Thermo-Mechanical Modeling for Selective Laser Melting

Von der Fakultät für Maschinenbau
der Gottfried Wilhelm Leibniz Universität Hannover

zur Erlangung des akademischen Grades
Doktor-Ingenieur

genehmigte Dissertation
von

M.Sc. Henning Wessels

geboren am 13.05.1990 in Hildesheim

2019

Herausgeber:
Prof. Dr.-Ing. habil. Peter Wriggers

Verwaltung:
Institut für Kontinuumsmechanik
Gottfried Wilhelm Leibniz Universität Hannover
Appelstraße 11
30167 Hannover

Tel: +49 511 762 3220
Fax: +49 511 762 5496
Web: www.ikm.uni-hannover.de

© M.Sc. Henning Wessels
Institut für Kontinuumsmechanik
Gottfried Wilhelm Leibniz Universität Hannover
Appelstraße 11
30167 Hannover

Alle Rechte, insbesondere das der Übersetzung in fremde Sprachen, vorbehalten. Ohne Genehmigung des Autors ist es nicht gestattet, dieses Heft ganz oder teilweise auf photomechanischem, elektronischem oder sonstigem Wege zu vervielfältigen.

ISBN 978-3-941302-31-0

1. Referent: Prof. Dr.-Ing. habil. Peter Wriggers
2. Referent: Prof. Dr. Eugenio Oñate Ibañez de Navarra

Tag der Promotion: 10.07.2019

Zusammenfassung

Selektives Laserstrahlschmelzen (SLM, *engl.* Selective Laser Melting) ist ein additiver Fertigungsprozess, bei dem ein Metallpulverbett lokal mithilfe eines Lasers aufgeschmolzen wird. Schicht für Schicht können so komplexe, drei dimensionale Geometrien einschließlich Überhängen produziert werden. Zum heutigen Zeitpunkt basiert die Material- und Prozessentwicklung für SLM hauptsächlich auf experimentellen Studien, die sowohl zeit- als auch kostenintensiv sind. Simulationsmethoden bieten das Potential, ein besseres Verständnis der Interaktion von Prozess, Struktur und Eigenschaften zu gewinnnen. Damit kann Simulation helfen, optimale Prozessparameter für individualisierte Komponenten und die Verarbeitung innnovativer Pulvermaterialien zu bestimmen.

In dieser Arbeit wird ein striktes thermo-mechanisches Modell für den Phasenwandel unter Berücksichtigung finiter Deformationen entwickelt. Neben dem Phasenwandel ist das Verschmelzen von Pulverpartikeln eine weitere Besonderheit des SLM Prozesses. Bezüglich der numerischen Lösung eignen sich hierfür insbesondere netzfreie Methoden, da bei diesen die Darstellung des Verschmelzens intrinsisch in der Formulierung enthalten ist. Die komplexen, zeitlich veränderlichen Grenzflächen zwischen flüssiger Schmelze und festem Metall können ohne zusätzlichen numerischen Aufwand dargestellt werden. In dieser Arbeit wurde das Verfahren der kürzlich entwickelten Optimal Transportation Meshfree Methode (OTM) gewählt. Die OTM wurde als vielseitiges Werkzeug für fluid- und strukturmechanische Fragestellungen vorgestellt.

Ein weiterer Fokus der Arbeit liegt in der Modellierung der Interaktion von Laser und Bauteil. Die Laserstrahlung kann in diskrete, bewegliche Energieportionen, sogenannte Strahlen (*engl.* rays) unterteilt werden, deren Bewegung in Raum und Zeit verfolgt wird. Um die Reflektion und Absorption von Strahlen zu berechnen, wird für gewöhnlich die Oberfläche des diskretisierten, bestrahlten Bauteils trianguliert. Im Rahmen von netzfreien Berechnungsmethoden ist die Triangulation mit erhöhtem Rechenaufwand verbunden. Um dies zu vermeiden, wird ein allgemeiner und effizienter Algorithmus vorgestellt, der sich leicht auch mit anderen netzfreien Methoden kombinieren lässt.

Sowohl die Dynamik des Schmelzbads als auch die Entstehung von Eigenspannungen werden mit dem entwickelten Berechnungsmodell untersucht. Der Einfluss von Laserbestrahlung und Auskühlbedingungen wird ebenfalls beleuchtet. Obwohl die Ergebnisse zum Teil vielversprechend sind, werden auch Einschränkungen der OTM deutlich. Die Genauigkeit der Methode wird daher abschließend kritisch diskutiert.

Schlagworte: Additive Fertigung, Selektives Laserstrahlschmelzen, Phasenwandel-Modellierung, Ray Tracing, Implizite Netzfreie Methode, Optimal Transportation Meshfree Methode

Abstract

Selective Laser Melting (SLM) is an Additive Manufacturing (AM) process where a powder bed is locally melted with a laser. Layer by layer, complex three dimensional geometries including overhangs can be produced. Up to date, the material and process development of SLM mainly relies on experimental studies that are time intensive and costly. Simulation tools offer the potential to gain a deeper understanding of the process - structure - property interaction. This can help to find optimal process parameters for individualized components and the processing of innovative powder materials.

In this work, a rigorous thermo-mechanical framework for the finite deformation phase change problem is formulated. Beside the phase change, an additional peculiarity of the SLM process is the fusion of powder particles. Regarding the numerical solution, meshfree methods seem to be especially suited because the treatment of particle fusion is intrinsic to the formulation. The complex moving boundaries between liquid melt and solid metal can be resolved without additional numerical effort. The recently introduced Optimal Transportation Meshfree Method (OTM) has been chosen since it was promoted as a versatile tool for both fluid and solid mechanics.

Special focus lays on the modeling of laser-matter interaction. The laser beam can be divided into moving discrete energy portions (rays) that are traced in space and time. In order to compute the reflection and absorption, usually a triangulation of the free surface is conducted. Within meshfree methods, this is a very expensive operation. To avoid the need for surface triangulation, a computationally efficient algorithm is presented which can easily be combined with meshfree methods.

Both melt pool dynamics and residual stress formation are studied with the developed numerical framework. The influence of laser heating and cooling conditions on melting and consolidation is investigated. Although the numerical results are promising, it was found that the OTM exhibits some limitations. Therefore, the accuracy of the method is critically discussed.

Keywords: Additive Manufacturing, Selective Laser Melting, Phase Change Modeling, Ray Tracing, Implicit Meshfree Scheme, Optimal Transportation Meshfree Method

Acknowledgements

Herewith I want to take the opportunity to thank Professor Peter Wriggers for the freedom he gave me in elaborating this thesis. I am especially grateful for the support for a six month lasting research stay at the University of California, Berkeley in the group of Professor Tarek I. Zohdi. The discussions with Professor Zohdi and his coworkers always gave me a new perspective when I felt stuck in a problem. The Fulbright Commission is acknowledged for the organizational and financial support.

I thank Christian Weißenfels for his guidance. During my time at the Institute of Continuum Mechanics, he always had an open ear for me and provided constructive feedback. I deeply appreciate the uncountable fruitful discussions we had.

Special thanks also goes to Tobias Bode. His interest in the topic and hard work on a ray tracing algorithm as part of his Master's thesis advanced the project a lot. I am also very thankful for the inspiring collaboration with Jan-Philipp Fürstenau. My office mate Mohsin Chaudry not only made our office a livable place, his critical mind also helped me in elaborating this thesis.

A special shoutout goes to Volker Meine, technical coworker at the IKM, to whom I owe nearly every drawing in this work. I greatly appreciate the help of Jens Bsdok, system administrator, in preparing my private laptop for my stay in the US and in numerous other IT issues.

I want to thank my family for their unconditional faith and support. Inga and Leni - I love you!

Hannover, August 2019 Henning Wessels

Contents

Index ix

1 Introduction **1**
- 1.1 Additive Manufacturing 2
- 1.2 Meshfree Methods 3

2 Selective Laser Melting **7**
- 2.1 Physical Phenomena 9
- 2.2 Process Simulation for Selective Laser Melting 14

3 Concept of Continuum Mechanics **19**
- 3.1 Kinematics 19
- 3.2 Balance laws 21
- 3.3 Guidelines for Constitutive Modeling 25

4 A Thermo-Mechanical Model of SLM **27**
- 4.1 Finite Deformation Phase Change Approach 27
- 4.2 Constitutive Model for the Phase Change Problem 29
  - 4.2.1 Elasto-Plasticity 34
  - 4.2.2 Elasto-Visco-Plasticity 35
  - 4.2.3 Dissipation 37
- 4.3 Boundary Conditions 37
  - 4.3.1 Surface Tension and Marangoni Convection 39
  - 4.3.2 Recoil Pressure 39

5 Heat Source Modeling **41**
- 5.1 Ray Tracing 42
- 5.2 Volumetric Heat Sources 44

6 Optimal Transportation Meshfree Algorithm **47**
- 6.1 Explicit Solution of the Energy Equation with OTM 48
- 6.2 Implicit Thermo-Mechanical OTM 50
  - 6.2.1 Update of Kinematic Quantities 54
  - 6.2.2 Local Newton-Raphson Algorithm 54
  - 6.2.3 Stabilization of the Momentum Equation 57
- 6.3 Search algorithm 57

6.4 Local Maximum Entropy Shape Functions 58
6.5 Automatic Code Generation 59
6.6 Contact Formulation 60

7 Coupling of Ray Tracing and OTM 63
7.1 Influence of Spatial OTM Discretization 64
7.2 Laser Discretization 65
7.3 Reflection 66
7.4 Comparison of Heat Source Modeling 69
7.5 Investigation of Laser Pulsing 71

8 Metal Particle Fusion Analysis 73
8.1 Material Data 73
8.2 Influence of Surface Tension 77
8.3 Influence of Cooling Conditions 79
8.4 Impact of Heat Source Modeling 83
8.5 Consolidation Analysis 86
8.6 Melting of Packed Powder 88

9 Limitations of the OTM 91
9.1 Marangoni Convection 91
9.2 Curvature 93
9.3 Accuracy 96

10 Conclusion and Outlook 101

A Free energy potential 105

B Linearization 107

C Heat Source Modeling 109
C.1 Gusarov Model 109
C.2 Ray Tracing 109

D Particle Fusion 111
D.1 Influence of Spatial and Temporal Discretization 111
D.2 Stability of LME Shape Functions 113

Bibliography 114

CURRICULUM VITAE 127

Index

Symbols and Operators

$\dot{\bullet}$	Material time derivative
div	Divergence current configuration
grad	Gradient current configuration
$\delta(\bullet)$	Symbol of a virtual quantity
$\Delta(\bullet)$	Symbol of a linearized quantity
$\boldsymbol{\eta}$	Virtual displacements
ξ^1, ξ^2, ξ^3	Curvilinear coordinates

Continuum quantities

$\mathbf{a}$	Acceleration vector
$\mathbf{b}$	Left Cauchy Green tensor
$\bar{\mathbf{b}}$	Isochoric left Cauchy Green tensor
$\hat{\mathbf{b}}$	Acceleration caused by volumetric forces
$\tilde{c}$	Color function
$\mathbf{c}$	Gradient of color function
$\mathbf{C}$	Left Cauchy Green tensor
$\mathrm{d}a$	Current surface increment
$\mathrm{d}v$	Current volume increment
$\mathrm{d}A$	Initial surface increment
$\mathrm{d}V$	Initial volume increment
D_{int}	Internal dissipation
$\mathbf{d}$	Stretch tensor
$_e$	Elastic component
$\mathbf{e}$	Euler Almansi strain tensor
$\mathbf{e}_i$	Cartesian base vector
$\mathbf{E}$	Green Lagrange strain tensor
f	Yield criterion
$\mathbf{F}$	Deformation gradient
$\mathbf{g}_i$, $\mathbf{g}^i$	Co- and contravariant base vector current configuration
$\mathbf{G}_i$, $\mathbf{G}^i$	Co- and contravariant base vector initial configuration
J	Determinant of the deformation gradient
L_m, L_v	Latent heat of melting, vaporization
$\mathbf{l}$	Velocity gradient current configuration
$\mathbf{n}$	Surface normal
$_p$	Plastic component
p	Pressure
p^{rec}	Recoil pressure
$\mathbf{p}$	Process vector
$\hat{q}$	Hardening stress
$\bar{q}$	Norm of surface heat flux

$\mathbf{q}$	Heat flux current configuration
r^s	Inner heat production current configuration
$\mathbf{r}$	Distance vector
s	Entropy
t	Time
$\mathbf{t}$	Surface load current configuration
u	Internal energy
$\mathbf{u}$	Displacement vector
$\mathbf{v}$	Velocity vector
$\mathbf{x}$	Position vector current configuration
$\mathbf{X}$	Position vector initial configuration
α	Accumulated plastic strain
$\dot{\gamma}$	Plastic multiplier
Γ_N	Neumann boundary
$\Delta\mathbf{F}$	Incremental deformation gradient
$_\theta$	Thermal component
θ	Temperature in Kelvin
θ_0	Reference temperature in Kelvin
κ	Curvature
ρ_0	Initial density
ρ	Density current configuration
σ_{Y0}	Initial yield limit
$\boldsymbol{\sigma}$	Cauchy stress tensor
$\boldsymbol{\tau}$	Kirchhoff stress tensor
ϕ	Phase indicator
$\boldsymbol{\chi}$	Motion
ψ	Helmholtz free energy

Discrete quantities

a_p	Current material point surface
$\mathbf{C}$	Heat capacitance matrix
$\mathrm{d}\mathbf{x}_I$	Distance vector
$\mathbf{e}_I$	Discrepancy
$\mathbf{E}$	Penalty stabilization
G	Thermo-mechanical residual
h_p	Characteristic length of material point
$\mathbf{h}_p$	Vector of internal variables
$_I$	Nodal quantity
$\mathbf{K}$	Thermal conductivity matrix
$\mathbf{K}^p$	Curvature tensor
$\mathbf{K}_{p\,ace}$	*AceGen* contribution to material point tangent
$\mathbf{M}$	Mass matrix
$_n$	Previous time step
$_{n+1}$	Current time step

n_{mp}	Number of material points
N	Shape function
N_p^{sup}	Size of support domain
N_I^{inf}	Size of influence domain
${}_p$	Material point quantity
$\mathbf{p}_p$	Vector of nodal increments
$\mathbf{P}$	Load vector
$\mathbf{Q}$	Heat input vector
$\mathbf{Q}_p$	Local residual vector
$\mathbf{R}_{p\,ace}$	*AceGen* contribution to material point residual
$\mathbf{R}_{\mathbf{u}}$	Vector of internal forces
$\mathbf{R}_\theta$	Thermal conductivity vector
$\mathbf{R}_{\mathbf{u}}^{con}$	Contact force vector
$\mathbf{R}_\theta^{con}$	Contact heat flux vector
${}_r$	Ray quantity
r_p	Radius of support domain
S_p	Support domain of material point
v_p	Current material point volume
$\bar{v}_p$	Averaged material point volume
$\boldsymbol{\lambda}_p$	LME Lagrange multiplier

Material parameters

c	Heat capacity
c_{L_θ}	Latent heat contribution to heat capacity
E	Young's modulus
H_α	Plastic hardening modulus
H_θ	Thermal softening modulus
k	Thermal conductivity
T_m, T_v	Melting, vaporization temperature
T_{sol}, T_{liq}	Solidus, liquidus temperature
T_{bub}, T_{dew}	Bubble, dew temperature
$\alpha, \alpha_{powder}, \alpha_{bulk}$	Heat transfer coefficient (of powder, bulk metal)
α_θ	Thermal expansion coefficient
γ	Surface tension coefficient
η	Dynamic viscosity
μ	Second Lamé constant
ν	Poisson ratio

Laser and heat source parameters

A_{laser}	Laser spot size
E_r	Energy associated to a ray
f_{rep}	Repetition rate
I, I_{rad}, I_{dep}	Intensity function, (radial, depth component)

k_{red}	Ray speed reduction factor
L	Layer thickness
n_{rpl}	Number of rays per level
$\hat{n}$	Ratio of refractive indices
N_I^{nbr}, N_p^{nbr}	Number of neighbors of a node (material point)
$\mathbf{n}_r$	Normalized direction vector of ray trajectory
$\mathbf{n}_{refl}$	Normal vector to reflecting surface
P	Laser power
r	Distance from focal midpoint
r_{abs}	Absorption radius
r_{det}	Detection radius
R	Laser beam radius
R_r	Reflectivity of ray
v_{laser}	Laser speed, scan rate
w_p^{abs}	Weighting function for ray absorption
w_p^{norm}	Weighting function for surface normal
$\mathbf{x}_c$	Anchor point of ray reflection
β	Optical extinction coefficient
Δt_r	Time step of ray creation
Δt_{rep}	Repetition interval
Δt_{puls}	Pulsing period
θ_r^{in}	Angle between incoming ray and surface
λ	Optical thickness
$\hat{\mu}$	Ratio of magnetic permeability
ρ_h	Hemispherical reflectivity

Numerical parameters

c^{enla}	Enlarge factor of search radius extension factor
α^{ext}	Search radius extension factor
β_p	LME locality parameter
γ^{LME}	LME constant
$\triangle t$	Time step increment
ε_c	Contact parameter
ε_s	Stability parameter

Chapter 1

Introduction

Thanks to its unique flexibility, Additive Manufacturing (AM) has received great attention in recent years[1]. From 2010 to 2016, the market for AM products and services has grown by nearly 5.7 times and exceeded an estimated volume of \$6 billion in 2016 (WOHLERS, 2017). Many different processes for all kinds of materials have emerged. Compared to other manufacturing technologies, the sequential adding of material increases the freedom in design and material texture significantly. Unfortunately, the flexibility of AM is not free of cost. The more parts of a kind need to be produced, the less competitive AM processes are compared to traditional manufacturing techniques like casting, die casting, cutting or milling. Today, AM is mostly suited either for individualized applications or if a functionality is achieved which compensates for the higher production costs. An example for the first scenario are patient specific implants (EOS GMBH, 2015). Gas turbines are a commonly cited application for the second scenario, since the increased efficiency of long-living gas turbines may outnumber the prime cost (NAVROTSKY, 2014).

AM metal production is rapidly gaining industrial importance. In 2016, an estimated 957 machines were sold for an average price of \$566,750. Compared to the sales in 2015, this corresponds to a growth of 18.4% (WOHLERS, 2017). An AM technology commonly employed for the fabrication of metal parts is a process called Selective Laser Melting (SLM). It is a powder bed fusion process, where a laser melts the desired portions of a metallic powder bed layer by layer. Melting and consolidation occur within milliseconds. The fast thermal cycles and the strong melt pool dynamics which are typical for the process are difficult to investigate experimentally. More than 130 parameters affect the quality of SLM fabricated parts (YADROITSEV, 2008). However, the interplay of all these phenomena is not yet fully understood which contributes to the high cost of SLM. Often more than one trial is necessary until desired geometries can be produced within acceptable tolerances. Computational methods can help to give insight into the physical mechanisms and to find the optimal setup. Therefore, numerical simulation is a promising technique to increase the confidence in AM and to reduce the time-to-market. It could further help to increase the design space towards faster build rates and accelerate the process development for new materials or alloys. For well-established mesh-based numerical methods such as Finite Element, Finite-Volume and Finite-Difference Methods, SLM is a challenging process. The fusion of metal powder particles causes an evolution of the free surface and large deformations. These problems are difficult to represent with the aforementioned traditional methods because the fulfillment of topological requirements on the mesh is not straightforward. Meshfree methods promise to overcome these limitations. A novel method of this type is the Optimal Transportation Meshfree Method (OTM). In LI ET AL. (2010), the OTM has been promoted as a flexible method applicable to both fluid and solid mechanics. The goal of this thesis is to assess its applicability for SLM powder scale simulations.

---

[1] Excerpts from this chapter have been published previously in FÜRSTENAU ET AL. (2019b).

In the remainder of this chapter, an overview of AM technology (section 1.1) and state of the art meshfree methods (section 1.2) is given. The further outline of this work is as follows: A detailed discussion of the SLM process, the related physical phenomena and previous modeling approaches can be found in chapter 2. In chapter 3, the concept of continuum mechanical modeling is introduced. Based on these principles, a thermo-mechanical model accounting for the physics relevant to SLM is developed in chapter 4. The modeling of the laser-matter interaction is discussed in chapter 5. The discretization of the developed set of equations with the stabilized Optimal Transporation Meshfree Method (OTM) is topic of chapter 6. In chapter 7, a coupling algorithm for meshfree schemes and ray tracing is introduced. Numerical results taking into account different process conditions are presented in chapter 8. Chapter 9 gives an insight into currently existing limitations of the OTM method. The thesis concludes with a summary and an outlook in chapter 10.

1.1 Additive Manufacturing

Manufactured objects owe their functionality to a combination of geometry and properties. Following DIN EN ISO 52900 (2017), these features are obtained with manufacturing technologies that can be classified into three groups:

- Subtractive: *"The desired shape is acquired by selective removal of material, examples: milling, turning, drilling, EDM, etc."*
- Formative: *"The desired shape is acquired by application of pressure to a body of raw material, examples: bending, casting, injection moulding, the compaction of green bodies in conventional powder metallurgy or ceramic processing, etc."*
- Additive: *"The desired shape is acquired by successive addition of material."*

Often, a combination of the aforementioned technologies is necessary to produce parts with desired specifications. For example, surface finishing with subtractive operations is a common post processing step for AM produced metal parts. In this section, common traits of AM processes are discussed.

The layer-wise processing of material has brought AM the name 3D printing which is commonly used in the media. The different layers are joined together in the height coordinate direction. A typical feature is that the tool path is derived from a CAD drawing. The latter can either be the result of an innovative design process involving topology optimization software or stem from a 3D scan. Usually, the CAD drawing is stored in stl format (*surface tesselation language*, abbr. stl). A preprocessing software reads the stl file, slices the 3D part into layers and generates the machine code. Due to the slicing operation, curvatures along the height coordinate can only be approximated up to the minimal processable layer thickness.

Since continuous surfaces cannot be generated in all three spatial dimensions, AM processes are sometimes referred to as 2.5D processes. If continuous curvatures need to be generated, post processing with subtractive operations such as surface polishing are necessary.
In the past decades, AM processes for a variety of different materials have been developed. Today, ceramics, plastics and metals can be processed. Depending on the application of additively manufactured parts, different terms for AM processes have emerged. The most commonly used are Rapid Prototyping, Rapid Tooling and Rapid Manufacturing. Another possible classification of AM processes is suggested in GEBHARDT & HÖTTER (2016) and follows the standard for primary shaping DIN 8580 (2003). Therein, processes are classified according to the aggregate state of the processed material as it enters the machine. This classification is illustrated in figure 1.1.
The most common AM processes for metals start with solid material as filament or powder. Thereby, it is distinguished between metal deposition and powder bed fusion processes. In metal deposition processes, a laser melts the surface of the processed part while powder is fed through a nozzle. Alternatively, the metal may also be fed in form of molten filament. Metal deposition processes can not only be used to build new, but also to repair existing components. For the production of new parts, powder bed fusion is a sound alternative to laser metal deposition. Additional support structures which reduce the formation of residual stress can be easily generated. In powder bed processes, cohesion of powder particles is established either in a two step process, where a plastic binder is introduced and subsequently removed in a sinter process; alternatively, the metal is directly molten with a moving heat source, which may be a laser or an electron beam. If the heat source is a laser, the process is often referred to as Selective Laser Melting (SLM), which is the process considered in the present work. A detailed description follows in chapter 2. For an in-depth discussion of a variety of AM processes, see e.g. GEBHARDT & HÖTTER (2016) or GIBSON ET AL. (2010).

1.2 Meshfree Methods

Mesh-based methods such as the Finite Element (FEM), Finite Volume (FVM) and Finite-Difference Method (FDM) are well established in industrial research and development. In solid mechanics, FEM is especially suited for problems formulated in Lagrangian[2] description involving small to medium deformations. The method is described in a variety of standard textbooks, see e.g. DHATT & TOUZOT (1985), HUGHES (2000) or WRIGGERS (2008). In Computational Fluid Dynamics (CFD), the study of flows in Eulerian[2] formulation within enclosed domains, e.g. gas turbines, is typically performed with FVM and FDM. An introduction to CFD can be found in FERZIGER & PERIĆ (2002). When mesh-based methods are applied to other problems involving large deformations and free surface flows, topological requirements on the mesh are difficult to fulfill: The evolution of free surfaces is not intrinsic to Eulerian formulations, while in Lagrangian methods, mesh distortion may yield to inaccuracies and failure of computations. A variety of attempts has been made to compensate for these negative effects. A surface recognition technique commonly employed in CFD is the Volume of Fluid (VoF) approach. In an attempt to minimize the mesh distortion by

---

[2] The difference between the Eulerian and the Lagrangian formulation is briefly explained in chapter 3.

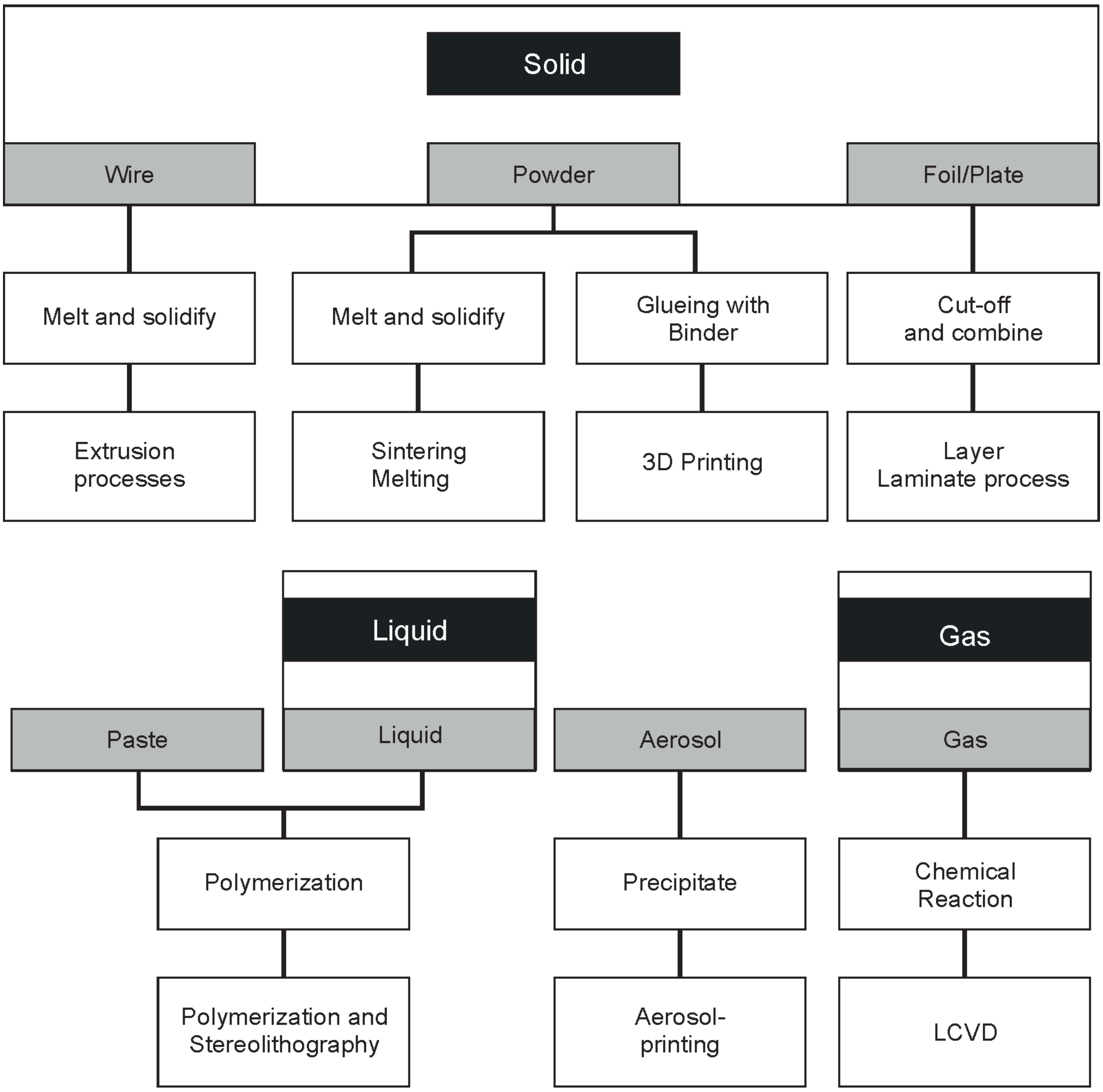
Solid
Wire
Powder
Foil/Plate
Melt and solidify
Melt and solidify
Glueing with Binder
Cut-off and combine
Extrusion processes
Sintering Melting
3D Printing
Layer Laminate process
Liquid
Gas
Paste
Liquid
Aerosol
Gas
Polymerization
Precipitate
Chemical Reaction
Polymerization and Stereolithography
Aerosol-printing
LCVD

Figure 1.1. Classification of AM processes according to the aggregate state of the processed material as it enters the machine. The classification follows the standard of primary shaping DIN 8580 (2003). This figure is adapted from GEBHARDT & HÖTTER (2016).

moving the mesh independently of the material motion, Hirt et al. (1974) developed the Arbitrary-Lagrangian-Eulerian (ALE) method. Beside these efforts to improve mesh-based methods, a new family of numerical methods has emerged which aim to remove entirely the mesh dependency. The members of this family are referred to as meshfree methods. The key feature is that extensive quantities are not related to a mesh, but stored at discrete points which are often called particles (Chen, 2019).

Many different meshfree methods have been developed. Depending on the employed discretization technique they are either more suitable to represent granular (particulate) or continuous material. Numerical solution schemes for particulate media are Molecular Dynamics (MD) and the Discrete Element Method (DEM). In both methods the particle positions are updated from the interaction forces. In MD, the discretization is performed on the molecular scale. An introduction to the method can be found in Griebel et al. (2007). DEM is numerically similar to MD but used to discretize particles comprised of more than one molecule. In the context of SLM, DEM is the method of choice to model the powder deposition prior to melting, see e.g. Ganeriwala & Zohdi (2016). For the same purpose it is implemented into the commercial software *Flow3D®*.

The probably most famous representative of the meshfree family is Smoothed Particle Hydrodynamics (SPH). It has been developed independently by Lucy (1977) and Gingold & Monaghan (1977). The method was originally intended for astrophysical computations. The governing equations are derived in the strong form and discretized by the means of kernel functions while making use of nodal integration. Therefore, SPH is often considered as a collocation method. Thanks to its conservation properties, today SPH is widely used in academia to tackle fluid flow problems involving free surfaces. However, SPH suffers from well known problems such as tensile instabilities and a rank deficiency, see e.g. Belytschko et al. (2000). These problems become especially pronounced in solid mechanics. Dyka & Ingel (1994) have studied the effect of additional integration points, so called stress points to remove the tensile instability. The limited benefit and the additional computational effort related to the insertion of stress points have prevented a broader application of this stabilization approach in the SPH community. Belytschko et al. (1998) have found that SPH derivatives do not meet completeness conditions. While various correction techniques have been developed aiming to recover completeness, these are also not free of flaws. Price (2012) states that within SPH, exact derivatives compromise the conservation properties. He also provides a detailed overview and an introduction to SPH.

Another meshfree method that has been recently introduced by Silling (2000) is Peridynamics. Unlike classical continuum mechanics, which is based on partial differential equations, Peridynamics is formulated in terms of integro-differential equations. This makes the method especially suitable to model fracture. The original bond based formulation is restricted to linear elasticity and Poisson ratios of 0.25. Using so-called state based Peridynamics, classical material models based on the deformation gradient can be incorporated. However, it has been found that the latter approach exhibits strong similarities with other meshfree methods. For a nodal integration scheme, Bessa et al. (2014) have shown equivalence of state based Peridynamics with a special case of the Reproducing Kernel Particle Method (RKPM) while Ganzenmüller et al. (2015) have demonstrated that it is identical to a special type of SPH formulation. An in-depth discussion of Peridynamics can be found in BOBARU (2017).

The Diffusive Element Method introduced by NAYROLES ET AL. (1992) makes use of nodal integration and Moving Least Square (MLS) interpolation. In order to resolve instabilities inherent to the method, BELYTSCHKO ET AL. (1994) have introduced the Element Free Galerkin method (EFG) by introducing another set of points arranged on a background mesh. Conceptually, the method is similar to the Material Point Method (MPM). In MPM, integration points travel through a fixed grid of nodes while in EFG, nodes travel through a background grid of integration points. Details on both methods can be found in LI & LIU (2007).

The Optimal Transportation Method (OTM) has initially been introduced by LI ET AL. (2010). While originally derived from the theorem of optimal transportation (VILLANI, 2003), the OTM can also be regarded as a Galerkin method: WEISSENFELS & WRIGGERS (2018) have derived it from the principle of virtual work. In OTM, the extensive quantities are defined on additional integration points, so called material points. These are not arranged on a fixed grid, but also updated during the computation. In the original publication, the OTM has been promoted as a flexible meshfree method which is applicable to both fluids and solids. This flexibility makes the OTM a promising tool for phase change simulations and hence for SLM. The method has been employed in the present work and is discussed in detail in section 6.

It is understood that this review of meshfree methods is by no means complete. For an in-depth discussion of the topic, the reader is referred to LI & LIU (2007).

Chapter 2

Selective Laser Melting

Selective Laser Melting (SLM) is an Additive Manufacturing (AM) technology which belongs to the class of Powder Bed Fusion (PBF) processes[1]. In DIN EN ISO 52900 (2017), PBF is defined as an "*additive manufacturing process in which thermal energy selectively fuses regions of a powder bed*". The heat source may either be a laser or an electron beam. When the heat source is an electron beam, the process is referred to as Electron Beam Melting (EBM). Compared to laser heat sources, higher scan rates can be used and the electrons may penetrate deeper into the powder bed than a laser. However, EBM processes must be held in vacuum, which is expensive. When using a laser heat source, this not necessary. Laser powder bed fusion is often referred to as Selective Laser Melting (SLM). It must be mentioned that the abbreviation SLM is a registered trademark of the companies SLM® Solutions GmbH and Realizer GmbH, whereby the latter is today operating under the umbrella of DMG Mori. Per consequence, strictly speaking SLM is not available as a generic term. Nevertheless, in the literature, including previous publications of the author and the present work, Selective Laser Melting (SLM) is often used as such. Although SLM is a relatively new technology, many machine manufacturers have emerged. An overview of manufacturers and their concurrent process terms is listed below:

- Electro Optical Systems GmbH (EOS), Krailingen, Munich, Germany
  Direct Metal Laser Sintering (DMLS)
- 3D Systems Inc., Rock Hill, SC, USA
  Direct Metal Printing
- DMG Mori, Nagoya, Japan
  Selective Laser Melting (SLM®)
- SLM® Solutions GmbH, Lübeck, Germany
  Selective Laser Melting (SLM®)
- Renishaw Inc., Gloucestershire, UK
  Metal Powder Bed Fusion
- Concept Laser GmbH, Lichtenfels, Germany (partially owned by GE Additive)
  LaserCUSING®

---

[1] Excerpts from this chapter have been published previously in FÜRSTENAU ET AL. (2019b).

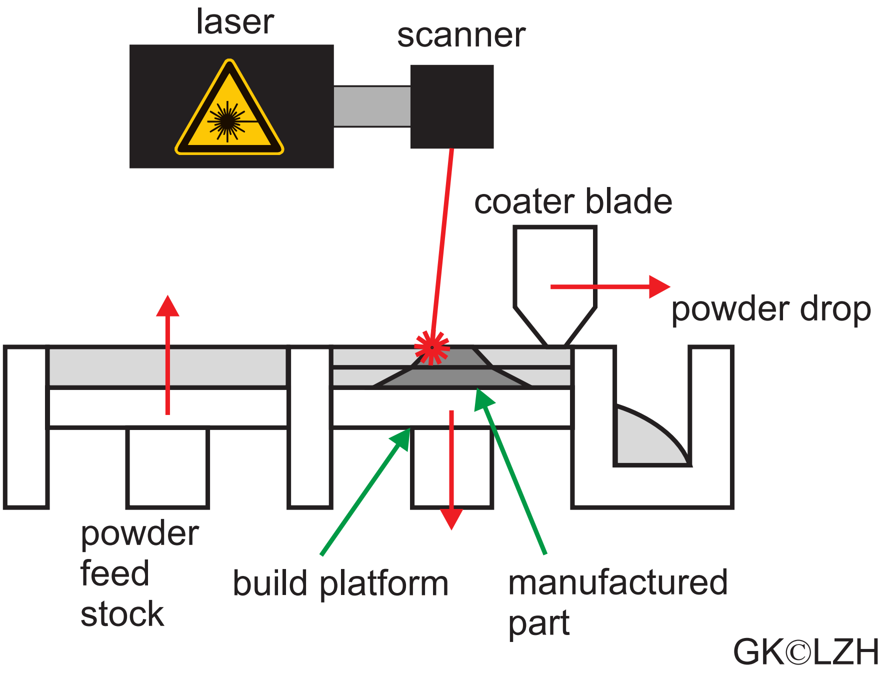

Figure 2.1. Process schematic of Selective Laser Melting adapted from GIESEKE ET AL. (2016).

- TRUMPF Laser GmbH & Co. KG, Ditzingen, Germany
  Direct Laser Forming

A summary and a detailed comparison of the processes from the above listed competitors can be found in GEBHARDT & HÖTTER (2016). In the following, a general description of the SLM process is provided and common traits are discussed.

The first processing step in SLM is to spread a thin layer of metal powder from a feed stock onto a build plate of bulk metal. Next, the powder bed is partially irradiated with a laser according to a predefined tool-path derived from a CAD model. Once a layer has been completed, the coater blade adds a new layer for laser processing. This procedure is schematically sketched in figure 2.1. The process is held under an inert gas atmosphere of argon or nitrogen to prevent oxidation. After the build has completed, unprocessed powder is removed and recycled. Typical materials for SLM processing are titanium alloys (e.g. TiAl6V4) and stainless steel (e.g. SS316L). Optional post-processing steps include surface polishing and heat treatment such as annealing or Hot Isostatic Pressing (HIP). Experimental investigations on the effect of heat treatment on residual stresses and the mechanical properties of as-built components can be found e.g. in SERCOMBE ET AL. (2008) and SONG ET AL. (2014).

The achievable layer resolution is in the range of 30-100 μm and highly affected by the powder diameters. Often, the machine manufacturers sell proprietary powder for operation with their machines. For these powders, the manufacturers guarantee mechanical properties of finished parts within a specified window of process parameters. The operation with commercial powders is generally possible, but admissible parameter sets must be identified beforehand. Powder characterization is discussed in detail in YADROITSEV (2008).

Beside the powder characteristics, the geometrical resolution of as-built components is dictated by the melt pool geometry. To achieve consistent accuracy, it is important to keep the melt pool size constant during the process. The melt pool geometry in turn is governed by the cooling conditions (which may vary during the process) and the volumetric energy density VED. The latter is obtained from the laser power P_{laser}, the scan rate v_{laser}, the layer thickness L and the hatch spacing h. A hatch denotes a single laser track, therefore h is closely related to the beam diameter R. GU ET AL. (2013) give the following definition of volumetric energy density:

$$VED = \frac{P_{laser}}{v_{laser}\, h\, L} \tag{2.1}$$

A similar definition can be found in NEUGEBAUER ET AL. (2014). In practice, high scan rates are desirable because they come along with high production rates. However, in order to maintain the volumetric energy density, higher scan rates necessitate increased laser powers. These boost the thermal gradients which in turn cause residual stress formation and distortion. Hence, a key task in process planning is to find a Pareto-Optimum for the trade-off between laser power and scan rate (KHAIRALLAH & ANDERSON, 2014).

An important quality measure of SLM manufactured parts is the density. According to GU ET AL. (2013), in optimized processes densities greater than 99.9% referred to pure metal can be realized. Responsible for the lower densities compared to pure metal are voids. Since voids can favor e.g. crack initiation, the density of a part is closely related to its mechanical properties. Hence, a thorough understanding of the mechanisms of void formation is important. In the literature, five different mechanisms of void formation are reported. The first is that surrounding gas present in the gaps between powder particles may be encapsulated by the violent melt flow (KHAIRALLAH & ANDERSON, 2014). Analogously, unmolten powder particles can be enclosed. This second type of void formation becomes prominent at higher scan rates, thus lower energy densities (KHAIRALLAH & ANDERSON, 2014). On the contrary, at high energy densities the likelihood for vaporization and therefore for the enclosure of vaporized metal is increased, which is a third mechanism reported in GANERIWALA & ZOHDI (2016). Micro-cracking caused by residual stresses can be regarded as a fourth mechanism of void generation. An additional source is insufficient wetting of consolidated material with melt, which is due to surface tension effects. In summary, void formation is related to highly-coupled physical effects. These are topic of the subsequent section 2.1. Existing simulation approaches describing the SLM process are summarized in section 2.2.

2.1 Physical Phenomena

Absorption of laser irradiation as well as heat emission to the surroundings and heat transfer into the workpiece are the first important physical effects to mention. The laser causes the powder to melt, thereby the powdered material fuses together and forms the melt pool. The latter is subject to large, temperature dependent surface tension effects. Keeping the size of the melt pool constant is fundamental to achieve a constant geometrical printing resolution. Escaping vaporized metal may impose a recoil pressure and indent the melt pool. These effects are illustrated in figure 2.2. Since the heat input is highly localized, the melt rapidly consolidates when the laser moves onwards. Consolidation comes along with residual stress formation and microstructure evolution. The microstructure is responsible for the

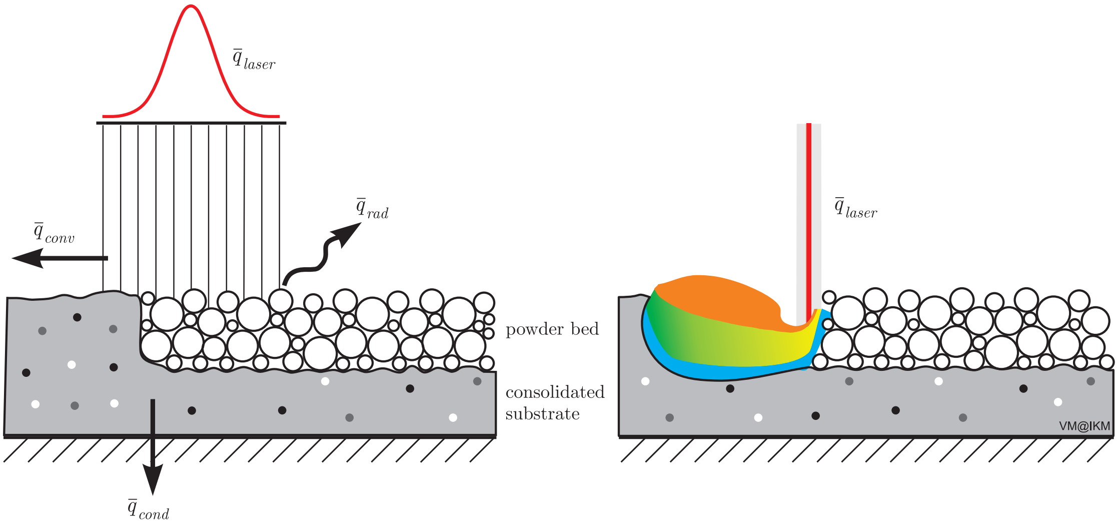

Figure 2.2. Left: The incident laser irradiation $\bar{q}_{laser}$ is emitted by thermal conduction $\bar{q}_{cond}$, convection $\bar{q}_{conv}$ and radiation $\bar{q}_{rad}$. Right: Escaping vapor indents the melt pool. Voids caused by the enclosure of vaporized metal, non-molten powder particles and surrounding gas are represented by gray, black and white dots, respectively.

mechanical properties of as-built components. In this section, the aforementioned physical phenomena which are crucial for the SLM process are thoroughly discussed. Detailed reviews on the topic can be also found in KING ET AL. (2015) and GU ET AL. (2013).

Laser Absorption, Heat Emission and Transfer

The fraction of laser power that is absorbed by the irradiated material varies with phase. Melt reflects incident irradiation better than powdered material. Laser radiation may deeply penetrate a powder bed due to multiple reflections. Modeling strategies for absorption and reflection will be discussed in chapter 5.

The fundamental mechanisms of heat transfer are radiation, convection and conduction. The thermal conductivity of powder is significantly lower compared to the denser liquid or consolidated material. ROMBOUTS ET AL. (2005) have experimentally shown that the thermal conductivity of powdered metal is mainly governed by the shape of its individual constituents. If vaporization occurs, the absorption of latent heat significantly cools the melt pool.

Phase Transition

The change of phase results in a change of internal structure. The energy necessary for this change in structure is expressed by a latent heat. It is absorbed or released depending on the direction of a phase change. During this process, the temperature remains constant. Multi-component alloys consist of different materials that in general change phase at different temperatures. Then, instead of a single melting temperature, a phase change interval is specified in terms of solidus and liquidus temperatures. The same applies to liquid - gas transitions, where bubble and dew temperatures are defined, see also section 4.2. As mentioned in the previous paragraph, the latent heat of vaporization significantly affects the temperature evolution. This will also be illustrated by means of numerical examples in section 8.4. Beside the latent heat effect, the phase change comes along with a drastic change in mechanical behavior. While the deviatoric stress in liquid and gaseous metal only depends on the rate of deformation, in solid metal it is a function of the current deformation state and the deformation history.

Surface Tension and Recoil Pressure

The difference between cohesive forces of liquid metal and surrounding argon gas is responsible for strong surface tension. Since the diameter of powder particles is in the range of micro-meters, the surface to volume ratio is quiet large compared to other metal processing technologies. In SLM, surface tension is therefore the main driving force for the fusion of powder particles. An order of magnitude analysis of the different forces can be found in section 8.2. However, surface tension is also responsible for the so-called balling effect which stems from the minimization principle of surface energy. In KHAIRALLAH & ANDERSON (2014), balling is explained by Plateau-Rayleigh instabilities which cause a break of the melt pool into spherical agglomerates. The wetting of consolidated material with its molten counterpart depends on the surface tension at the melt-substrate interface. Insufficient wetting may yield voids and lower the density ratio compared to bulk material. The wettability is defined in AGARWALA ET AL. (1995) by the contact angle θ between solid and liquid. Complete wetting is achieved for a zero contact angle. It is postulated that θ can be expressed in terms of the surface tensions τ_{sl}, τ_{sv} and τ_{lv} at the solid-liquid, solid-vapor and liquid-vapor interfaces, respectively:

$$\cos\theta = \frac{\tau_{sv} - \tau_{sl}}{\tau_{lv}} \tag{2.2}$$

A theoretical investigation of the contact angle evolution can be found in HU ET AL. (2018). The surface tension coefficients are temperature dependent. This causes a convective flow from regions of higher towards regions of lower temperature, also known as Marangoni effect. It is especially pronounced at the liquid-vapor interface, where the surface tension coefficient is highest. Another important aspect impacting the shape of the melt pool is evaporation. The high temperatures in the rear of the laser beam may yield an evaporation hot spot. Escaping vapor induces a recoil pressure which indents the melt pool. This effect is schematically illustrated in figure 2.2.

Residual Stress

Residual stresses originate during consolidation. The change of material stiffness and inhibited thermal expansion mainly cause their formation. WITHERS & BHADESHIA (2001a) and WITHERS & BHADESHIA (2001b) classify residual stresses according to the length scale l_0 on which they occur:

- Type I: Macroscopic or part scale, $l_{0,I} \approx$ scale of the structure. Type I stresses arise as a consequence of non-uniform plastic deformation or in the presence of sharp thermal gradients.

- Type II: Granular scale, $l_{0,II} \approx 3 - 10 \times$ grain size. Caused by heterogeneous material properties and different grain orientations. Low type II stresses are present in polycrystalline materials. Higher stresses occur when the microstructure consists of different phases or in the presence of phase transformations.
- Type III: Atomic scale, $l_{0,III} \approx$ grain size. Related to coherency at interfaces or dislocations.

Measurement techniques for the different types of stresses are discussed in WITHERS & BHADESHIA (2001a). Type I stresses can be assessed by measuring distortion when stresses arise or relax. Ultrasonic or X-ray measurements may also be used to detect stresses on the lower scales.

Residual stresses can severely affect the geometrical accuracy of printed parts and even cause failure. Their effect on fatigue lifetime can be expressed by Gerber or Goodman relations (WITHERS & BHADESHIA, 2001a). Generally, the higher the residual mean stress, the lower the admissible stress amplitude that can be applied to achieve the same lifetime. Another phenomenon related to residual stress is stress cracking, see GU ET AL. (2013). Microscopic cracking occurs during rapid solidification and is therefore referred to as hot, while macroscopic cracking is also known as cold cracking. In some applications, residual stresses are desired and used to positively influence the material properties, e.g. when toughening glass. In SLM, a reasonable level of residual stress increases the hardness of components (GU ET AL., 2013). GU ET AL. (2013) indicate three influence factors for the formation of residual stress in the SLM processes:

- the geometric height of the part
- the material properties, especially material stiffness and thermal expansion coefficient
- the laser scanning strategy and processing conditions

On the process side, it was found that especially a subdivision of the irradiated surface into smaller sectors significantly reduces residual stress formation. Another option is to create additional support structures, although non-melted powder already provides mechanical support. The importance of solid support structures can be explained with the difference in thermal conductivity of the different phases. The conductivity of melt and consolidated material is considerably better compared to a powder bed, where the voids filled with gas act isolating. Therefore, support structures can enhance the heat emission. This reduces thermal gradients and hence counteracts residual stress formation. For the same reason, it may be beneficial to fuse the part directly onto the build platform and to preheat the build chamber.

Microstructure

The fast thermal cycles in SLM result in an AM-specific microstructure. The time for grain growth is very short and therefore grain refinement is expected. Rapid solidification follows the direction of maximum heat flow, i.e. the maximum temperature gradient. According to GU ET AL. (2013), the combination of these two characteristics results in a variety

Phenomena	Description	Part scale	Powder scale
Heat input	phase dependent absorption and reflection properties	(x)	x
Heat emission	radiation, convection, conduction	(x)	x
Phase transition	– latent heat – change of mechanical behavior	x (x)	x x
Surface tension	difference in cohesive forces of different phases and materials	-	x
Keyholing	melt pool indentation by escaping vaporized metal particles	-	x
Residual stress	caused by sharp thermal gradients and cyclic heating and cooling	x	(x)

Table 2.1. Phenomena that can be described by the means of continuum mechanical equations on different scales. Effects that can and cannot be displayed on a given scale are marked with ”x” and ”-”, respectively. The representation of effects marked with ”(x)” is restricted to some limitations discussed in section 2.2.

of crystal orientations with a localized regularity. Beside the grain structure, the surface roughness is an important microstructural characteristic. The roughness is related to surface tension effects which were discussed in an earlier paragraph. Generally, the microstructure is influenced by the scanning strategy, since processing of the topmost layer influences the microstructure of layers beneath through repeated heating and cooling. Detailed information about microstructural features of laser based AM manufactured components can be found in GU ET AL. (2013) and KRAKHMALEV ET AL. (2018). The microstructure is closely related to the mechanical properties of as-built components which are briefly discussed in the next paragraph.

Mechanical Properties

The properties of SLM fabricated parts depend on the properties of the processed powder material and the aforementioned physical effects. Surface roughness, a microstructural feature, influences the friction and wear behavior which has been investigated by KUMAR & KRUTH (2008) for different powders. While the coefficient of friction measured was generally high, excellent wear performance could be obtained with some powders. According to GU ET AL. (2013), the hardness of AM fabricated parts is generally higher compared to casted components, because it is positively influenced by a reasonable level of residual stress. As discussed earlier in this chapter, an important characteristic of as-built components is the density which is affected by the mechanisms of void generation. While SLM produced parts are generally more brittle than bulk material, the yield and tensile strength are similar (KRUTH ET AL., 2005). The effect of scanning and part placement strategies on the strength of stainless steel components was experimentally investigated in GU & CHEN (2018).

2.2 Process Simulation for Selective Laser Melting

Numerous models have been developed to describe the SLM process. A classification into simplified, part scale, powder scale, thermo-metallurgical-mechanical and surrogate models is followed in this work. Simplified models are based on theoretical considerations, experience or experimental data. The entire thermal and sometimes also the mechanical history of the process is analyzed on the part scale. This allows the prediction of residual stress and distortion. Since computational resources are limited, severe simplifications are necessary within part scale simulations. The powder is not geometrically resolved as such. Its properties are averaged in continuum elements and the problem is usually solved with the well-known FEM. The change in material behavior is only captured by lowering the material stiffness and the resistance to plastic yielding, but the melt flow is not taken into account. Hence, melt pool effects such as surface tension and keyholing can not be represented. Also heat input and transfer are averaged because the exact surface through which heat is transmitted is unknown. Due to the volume averaging, local overheating and resulting vaporization cannot be resolved as accurately. On the powder scale, the transient melt pool dynamics of a single up to a few hatches are investigated. Basically, on the powder scale all effects mentioned in section 2.1 can be represented. However, the evolution of cracks and macroscopic residual stresses is rather interesting on the part scale, where their interference with actual laser scanning patterns and build heights can be investigated. CFD, ALE and SPH methods have been applied recently on the powder scale as will be discussed later on. The physical phenomena that can be displayed on the different scales are listed in table 2.1. It is important to emphasize that both scales are of interest for designers. Generally, part and powder scale simulations can be coupled to grain growth models to investigate the microstructure evolution. This will be discussed in the paragraph on thermo-metallurgical-mechanical models.

The SLM process has been conceptually divided into a part and a powder scale. A natural link between the different scales would be the melt pool geometry. However, the computational effort related to part scale simulations requires severe simplifications in which the heat input and therefore the melt pool are usually averaged over multiple layers (KING ET AL., 2015). This fact and the transient nature of the process hinder a combination of both scales in the sense of a traditional micro-macro formulation. Instead, surrogate models fed with information from both part and powder scale simulations as well as from experiments seem to be more promising (KAMATH, 2016). The idea of surrogate modeling is to build continuous curves to relate the input to specified output parameters of interest. In a learning phase, surrogate models are fed with data. After the learning phase is completed, they can be used to identify the processing window. Multiple algorithms are available for surrogate modeling, e.g. fitting of multi-variate functions, machine learning methods such as neural networks, regression trees, locally weighted learning and support vector machines (KAMATH, 2016).

In the remainder of this section, first simplified models are discussed. Next, part and powder scale simulations as well as thermo-metallurgical-mechanical approaches are presented. Finally, surrogate modeling strategies are described. A comprehensive review on SLM simulation can also be found in LIU ET AL. (2018).

Simplified models

In the past century, when computational power was much more limited, simple theoretical models found widespread use in the welding community. These may also be applied to estimate parameters for SLM applications (KAMATH, 2016). For example, ROSENTHAL (1946) has suggested a formula for the temperature evolution caused by a moving point heat source. While retaining most of the simplifying assumptions made in this model, EAGAR & TSAI (1983) have extended it to distributed heat sources for application in conduction mode laser welding. The enhanced model is used to relate the melt pool dimensions to the laser's power, speed, beam size and the material's absorptivity. A simplified theoretical model for the prediction of residual stresses in SLM finished parts has been postulated and experimentally validated by MERCELIS & KRUTH (2006).

Part scale

As discussed in the introduction of this section, severe simplifications are made in part scale simulations. This allows the use of concepts from Computational Welding Mechanics (CWM) (LINDGREN & LUNDBÄCK, 2018). An overview of CWM can be found in GOLDAK & AKHLAGHI (2005). While in CWM often only a single weld is investigated, fusing multiple layers of powder increases the computational effort tremendously. Therefore, in order to decrease the required computational time while maintaining accuracy, oftentimes adaptive meshing is employed. In regions with high temperature gradients a much finer mesh is necessary compared to regions of lower thermal gradients. Also, in coupled thermo-mechanical simulations, the monolithic solution of the system of equations is expensive. A staggered solution based on a split of the momentum and energy equation can reduce the computational cost. Such an iterative staggered algorithm is described e.g. in ZOHDI (2018). An adiabatic split approach combined with adaptive meshing is used in RIEDLBAUER ET AL. (2014).

A powerful thermo-mechanical part scale simulation tool is the *Diablo* code developed at the Lawrence Livermore National Laboratory (HODGE ET AL., 2014). A comparison of computational and experimental results can be found in HODGE ET AL. (2016). Recently, STRANTZA ET AL. (2018) have validated the model's ability to predict residual stress formation in TiAl6V4 with X-ray diffraction measurements. Although *Diablo* is intended for high performance computing, even in this framework simplifying assumptions are necessary to reduce the computational effort. Instead of simulating each layer individually, several layers are accumulated and simulated simultaneously (KING ET AL., 2015). Also commercial software has been used to study residual stress formation and distortion in SLM fabricated parts. NEUGEBAUER ET AL. (2014) have employed *MSC Marc/Mentat* for thermo-mechanical process simulations with CALPHAD (CALculation of PHase Diagram, abbr. CALPHAD) informed material parameters. A brief description of the CALPHAD approach is given in the thermo-metallurgical-mechanical paragraph.

As discussed in the previous section, the transient sharp thermal gradients strongly influence residual stress formation and microstructure. Thus, analyzing only the thermal history of the SLM process may give an estimate of processability. This approach is combined with adaptive meshing in RIEDLBAUER ET AL. (2017). A detailed review of various FEM studies can be found in SCHOINOCHORITIS ET AL. (2016).

Powder scale

Particle deposition can be modeled conveniently with the Discrete Element Method (DEM). GANERIWALA & ZOHDI (2016) not only simulated the particle packing, but also a single laser track with DEM. The model accounts for the statistical nature of the powder bed but lacks a physical representation of the melt flow. Displaying the free surface flow of molten metal is a key challenge for numerical methods on the powder scale. A three dimensional Lattice-Boltzmann Method (LBM) has been developed in AMMER ET AL. (2014) for the study of melt pool effects during Electron Beam Melting. The Arbitrary Lagrangian Eulerian (ALE) method has been applied to detailed, but computationally very expensive SLM simulations of melting and consolidation in the powder bed, see KHAIRALLAH & ANDERSON (2014) and KHAIRALLAH ET AL. (2016).
Recently, YAN ET AL. (2017) have studied the powder bed process using a Finite Volume (FV) formulation within the commercial software *Flow3D*®. In comparison to the ALE formulation of KHAIRALLAH & ANDERSON (2014), the FV approach was much more efficient in terms of computational time. It has also successfully been applied to model multiple layer fabrication (YAN ET AL., 2018c). A similar FV model has been implemented by QIU ET AL. (2015) into the open source CFD code *OpenFOAM*®. Keyhole formation has been investigated with the proposed method in PANWISAWAS ET AL. (2017a). However, a restriction of the FV method is that the solid phase is modeled as a highly viscous fluid. Note that such a solid phase model does not provide any reliable information about residual stress formation. Within mesh-based methods, the use of higher viscosities is necessary to account for the dynamic melt pool boundaries. Removing the solid from the simulation domain by introducing arbitrary curved zero-displacement Dirichlet boundaries would likely yield to volumetric locking. As RUSSELL ET AL. (2018) have shown, this is not the case for meshfree SPH computations: In two dimensional powder scale simulations, only the heat equation was solved in the solid phase. This methodology increases the efficiency of SPH computations compared to the aforementioned FV formulations tremendously. Another advantage of SPH is that in Lagrangian particle methods the tracking of the free surface is intrinsic. Special numerical treatments such as the Volume of Fluid (VoF) method are not necessary. A limitation of the SPH model is that residual stress formation is neglected. As discussed in section 1.2, SPH suffers from instabilities that become especially prominent when applied to solid mechanics. A meshfree method that promises to overcome this limitation is the Optimal Transportation Meshfree Method (OTM). LI ET AL. (2010) introduced the OTM as an Updated Lagrangian meshfree method that accounts for a broad variety of materials ranging from solids to fluids. Recently, WESSELS ET AL. (2018) have developed a rigorous phase change model accounting for both the liquid and solid phase effects in the SLM process. The model has been embedded in the OTM framework. In this work, it is extended about inelastic contributions in the solid phase to enable the prediction of residual stress formation. The continuum framework will be introduced in chapter 4 and the OTM method in chapter 6.

Thermo-metallurgical-mechanical approaches

Thermo-metallurgical-mechanical simulations can give insight into the formation of microstructure. For example, SMITH ET AL. (2016) have coupled a thermal FEM code to the CALPHAD method. With CALPHAD, thermodynamically consistent values for the heat capacity, latent heat as well as solidus and liquidus temperature can be calculated as a function of alloy composition. In addition, CALPHAD can also be used to predict face and body centered cubic phase fractions. While SMITH ET AL. (2016) only investigated the effect of temperature history on microstructure, GOLDAK & AKHLAGHI (2005) state that the latter is also influenced by the deformation history. LIAN ET AL. (2018), PANWISAWAS ET AL. (2017b) and RAI ET AL. (2016) coupled powder scale simulations to grain growth models. The ultimate goal of grain growth simulations is to establish a link to the performance behavior of as-built components: In KERGASSNER ET AL. (2018), a gradient-enhanced crystal plasticity model in combination with homogenization techniques is used to account for the influence of grain structure on mechanical properties. Recent reviews on modeling attempts to link process, microstructure and performance of finished parts can be found in YAN ET AL. (2018b) and FRANCOIS ET AL. (2017).

Surrogate modeling

KAMATH (2016) use regression trees and Gaussian process modeling to build a data driven process model fed with both experimental and simulation results. A two step modeling approach is followed in order to account for the complexity of the SLM process. In the first step, the parameter space is reduced by conducting simple simulations and experiments which consider only a few input parameters. Here, the simple model of EAGAR & TSAI (1983) introduced earlier in this section is employed. More complex simulations involving more parameters are executed in a second step, where the model of VERHAEGHE ET AL. (2009), a thermal FV simulation of SLM, is used. Due to the high cost of detailed simulations, the data available for surrogate modeling is somewhat limited. This issue is addressed in KAMATH & FAN (2018).

Data-driven techniques can also be used to approximate constitutive laws of materials with complex microstructures as they occur in SLM fabricated parts. BESSA ET AL. (2017) have developed a machine learning algorithm which is trained with results obtained from Self-Consistent Clustering Analysis (SCA) of composite materials. The method may be applied in future work to establish a link between process, structure and property, see YAN ET AL. (2018a) and YAN ET AL. (2018b).

Chapter 3

Concept of Continuum Mechanics

Continuum mechanics deals with the macroscopic behavior of materials. In this work, the field variables of interest are displacements and temperature. Based on the displacements, motion and deformation are expressed by kinematic quantities. The evolution of field variables is described with differential equations that follow from balance principles. These are valid for generic materials. Additional constitutive relations tailored to meet specific material behavior need to be formulated in order to close the system of equations. The formulation of physically meaningful constitutive models is a fundamental task in continuum mechanics. An introduction into the topic can be found e.g. in HOLZAPFEL (2010). In most cases, the solution of the resulting differential equations can not be obtained analytically, which is why numerical methods are necessary. Due to the importance of numerics for continuum mechanics, research in the field is often referred to as computational mechanics.

The outline of this chapter is as follows: The kinematic measures necessary to describe the motion and deformation of continua are defined in section 3.1. The fundamental balance laws are introduced in section 3.2. In section 3.3, the principles of continuum mechanical modeling necessary to close the system of equations are summarized.

3.1 Kinematics

When subject to motion and deformation, a body Ω can occupy different regions $\mathcal{B}$ of the Euclidean space $\mathbb{E}^3$. These regions $\mathcal{B} \subset \mathbb{E}^3$ are referred to as configurations of Ω. Tensors defined in the initial or reference configuration (e.g. at time $t = 0$) are indicated by capital letters, while tensors in the current configuration at the actual time t are written in lower case. The motion of a point belonging to Ω is a mapping from its reference position $\mathbf{X}$ to the current position $\mathbf{x}$:

$$\mathbf{x} = \boldsymbol{\chi}\left(\mathbf{X}, t\right) \tag{3.1}$$

This description follows the trajectory of a point and is referred to as the material or Lagrangian description. The motion $\boldsymbol{\chi}$ is uniquely invertible. The inverse motion yields the Eulerian or spatial formulation:

$$\mathbf{X} = \boldsymbol{\chi}^{-1}\left(\mathbf{x}, t\right) \tag{3.2}$$

Here, the observer is fixed in space and the evolution of quantities at the observation point $\mathbf{X}$ is observed. The material time derivative of an arbitrary quantity $(\bullet)$ in Lagrangian formulation is defined by:

$$\frac{\mathrm{d}\bullet(\mathbf{X},t)}{\mathrm{d}t} = \left.\frac{\partial\bullet(\mathbf{X},t)}{\partial t}\right|_{\mathbf{X}} = \dot{\bullet} \tag{3.3}$$

Quantities in the current configuration are expressed as a function of the current position $\mathbf{x}$ which itself is a function of time. Hence, the product rule applies when taking the material time derivative and a convective term appears:

$$\frac{\mathrm{d}\bullet(\mathbf{x},t)}{\mathrm{d}t} = \left.\frac{\partial\bullet(\mathbf{x},t)}{\partial t}\right|_{\mathbf{x}} + \mathrm{grad}\,(\bullet)\cdot\mathbf{v}\,(\mathbf{x},t) \tag{3.4}$$

Here, the gradient operator with respect to the current configuration and the velocity $\mathbf{v}$ have been introduced. Beside the well-known Cartesian coordinate system, tensors can be expressed in terms of curvilinear coordinates ξ^i that precisely fit the body $\mathcal{B}$. In the curvilinear coordinate system, care has to be taken about the difference between co- and contravariant quantities. They are indicated by sub- and superscript indices, respectively. Co- and contravariant basis vectors are defined in the current and in the reference configuration as:

$$\mathbf{g}_i = \frac{\partial\mathbf{x}\,(\xi^i)}{\partial\xi^i} \qquad \mathbf{g}^i = \frac{\partial\xi^i}{\partial\mathbf{x}\,(\xi^i)} \qquad \mathbf{G}_i = \frac{\partial\mathbf{X}\,(\xi^i)}{\partial\xi^i} \qquad \mathbf{G}^i = \frac{\partial\xi^i}{\partial\mathbf{X}\,(\xi^i)} \tag{3.5}$$

All tensors can be written in symbolic or in index notation with the aid of basis vectors:

$$\mathbf{x} = x_i\,\mathbf{e}_i = \bar{x}_i\,\mathbf{g}^i = x^i\,\mathbf{g}_i \tag{3.6}$$

Here, the basis vectors $\mathbf{e}_i$ of the Cartesian coordinate system have been introduced. The Cartesian basis is orthonormal and a difference between co- and contravariant does not exist. The displacement $\mathbf{u}$ is defined as the difference between the position vectors of the current and the reference configuration:

$$\mathbf{u} = \mathbf{x} - \mathbf{X} \tag{3.7}$$

Finite strains are described with the deformation gradient $\mathbf{F}$. It is a linear second order tensor which has one basis in the reference and one in the current configuration. Therefore, it maps the basis vectors from the reference into the current configuration. The determinant of $\mathbf{F}$ is known as the Jacobian J which is a measure for the volumetric deformation. It is equivalent to the ratio of volume increments $\mathrm{d}v$ and $\mathrm{d}V$ of the current and reference configuration:

$$\mathbf{F} = \frac{\partial\mathbf{x}}{\partial\mathbf{X}} = \mathbf{g}_i\otimes\mathbf{G}^i \qquad J = \det\mathbf{F} = \frac{\mathrm{d}v}{\mathrm{d}V} \tag{3.8}$$

For simplicity, it is desirable to work with symmetric tensors. Symmetry is not a property of the deformation gradient, but symmetric strain tensors can be easily defined with it. Commonly used are the left and the right Cauchy Green tensors, which are rotation free and defined in the current and reference configuration, respectively:

$$\mathbf{b} = \mathbf{F}\,\mathbf{F}^T = G^{ij}\mathbf{g}_i\otimes\mathbf{g}_j \qquad \mathbf{C} = \mathbf{F}^T\,\mathbf{F} = g_{ij}\mathbf{G}^i\otimes\mathbf{G}^j \tag{3.9}$$

In engineering applications it is advantageous to work with strain tensors which are zero in the undeformed state. This is fulfilled for the Euler-Almansi and the Green-Lagrange strain tensor $\mathbf{e}$ and $\mathbf{E}$. With the covariant unity tensors of the current and the reference configuration $\mathbf{g}^\flat = g_{ij}\,\mathbf{g}^i \otimes \mathbf{g}^j$ and $\mathbf{G}^\flat = G_{ij}\,\mathbf{G}^i \otimes \mathbf{G}^j$, $\mathbf{e}$ and $\mathbf{E}$ are defined as:

$$\mathbf{e} = \frac{1}{2}\left(\mathbf{g}^\flat - \mathbf{b}^{-1}\right) \qquad \mathbf{E} = \frac{1}{2}\left(\mathbf{C} - \mathbf{G}^\flat\right) \tag{3.10}$$

The contravariant counterparts to the unity tensors $\mathbf{g}^\flat$ and $\mathbf{G}^\flat$ are defined as $\mathbf{g}^\sharp = g^{ij}\,\mathbf{g}_i \otimes \mathbf{g}_j$ and $\mathbf{G}^\sharp = G^{ij}\,\mathbf{G}_i \otimes \mathbf{G}_j$. The stress of rate dependent materials such as fluids involves the material time derivatives of the strain tensors. Time differentiation of the Green Lagrange tensor $\mathbf{E}$ yields:

$$\dot{\mathbf{E}} = \operatorname{sym}\left(\mathbf{F}^T\dot{\mathbf{F}}\right) \qquad \dot{\mathbf{F}} = \operatorname{Grad}\dot{\mathbf{x}} \tag{3.11}$$

When taking the material time derivative of the Euler-Almansi tensor $\mathbf{e}$, the basis vectors of the current configuration also need to be differentiated. Hence, the product rule applies:

$$\dot{\mathbf{e}} = \mathbf{d} - \mathbf{l}^T\,\mathbf{e} - \mathbf{e}\,\mathbf{l} \qquad \mathbf{d} = \operatorname{sym}\mathbf{l} \qquad \mathbf{l} = \dot{\mathbf{F}}\,\mathbf{F}^{-1} \tag{3.12}$$

Here, the spatial velocity gradient $\mathbf{l}$ and its symmetric part $\mathbf{d}$ have been introduced. Another important time differentiation operator is the Lie derivative for tensors in the current configuration. It consists of a pull-back into the reference configuration, in which only the components are differentiated, and a push-forward into the current configuration:

$$\mathscr{L}_v\,\mathbf{e} = \mathbf{F}^{-T}\frac{\mathrm{d}}{\mathrm{d}t}\left(\mathbf{F}^T\,\mathbf{e}\,\mathbf{F}\right)\mathbf{F} = \mathbf{F}^{-T}\,\dot{\mathbf{E}}\,\mathbf{F}^{-1} = \mathbf{d} \tag{3.13}$$

Since only the components are differentiated, the Lie derivative is independent of the basis vectors. This property makes it an objective derivative, see also section 3.3.

3.2 Balance laws

Classical mechanics postulate the conservation of mass, linear and angular momentum. Additionally, the two laws of thermodynamics, i.e. the conservation of energy and the dissipation inequality need to be fulfilled. These balance laws are axiomatic. For simplicity, they are introduced in the current configuration only. When transferring the equations into the reference configuration, care has to be taken about the correct work conjugate pairs of stress and strain, see e.g. HOLZAPFEL (2010).

Conservation of mass

The mass m of a continuum is constant over time. It can be expressed as the integral of the density ρ over the volume with the increment $\mathrm{d}v$. Time derivation is subject to the product rule:

$$\frac{\mathrm{d}m}{\mathrm{d}t} = \frac{\mathrm{d}}{\mathrm{d}t}\int_v \rho\,\mathrm{d}v = \int_v \left(\dot{\rho} + \rho\,\operatorname{div}\mathbf{v}\right)\,\mathrm{d}v = 0 \tag{3.14}$$

The conservation of mass must hold at every point within the continuum, i.e. the volume integral can be omitted. This is referred to as local form and writes:

$$\dot{\rho} + \rho \operatorname{div} \mathbf{v} = 0 \tag{3.15}$$

Note that for incompressible fluids, the change in density is equal to zero, so that the incompressibility constraint reduces to $\operatorname{div} \mathbf{v} = 0$.

Conservation of linear momentum

The conservation of linear momentum $\mathbf{I}$ follows from Newton's second law. It states that the temporal derivative of a continuum's linear momentum is equal to the sum of exterior forces acting on it:

$$\frac{\mathrm{d}\mathbf{I}}{\mathrm{d}t} = \mathbf{F}_a + \mathbf{F}_v \tag{3.16}$$

Exterior forces are classified as surface and volume forces, denoted by $\mathbf{F}_a$ and $\mathbf{F}_v$, respectively. Analogously to mass conservation, the momentum equation is again written in integral form:

$$\frac{\mathrm{d}}{\mathrm{d}t} \int_v \rho \, \mathbf{v} \, \mathrm{d}v = \int_a \mathbf{t} \, \mathrm{d}a + \int_v \rho \, \hat{\mathbf{b}} \, \mathrm{d}v \tag{3.17}$$

Here, $\mathbf{v}$ is the velocity and $\hat{\mathbf{b}}$ the acceleration of external body forces caused e.g. by gravity. The surface traction $\mathbf{t}$ is related to the Cauchy stress $\boldsymbol{\sigma}$ via Cauchy's theorem $\mathbf{t} = \boldsymbol{\sigma} \cdot \mathbf{n}$ with $\mathbf{n}$ the normal vector to the surface. Exploiting Cauchy's and Gauss's theorem[1] and under consideration of (3.15), the conservation of linear momentum can be expressed in terms of volume integrals only. Hence, the local form can be stated as:

$$\rho \, \mathbf{a} = \operatorname{div} \boldsymbol{\sigma} + \rho \, \hat{\mathbf{b}} \tag{3.18}$$

The acceleration $\mathbf{a}$ is the material time derivative of the velocity $\mathbf{v}$. The Cauchy stress tensor $\boldsymbol{\sigma}$ is the answer of a material to its deformation. It needs to be modeled to meet specific material behavior according to the principles and concepts discussed in section 3.3.

Conservation of angular momentum

The change of angular momentum $\mathbf{L}$ with respect to a fixed point is equivalent to the exterior moments $\mathbf{M}$ of all surface and volume forces acting on a continuum:

$$\frac{\mathrm{d}\mathbf{L}}{\mathrm{d}t} = \mathbf{M}_a + \mathbf{M}_v \tag{3.19}$$

With $\mathbf{r}$ the distance from the reference fixed point to any given point $\mathbf{x}$ in space and $\dot{\mathbf{r}} = \mathbf{v}$, the integral form becomes:

$$\frac{\mathrm{d}}{\mathrm{d}t} \int_v \mathbf{r} \times \rho \mathbf{v} \; \mathrm{d}v = \int_v \mathbf{r} \times \rho \, \mathbf{a} \; \mathrm{d}v = \int_a \mathbf{r} \times \mathbf{t} \; \mathrm{d}a + \int_v \mathbf{r} \times \rho \, \hat{\mathbf{b}} \; \mathrm{d}v \tag{3.20}$$

---

[1] Gauss's theorem establishes a link between surface and volume integrals via $\int_a \boldsymbol{\sigma} \cdot \mathbf{n} \; \mathrm{d}a = \int_v \operatorname{div} \boldsymbol{\sigma} \; \mathrm{d}v$.

Here, use has been made of the identity $\dot{\mathbf{r}} \times \mathbf{v} = \mathbf{0}$. Again, Cauchy and Gauss's theorem are applied and the above relation can be rewritten in local form as:

$$\mathbf{r} \times \rho\, \mathbf{a} = \operatorname{div}(\mathbf{r} \times \boldsymbol{\sigma}) + \mathbf{r} \times \rho\, \hat{\mathbf{b}} \tag{3.21}$$

After applying the product rule and factoring out the leverage $\mathbf{r}$, the balance of linear momentum is identified on the left hand side:

$$\mathbf{r} \times \left(\rho\, \mathbf{a} - \operatorname{div} \boldsymbol{\sigma} - \rho\, \hat{\mathbf{b}}\right) = \operatorname{div} \mathbf{r} \times \boldsymbol{\sigma} = \mathbf{1} \times \boldsymbol{\sigma} = \mathbf{0} \tag{3.22}$$

Since the conservation of linear momentum (3.18) must always be fulfilled, the requirement of the balance of angular momentum reduces to $\mathbf{1} \times \boldsymbol{\sigma} = \mathbf{0}$. In index notation it can be shown that this condition holds if the stress tensor is symmetric:

$$\boldsymbol{\sigma} = \boldsymbol{\sigma}^T \tag{3.23}$$

The symmetry condition must be implicitly fulfilled by any constitutive model. Therefore the conservation of angular momentum does not yield another equation that needs to be solved.

Conservation of energy

The total energy E can be additively split into a mechanical part K and the internal energy U. The evolution of mechanical energy is equal to the power of external forces P_{ext} reduced about the internal work P_{int}. The change of the total energy E of a system equals the sum of the power of external forces and the power of the introduced heat Q:

$$\frac{\mathrm{d}K}{\mathrm{d}t} = P_{ext} - P_{int} \qquad \text{and} \qquad \frac{\mathrm{d}E}{\mathrm{d}t} = P_{ext} + Q \tag{3.24}$$

Inserting the split $E = K + U$ into $(3.24)_2$ and making use of $(3.24)_1$, the energy equation can be expressed as evolution of internal energy U:

$$\frac{\mathrm{d}U}{\mathrm{d}t} = P_{int} + Q \tag{3.25}$$

The internal work is defined as the volume integral of the double scalar product of stress $\boldsymbol{\sigma}$ and stretch tensor $\mathbf{d}$. Heat can be exchanged with the system via a surface heat flux $\mathbf{q}$ and through a volumetric source term r:

$$P_{int} = \int_v \boldsymbol{\sigma} : \mathbf{d}\ \mathrm{d}v \qquad \text{and} \qquad Q = -\int_a \mathbf{q} \cdot \mathbf{n}\, \mathrm{d}a + \int_v \rho\, r\ \mathrm{d}v \tag{3.26}$$

When applying Gauss's theorem, the energy equation can again be written in the local form:

$$\rho\, \dot{u} = \boldsymbol{\sigma} : \mathbf{d} - \operatorname{div} \mathbf{q} + \rho\, r \tag{3.27}$$

Here, $\dot{u}$ is the rate of internal energy per unit mass. The final form of the energy equation is obtained after incorporating the requirements from the dissipation inequality introduced next.

Dissipation inequality

The second law of thermodynamics restricts the driving direction of processes from states with lower towards states with greater disorder. The measure of microscopic disorder is the entropy S. The entropy production Σ is the rate of entropy minus the externally introduced entropy $\bar{Q}$:

$$\Sigma = \frac{\mathrm{d}}{\mathrm{d}t} S - \bar{Q} \geq 0 \tag{3.28}$$

In integral form, the mass specific entropy production σ_d and the entropy s are introduced. Entropy can be exchanged with a system via surface fluxes $\mathbf{h}$ or an internal source term η:

$$\int_v \rho\, \sigma_d \;\mathrm{d}v = \int_v \rho\, \dot{s} \;\mathrm{d}v + \int_a \mathbf{h} \cdot \mathbf{n} \,\mathrm{d}a - \int_v \rho\, \eta \;\mathrm{d}v \geq 0 \tag{3.29}$$

The externally contributed entropy is assumed to be inversely proportional to temperature via $\mathbf{h} = \theta^{-1}\,\mathbf{q}$ and $\eta = r^s/\theta$. Inserting these assumptions into (3.29), applying Gauss's theorem and the product rule of differentiation, the dissipation inequality writes in local form:

$$\rho\, \sigma_d = \rho\, \dot{s} + \frac{1}{\theta}\,\mathrm{div}\,\mathbf{q} - \frac{1}{\theta^2}\mathbf{q}\,\mathrm{grad}\,\theta - \frac{1}{\theta}\rho\, r^s \geq 0 \tag{3.30}$$

The third term on the right hand side of the above relation is entropy production caused by thermal conduction. Since heat is flowing from higher towards lower temperatures, it can never achieve negative values. Therefore, the inequality must hold without this term as well. Multiplying the remaining terms with the temperature yields the definition of dissipation D_{int}. An alternative expression can be obtained by substituting $(\mathrm{div}\,\mathbf{q} - \rho\, r)$ from the energy equation (3.27):

$$\begin{aligned} D_{int} &= \rho\, \theta\, \dot{s} + \mathrm{div}\,\mathbf{q} - \rho\, r^s \\ &= \rho\, \theta\, \dot{s} + \boldsymbol{\sigma} : \mathbf{d} - \rho \dot{u} \geq 0 \end{aligned} \tag{3.31}$$

The internal energy u is related to the free energy ψ via the Legendre transformation:

$$u = \psi + \theta\, s \tag{3.32}$$

In practice, it is more convenient to model the free energy functional instead of the internal energy. Substituting u in the dissipation inequality (3.31) by the transformation (3.32) yields:

$$D_{int} = \boldsymbol{\sigma} : \mathbf{d} - \rho\, \dot{\psi} - \rho\, \dot{\theta}\, s \geq 0 \tag{3.33}$$

For compressible thermo-mechanical continua, the primary variables consist of the displacements and the temperature. It is then sufficient to solve the balance of linear momentum (3.18) and energy $(3.31)_1$. Nevertheless, the system of equations must be complemented with appropriate constitutive assumptions subject to rules discussed in section 3.3.

3.3 Guidelines for Constitutive Modeling

Constitutive modeling must respect mathematical and physical requirements. Therefore, rules and standards have been formulated which are described in detail in standard text books such as TRUESDELL & NOLL (2004), HAUPT (1977) and LEHMANN (1984). A summary can be found in MIEHE (1988). The most important aspects are:

1. Determinism
2. Local action
3. Material frame indifference
4. Material symmetry
5. Dissipation postulate
6. Equi-presence
7. Multiplicative decomposition
8. Concept of internal variables
9. Fading memory

The first two principles state that all thermo-mechanical measures at a material point are determined by the history of the primary variables within an arbitrary neighborhood. The third principle requires the material response to be independent of the observer, i.e. the reference frame. These first three principles are valid for the class of simple materials according to Walter Noll (TRUESDELL & NOLL, 2004).

Symmetry properties may be used to simplify the formulation of constitutive equations. A fundamental requirement is that constitutive equations must fulfill the dissipation inequality (3.33) of the second law of thermodynamics. Equi-presence means that all thermo-mechanical measures shall contain the same set of variables. The multiplicative decomposition is useful to decouple the deformation gradient into contributions related to different physics. The concept of internal variables is employed to model history dependent, e.g. plastic behavior. The principle of fading memory states that the history of primary variables in the distant past has less or no influence on the current thermo-mechanical measures.

In agreement with these principles, a thermo-mechanical model that incorporates the physical phenomena relevant to the powder scale of SLM will be formulated in the next chapter.

Chapter 4

A Thermo-Mechanical Model of SLM

Various thermo-mechanical material models for phase change problems exist in the literature. For example, in welding simulations a phase change from solid to liquid and vice versa has to be taken into account. Detailed overviews of Computational Welding Mechanics (CWM) can be found for instance in GOLDAK & AKHLAGHI (2005) and LINDGREN (2007). Another well-known industrial process including phase change is casting. Casting simulations aiming to predict residual stress formation often neglect the fluid dynamics of mold filling and start after the mold has been filled. Such a thermo-mechanical modeling approach for casting has been developed in CHIUMENTI (1998), AGELET DE SARACIBAR ET AL. (1999) and CERVERA ET AL. (1999), for instance. The deformations in both welding and casting are usually small and therefore an additive split of strains was sufficient in the aforementioned publications. However, the small strain assumption is not applicable on the powder scale of SLM. To overcome this limitation, a finite deformation phase change formulation for SLM powder scale simulations has been developed in WESSELS ET AL. (2018). This concept is described in section 4.1. The remainder of this chapter is structured as follows: A free energy potential is formulated in section 4.2. To account for residual stress formation, inelastic contributions to the deformation are modeled with elasto-plastic and elasto-visco-plastic constitutive equations, see sections 4.2.1 and 4.2.2, respectively. The resulting governing equations are summarized in section 4.3 and completed with surface tension and recoil pressure as Neumann boundary conditions in sections 4.3.1 and 4.3.2.

4.1 Finite Deformation Phase Change Approach

The phase change approach presented in WESSELS ET AL. (2018) is based on the following observations: Melting of metal results in an untying of internal bonds. Consequently, internal stresses are released. Once the metal becomes liquid, irreversible viscous deformation occurs. The mechanical volumetric deformation in the liquid phase due to external forces can be considered negligible compared to the thermal expansion. During consolidation from liquid to solid, internal links allowing the material to store isochoric elastic energy are created.

First, the kinematics of the solid phase are described. In the lower temperature regime, the plastic deformation can be regarded as rate independent. At higher temperatures, the yield limit gradually decreases and rate dependent plastic deformation occurs. As suggested by Goldak & Akhlaghi (2005), this behavior can be captured with an elasto-plastic model up to a homologous temperature $\theta/T_{melt} = 0.5$ and from there on with an elasto-visco-plastic model until the melting temperature is reached. Following the concept of multiplicative decomposition (section 3.3), the deformation gradient $\mathbf{F}$ is split into a reversible $\mathbf{F}_{rev}$ and an irreversible plastic part $\mathbf{F}_p$. The reversible part consists of an elastic and a thermal contribution as stated e.g. in Wriggers et al. (1992):

$$\mathbf{F} = \mathbf{F}_{rev}\,\mathbf{F}_p = \mathbf{F}_e\,\mathbf{F}_\theta\,\mathbf{F}_p \tag{4.1}$$

The thermal deformation is related to thermal expansion and is purely volumetric. Assuming plastic incompressibility in the frame of von-Mises plasticity yields a purely isochoric plastic deformation gradient, i.e. $J_p = 1$. Hence, the Jacobi determinant J is split into a thermal part J_θ and an elastic part J_e:

$$J = J_e\,J_\theta \qquad J_\theta = e^{3\alpha_\theta(\theta-\theta_0)} \tag{4.2}$$

The thermal part of the Jacobi determinant J_θ incorporates the thermal expansion coefficient α_θ, the temperature θ and the reference temperature θ_0 (Lu & Pister, 1975). In order to account for phase change related straining, the thermal expansion coefficient α_θ is defined as a function of temperature (Goldak & Akhlaghi, 2005). Making use of (4.1) and (4.2), the split of the deformation gradient into a volumetric component $\mathbf{F}_{vol}$ and an isochoric part $\mathbf{F}_{iso}$ is defined for the solid phase by:

$$\mathbf{F} = \mathbf{F}_{vol}\,\mathbf{F}_{iso} \qquad \mathbf{F}_{vol} = (J_\theta\,J_e)^{\frac{1}{3}}\,\mathbf{1} \qquad \mathbf{F}_{iso}\,(\phi = 1) = J_e^{-\frac{1}{3}}\,\mathbf{F}_e\,\mathbf{F}_p \tag{4.3}$$

Here, the phase indicator ϕ has been introduced and $\mathbf{1}$ denotes the unity tensor.. Powder and consolidated material is assigned $(\phi = 1)$ while the liquid phase is identified from $(\phi = 0)$. The mechanical volumetric deformation in the powder as well as in the liquid phase is deemed negligible: In the powder phase, no external mechanical loads exist while the fluid phase is modeled as mechanically weakly incompressible. Hence, volumetric deformation is mainly caused by thermal expansion which must be preserved in the presence of a phase change. Consequently, this yields to the assumption that only isochoric deformation is phase dependent. In the liquid phase, the isochoric deformation is purely viscous and therefore irreversible:

$$\mathbf{F}_{iso}\,(\phi = 0) = \mathbf{F}_v \tag{4.4}$$

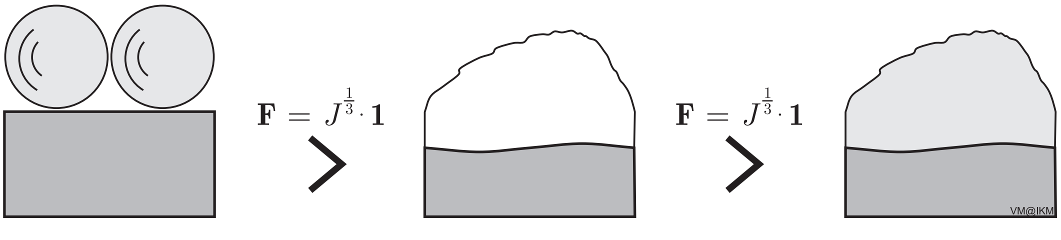
$\mathbf{F} = J^{\frac{1}{3}}\cdot\mathbf{1}$
$\mathbf{F} = J^{\frac{1}{3}}\cdot\mathbf{1}$
VM@IKM

Figure 4.1. When a phase change occurs, the isochoric deformation gradient $\mathbf{F}_{iso}$ is set equal to one. Only the volumetric part $\mathbf{F}_{vol}$ remains. Left: Metal powder. Centered: Molten metal. Right: Consolidated metal.

At this stage, the following phase change treatment is applied: once metal changes phase, the isochoric deformation gradient is set equal to the unity tensor. This corresponds to equating the deformation gradient with its volumetric part:

$$\mathbf{F}_{iso} = \mathbf{1} \qquad \mathbf{F} = \mathbf{F}_{vol} = J^{\frac{1}{3}}\mathbf{1} \tag{4.5}$$

In other words, the isochoric deformation gradient has a fading memory due to the phase change. A graphical illustration of the concept can be found in figure 4.1. Note that with the suggested approach, isochoric free energy is destroyed during the phase change from powder to liquid. However, the deformation in the powder phase is mostly related to volumetric thermal expansion. Hence, in the presence of latent heat the loss of isochoric free energy is deemed negligible.

Remark: *For casting simulations,* CHIUMENTI *(1998) suggests the solution of an evolution equation to ensure that viscous deformation in the liquid phase does not yield any stresses in the consolidated phase. This model has been developed for casting and only accounts for the consolidation from liquid to solid. Furthermore, it is limited to small deformations, where an additive split of the strain tensor is sufficient.* REESE & GOVINDJEE *(1998) have introduced a finite visco-elasticity formulation. In combination with finite thermo-plasticity it could be used to generalize the work of* CHIUMENTI *(1998) to the finite deformation regime. However, in SLM also melting must be considered. To capture the elastic deformation in the powder phase, an additional evolution equation would be required. The method presented in* WESSELS ET AL. *(2018) based on the fading memory of the isochoric deformation gradient is computationally far more efficient.*

4.2 Constitutive Model for the Phase Change Problem

Following the concept of LU & PISTER (1975), the free energy potential ψ is decomposed into a volumetric, an elastic isochoric, a plastic hardening and a thermal part ψ_{vol}, ψ_{iso}, ψ_{plas} and T, respectively. The thermo-elastic material has been described in MIEHE (1988) and an extension to associative plasticity can be found in SIMO & MIEHE (1992). The formulation of an uncoupled free energy potential requires an uncoupling of the strain measures. Reversible strains are described with the left Cauchy Green tensor $\mathbf{b}_{rev}$ defined in the current configuration, see SIMO & MIEHE (1992):

$$\mathbf{b}_{rev} = \mathbf{F}_{rev}\mathbf{F}_{rev}^{T} = \mathbf{F}\,\mathbf{C}_p^{-1}\,\mathbf{F}^{T} \qquad \mathbf{C}_p = \mathbf{F}_p^{T}\,\mathbf{F}_p, \tag{4.6}$$

The isochoric reversible left Cauchy Green tensor $\bar{\mathbf{b}}_e$ is purely elastic and defined as:

$$\bar{\mathbf{b}}_e = J^{-\frac{2}{3}}\mathbf{b}_{rev} \tag{4.7}$$

The free energy potential ψ can now be expressed as a function of the uncoupled strain measures J_e and $\bar{\mathbf{b}}_e$, the temperature θ and the plastic hardening variable α which will be defined later on in section 4.2.1:

$$\rho_0\,\psi = \rho_0\,\psi_{vol,e}\,(J_e) + \rho_0\,\psi_{iso,e}\left(\bar{\mathbf{b}}_e\right) + T\,(\theta) + \rho_0\psi_{plas}\,(\alpha) \tag{4.8}$$

Here, ρ_0 is the initial or reference density. Assuming a Neo-Hookean thermo-elastic material in the elastic region, the elastic volumetric and isochoric part of the free energy write (MIEHE, 1988):

$$\rho_0 \psi_{vol,e} = \frac{1}{2} K(\theta) (\ln J_e)^2 \qquad \rho_0 \psi_{iso,e} = \frac{1}{2} \phi \, \mu(\theta) \left(I_{\bar{\mathbf{b}}_e} - 3 \right) \tag{4.9}$$

The variable ϕ is again the phase indicator. In the solid phase ($\phi = 1$), elastic energy is stored. The isochoric viscous deformation in the liquid phase ($\phi = 0$) dissipates energy and therefore does not yield any contribution to the free energy potential. Also the first invariant $I_{\bar{\mathbf{b}}_e} = \operatorname{tr} \bar{\mathbf{b}}_e$ of the isochoric elastic left Cauchy Green tensor and the second Lamé constant $\mu(\theta)$ have been introduced. Using a temperature dependent compression modulus $K(\theta)$, the above stated volumetric free energy function is valid throughout all phases. For liquid metal, K is chosen as high as necessary to ensure mechanical incompressibility in a weak sense. Following the notation of CERVERA ET AL. (1999), the unknown function $T(\theta)$ in equation (4.8) is identified by means of the heat capacity c at constant deformation modified about the latent heat contribution c_{L_θ}:

$$c(\theta) + c_{L_\theta} = -\theta \frac{\partial^2 \psi}{\partial \theta^2} = -\theta \left[\frac{\partial^2 \psi_{vol,e}}{\partial \theta^2} + \frac{1}{\rho_0} \frac{\partial^2 T(\theta)}{\partial \theta^2} \right] \tag{4.10}$$

Details on the definition of the latent heat contribution c_{L_θ} are given in the remark below. When differentiating $\psi_{vol,e}$ with respect to temperature, care has to be taken about the temperature dependency of material parameters. Here, all terms involving the derivation of material parameters are neglected. For completeness, the exact differentiation is given in appendix A. The simplified derivatives write:

$$\frac{\partial \psi_{vol,e}}{\partial \theta} \approx -K (\ln J_e) 3\alpha_\theta \qquad \frac{\partial^2 \psi_{vol,e}}{\partial \theta^2} \approx K (3\alpha_\theta)^2 \tag{4.11}$$

The integration of (4.10) over temperature with respect to temperature dependent material parameters would again yield terms which are neglected in the present analysis. With this simplification, rearranging and integrating (4.10) yields:

$$T(\theta) \approx -(3\alpha_\theta)^2 K (\theta - \theta_0)^2 - \rho_0 (c + c_{L_\theta}) \left(\theta \ln \frac{\theta}{\theta_0} - (\theta - \theta_0) \right) \tag{4.12}$$

The latent heat is absorbed when metal transitions from solid to liquid or from liquid to gas and released during condensation and consolidation. It delays the temperature evolution in both directions of a phase change. The phase change problem is analytically described by the Stefan-Neumann equations, see e.g. HU & ARGYROPOULOS (1996). If the position of the interface is not explicitly needed, it is numerically more feasible to only track the volume in which a phase change occurs. An overview of such numerical methods can be found in POIRIER & SALCUDEAN (1988).

Remark: *The treatment of the latent heat effect in (4.10) is analogous to the apparent heat capacity method introduced by* BONACINA ET AL. *(1973) and recently studied by*

MUHIEDDINE ET AL. *(2009). It is most appropriate for materials that change phase over a temperature range between a solidus (bubble) and a liquidus (dew) temperature* T_{sol} (T_{bub}) *and* T_{liq} (T_{dew})*, respectively. The latent heat of melting* L_m *and vaporization* L_v *is absorbed in these temperature intervals. The latent heat contribution* c_{L_θ} *introduced in (4.10) can then be obtained from the quotient of latent heat* L_m *or* L_v *and the respective temperature interval* ΔT*. For materials that experience congruent melting (vaporization), i.e. whose components all have a single melting (vaporization) point* T_m (T_v)*, the temperature remains constant during a phase change. This is the case for the solid line in figure 4.2 (right). For this type of material it is more appropriate to formulate the energy equation in terms of the enthalpy and to use the latent heat accumulation method as described by* MUHIEDDINE ET AL. *(2009). In the latter, the energy equation is expressed as a function of latent heat as primary variable. Since in the present work a coupled thermo-mechanical problem is solved where the stress is a function of temperature, the apparent heat capacity method is preferred. The concept is illustrated in figure 4.2.*

The contribution from linear isotropic plastic hardening to the free energy functional (4.8) is, see e.g. WRIGGERS (2008):

$$\rho_0\psi_{plas}(\alpha) = \frac{1}{2}\,H_\alpha(\theta)\,\alpha^2 \tag{4.13}$$

Here, α is the plastic hardening variable. The concept of elasto-(visco)-plasticity will be discussed later on. The free energy functional (4.8) is now fully defined with the volumetric and isochoric contributions from (4.9), the thermal part (4.12) and the hardening term (4.13):

$$\begin{aligned}
\rho_0\psi(\mathbf{b}_{rev},\theta,\alpha) &= \underbrace{\frac{1}{2}K(\ln J_e)^2}_{\rho_0\psi_{vol,e}} + \underbrace{\frac{1}{2}\phi\,\mu\,(I_{\bar{\mathbf{b}}_e}-3)}_{\rho_0\psi_{iso,e}} + \underbrace{\frac{1}{2}\,H_\alpha\alpha^2}_{\rho_0\psi_{plas}} \\
&\quad \underbrace{-\frac{1}{2}(3\alpha)^2K(\theta-\theta_0)^2 - \rho_0(c+c_{L_\theta})\left(\theta\ln\frac{\theta}{\theta_0}-(\theta-\theta_0)\right)}_{T} \\
&= \underbrace{\frac{1}{2}K(\ln J)^2}_{\rho_0\psi_{vol}} + \underbrace{\frac{1}{2}\phi\,\mu\,(I_{\bar{\mathbf{b}}_e}-3)}_{\rho_0\psi_{iso,e}} + \underbrace{\frac{1}{2}\,H_\alpha\alpha^2}_{\rho_0\psi_{plas}} \\
&\quad \underbrace{-\,3\,\alpha K\,(\ln J)\,(\theta-\theta_0) - \rho_0(c+c_{L_\theta})\left(\theta\ln\frac{\theta}{\theta_0}-(\theta-\theta_0)\right)}_{T_2}
\end{aligned} \tag{4.14}$$

The link between the two alternative decompositions of ψ (4.14) is established by inserting the definition of J_e from (4.2) into the volumetric free energy $\psi_{vol,e}$. For the sake of brevity, the temperature dependency of material parameters has not been explicitly written in the above equation. The material time derivative of the free energy functional is obtained from partial differentiation of (4.14):

$$\dot{\psi} = \frac{\partial\psi}{\partial\mathbf{b}_{rev}} : \dot{\mathbf{b}}_{rev} + \frac{\partial\psi}{\partial\theta}\dot{\theta} + \frac{\partial\psi}{\partial\alpha}\dot{\alpha} \tag{4.15}$$

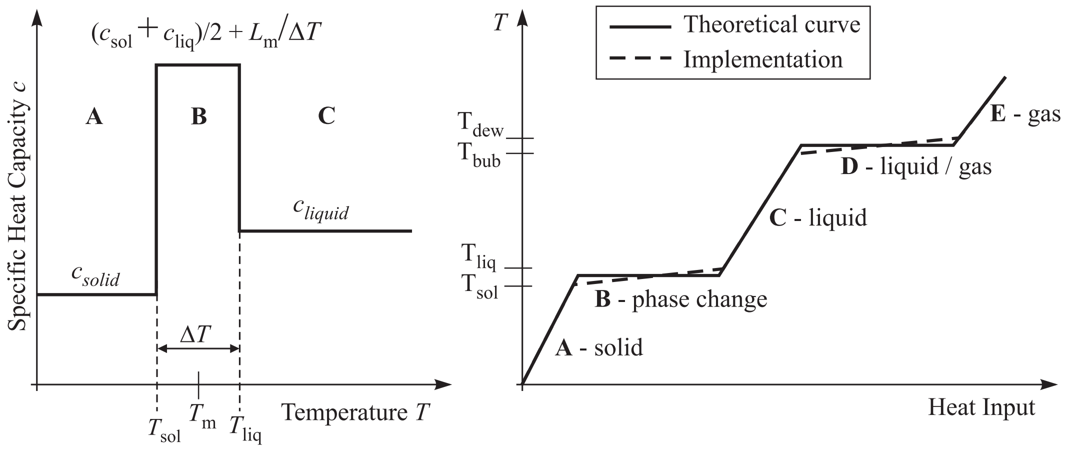

Figure 4.2. Comparison of latent heat treatment adapted from GANERIWALA & ZOHDI (2016). Left: In the apparent heat capacity method, the heat capacity is a function of temperature. Right: The temperature is a function of the heat input. Dashed line: Apparent heat capacity method. Solid line: Accumulated enthalpy method.

Here, the material time derivative of the reversible left Cauchy Green tensor $\mathbf{b}_{rev}$ is required. From its definition (4.6) it follows:

$$\dot{\mathbf{b}}_{rev} = \underbrace{\mathbf{l}\mathbf{b}_{rev} + \mathbf{b}_{rev}\mathbf{l}^T}_{2\mathbf{l}\cdot\mathbf{b}_{rev}} + \underbrace{\mathbf{F}\dot{\mathbf{C}}_p\mathbf{F}^T}_{\mathscr{L}_v\mathbf{b}_{rev}} \tag{4.16}$$

In the above expression, the Lie derivative $\mathscr{L}_v$ introduced in (3.13) has been identified and the symmetry of $\mathbf{b}_{rev}$ has been exploited. Inserting (4.15) into the dissipation inequality (3.33) and making use of the property of the double scalar product to filter antisymmetric terms yields the Gibbs relation, see e.g. HOLZAPFEL (2010) or SIMO & MIEHE (1992):

$$D_{int} = \left(\boldsymbol{\sigma} - 2\rho\frac{\partial\psi}{\partial\mathbf{b}_{rev}}\mathbf{b}_{rev}\right) : \mathbf{d} - \rho\left(s + \frac{\partial\psi}{\partial\theta}\right)\dot{\theta} - \rho\frac{\partial\psi}{\partial\mathbf{b}_{rev}} : \mathscr{L}_v\mathbf{b}_{rev} - \rho\frac{\partial\psi}{\partial\alpha}\dot{\alpha} \geq 0 \tag{4.17}$$

In the following, the constitutive equations for stress and entropy are identified by equating the terms in the brackets to zero. The remaining dissipation D_{int} will be addressed in section 4.2.3.

Entropy

The entropy is identified by equating the second bracket in (4.17) to zero. As in the definition of the heat capacity (4.10), the temperature dependency of material parameters is neglected in the differentiation of ψ with respect to temperature:

$$s = -\frac{\partial\psi}{\partial\theta} = \frac{3\alpha K}{\rho_0}\ln J + (c + c_{L_\theta})\ln\frac{\theta}{\theta_0} \tag{4.18}$$

For completeness, the correct derivative of the free energy function (4.14) with respect to temperature is given in appendix A. The material time derivative of entropy (4.18) is obtained by applying the chain rule:

$$\dot{s} = -\frac{\partial^2 \psi}{\partial \mathbf{b}_{rev} \partial \theta} : \dot{\mathbf{b}}_{rev} - \frac{\partial^2 \psi}{\partial \theta^2} \dot{\theta} - \frac{\partial^2 \psi}{\partial \alpha \partial \theta} \dot{\alpha} \tag{4.19}$$

Since the temperature dependency of the isotropic plastic hardening modulus H_α is neglected, the term on the most right hand side in (4.19) becomes zero. Taking the remaining partial and material time derivatives in the above statement, implementing the definition of the heat capacity (4.10) and multiplying with $(\rho\theta)$ yields the entropy work $(\rho\theta\dot{s})$ which is needed in the energy equation $(3.31)_1$:

$$\rho\theta\dot{s} = \frac{3\alpha K}{J} \theta \operatorname{tr} \mathbf{d} + \rho \left(c + c_{L_\theta} \right) \dot{\theta} \tag{4.20}$$

The first term on the right hand side of (4.20) is heating due to elastic volumetric deformation which is known as the Gough-Joule effect (HOLZAPFEL, 2010). In SLM, deformation in the solid phase is mostly due to thermal expansion while in the liquid phase the melt is assumed as mechanically weakly incompressible. Hence, the trace of the stretch tensor $\mathbf{d}$ is nearly zero and the effect is neglected.

Stress

The Cauchy stress tensor $\boldsymbol{\sigma}$ is identified from the first term in (4.17). The derivation of ψ with respect to $\mathbf{b}_{rev}$ yields the split of the stress tensor into a hydrostatic part, defined by the pressure p, and a phase dependent deviatoric part $\mathbf{s}(\phi)$:

$$\boldsymbol{\sigma} = 2\rho \mathbf{b}_{rev} \frac{\partial \psi}{\partial \mathbf{b}_{rev}} = -p\, \mathbf{g}^\sharp + \mathbf{s}(\phi) \tag{4.21}$$

In the above equation, $\mathbf{g}^\sharp$ denotes the contravariant unity tensor introduced in section 3.1. The pressure p can be derived throughout all phases from the volumetric free energy potential $\psi_{vol,e}$ defined in $(4.9)_1$ using the chain rule of differentiation:

$$-p = 2\rho \mathbf{b}_{rev} \frac{\partial \psi_{vol,e}}{\partial \mathbf{b}_{rev}} = \frac{\rho_0}{J_\theta} \frac{\partial \left(\psi_{vol,e}\left(J_e \right) \right)}{\partial J_e} = \frac{K}{J} \ln J_e \tag{4.22}$$

In the solid phase ($\phi = 1$), isochoric elastic energy is stored. The elastic deviatoric stress is derived from $(4.9)_2$ as:

$$\begin{aligned} \mathbf{s}(\phi = 1) &= \frac{2}{J} \rho \left[\bar{\mathbf{b}}_e \cdot \frac{\partial \left(\rho_0 \psi_{iso,e}\left(\bar{\mathbf{b}}_e \right) \right)}{\partial \bar{\mathbf{b}}_e} - \frac{1}{3} \left(\frac{\partial \left(\rho_0 \psi_{iso,e}\left(\bar{\mathbf{b}}_e \right) \right)}{\partial \bar{\mathbf{b}}_e} : \bar{\mathbf{b}}_e \right) \mathbf{g}^\sharp \right] \\ &= \frac{\mu}{J} \left(\bar{\mathbf{b}}_e - \frac{1}{3} \left(\operatorname{tr} \bar{\mathbf{b}}_e \right) \mathbf{1} \right) \end{aligned} \tag{4.23}$$

Details on the derivations (4.22) and (4.23) can be found in HOLZAPFEL (2010) and MIEHE (1988). The isochoric fluid flow in the liquid phase is dissipative and does not contribute to the free energy functional. Viscous stresses are defined by:

$$\mathbf{s}(\phi = 0) = \frac{2\,\eta}{J} \left(\mathbf{d} - \frac{1}{3} \left(\operatorname{tr} \mathbf{d} \right) \mathbf{g}^\sharp \right) \tag{4.24}$$

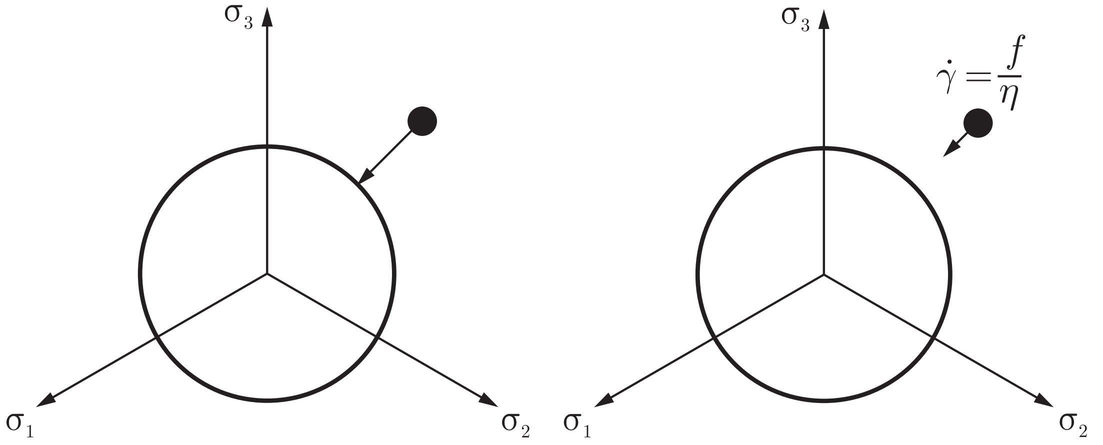

(a) Elasto-plasticity (b) Visco-plasticity (Bingham fluid)

Figure 4.3. Elasto-(visco)-plastic return mapping. Contrary to rate independent plasticity, in a rate dependent formulation the yield function may be violated in the converged state. The amount of plastic flow in direction of the yield surface follows an additional constitutive equation.

In the subsequent sections 4.2.1 and 4.2.2, the additional constitutive equations for elasto-(visco)-plasticity will be presented. Additional assumptions on the remaining dissipation D_{int} will be discussed in section 4.2.3.

4.2.1 Elasto-Plasticity

In elasto-plasticity, the material behaves elastically until a material dependent stress limit is reached. Beyond that limit, called the yield limit, the resistance to deformation dramatically decreases, that is the material is allowed to flow. The yield limit may increase proportional to the accumulated plastic strain which is called hardening. At higher temperatures, the yield limit decreases, which is referred to as thermal softening. A comprehensive overview of thermo-elasto-plasticity is given in SIMO & MIEHE (1992) and a condensed review on elasto-plasticity can be found in KORELC & STUPKIEWICZ (2014).

The evolution of plastic flow needs to be modeled with an additional constitutive equation. Using standard J_2 von-Mises plasticity with isotropic strain hardening and thermal softening, the yield function $f(\boldsymbol{\tau}, \theta, \alpha)$ is expressed in terms of Kirchhoff stress $\boldsymbol{\tau} = J\boldsymbol{\sigma}$, temperature θ and an internal hardening variable α:

$$f(\boldsymbol{\tau}, \theta, \alpha) = \sqrt{\frac{3}{2}} || \operatorname{dev} \boldsymbol{\tau} || - [\sigma_{Y0}(\theta) - \hat{q}(\theta)] \leq 0 \tag{4.25}$$

Here, $\sigma_{Y0}(\theta)$ is the temperature dependent yield limit of the undeformed body and $\hat{q}(\theta)$ denotes the hardening stress. The latter is identified from the last term in (4.17) as the first derivative of the free energy potential with respect to α. Since f is written in terms of Kirchhoff stress $\boldsymbol{\tau}$, the last term in (4.17) is also multiplied with the Jacobian J:

$$\hat{q} = -J\rho \frac{\partial \psi_{plas}(\alpha)}{\partial \alpha} = -H_\alpha(\theta)\, \alpha \tag{4.26}$$

Both $\sigma_{Y0}(\theta)$ and $\hat{q}(\theta)$ are assumed to depend linearly on temperature. The slope is prescribed by the thermal softening modulus $H_\theta = (T_m - \theta_0)^{-1}$ which is chosen such that the yield limit vanishes at the melting point:

$$\begin{aligned} \sigma_{Y0}(\theta) &= \sigma_{Y0}(\theta_0)\left[1 - H_\theta(\theta - \theta_0)\right] \\ \hat{q}(\theta) &= H_\alpha(\theta)\,\alpha = H_\alpha(\theta_0)\left[1 - H_\theta(\theta - \theta_0)\right]\alpha \end{aligned} \tag{4.27}$$

Based on the multiplicative split of the deformation gradient into a reversible $\mathbf{F}_{rev}$ and an irreversible plastic contribution $\mathbf{F}_p$ from (4.1), an evolution equation for the plastic flow can be formulated. Taking the material time derivative of $\mathbf{C}_p^{-1}$ yields:

$$\dot{\overline{\mathbf{C}_p^{-1}}} = -2\,\mathbf{F}_p^{-1}\,\tilde{\mathbf{D}}_p\,\mathbf{F}_p^{-T} = -2\,\mathbf{F}^{-1}\,\mathbf{d}_p\,\mathbf{F}\,\mathbf{C}_p^{-1} \tag{4.28}$$

Here, $\tilde{\mathbf{D}}_p$ is the plastic stretch tensor defined in the intermediate and $\mathbf{d}_p$ its counterpart in the current configuration. It is the symmetric part of the plastic velocity gradient $\tilde{\mathbf{L}}_p$ (or accordingly $\mathbf{l}_p$) defined by:

$$\tilde{\mathbf{L}}_p = \dot{\mathbf{F}}_p\,\mathbf{F}_p^{-1}, \qquad \mathbf{l}_p = \mathbf{l} - \mathbf{l}_e = \mathbf{F}_e\,\tilde{\mathbf{L}}_p\,\mathbf{F}_e^{-1} \quad \text{with} \quad \mathbf{l} = \dot{\mathbf{F}}\,\mathbf{F}^{-1}, \qquad \mathbf{l}_e = \dot{\mathbf{F}}_e\,\mathbf{F}_e^{-1} \tag{4.29}$$

An additional constitutive assumption enforces the plastic spin, i.e. the asymmetric part of the plastic velocity gradient, to be equal to zero. Per consequence, the plastic velocity gradient $\tilde{\mathbf{L}}_p$ is equal to the plastic stretch tensor $\tilde{\mathbf{D}}_p$ (and correspondingly $\mathbf{l}_p = \mathbf{d}_p$). In the current configuration, the evolution of plastic strain can now be formulated in terms of the plastic stretch tensor $\mathbf{d}_p$:

$$\mathbf{d}_p = \dot{\gamma}\,\mathbf{n} \qquad \mathbf{n} = \frac{\partial f}{\partial \boldsymbol{\tau}} = \sqrt{\frac{3}{2}}\frac{\operatorname{dev}\boldsymbol{\tau}}{||\operatorname{dev}\boldsymbol{\tau}||} \tag{4.30}$$

Here, $\dot{\gamma}$ is the plastic multiplier and $\mathbf{n}$ the normal to the yield surface. It defines the direction in which the stress is back-projected while $\dot{\gamma}$ controls the amount of plastic flow. In the present case of associative plasticity, $\mathbf{n}$ is obtained by deriving the yield function with respect to the Kirchhoff stress $\boldsymbol{\tau}$. The evolution of the hardening variable α is obtained from the first derivative of the yield function f with respect to the hardening stress $\hat{q}$:

$$\dot{\alpha} = \dot{\gamma}\frac{\partial f}{\partial \hat{q}} = \dot{\gamma} \tag{4.31}$$

The problem is complemented with the consistency conditions of Kuhn-Tucker type:

$$\dot{\gamma} \geq 0, \quad f(\boldsymbol{\tau}, \alpha, \theta) \leq 0, \quad \dot{\gamma} f(\boldsymbol{\tau}, \alpha, \theta) = 0 \tag{4.32}$$

4.2.2 Elasto-Visco-Plasticity

The key difference of elasto-visco-plasticity to elasto-plasticity is that the plastic behavior is rate dependent. This enables the description of phenomena such as creep where plastic flow occurs under constant loading conditions. In elasto-visco-plasticity, the yield limit may be

From the energy functional (4.14), heat capacity and entropy are defined by:

$$c + c_{L_\theta} = -\theta \frac{\partial^2 \psi}{\partial \theta^2}, \qquad s = -\frac{\partial \psi}{\partial \theta}$$

Isotropic Fourier type heat conduction

$$\mathbf{q} = -k \operatorname{grad} \theta$$

Kinematics: Multiplicative split of $\mathbf{F}$ and fading memory of $\mathbf{F}_{iso}$

$$\mathbf{F}_{vol} = J^{\frac{1}{3}} \mathbf{1} \qquad \text{solid: } \mathbf{F}_{iso} = J_e^{-\frac{1}{3}} \, \mathbf{F}_e \, \mathbf{F}_p \qquad \text{liquid: } \mathbf{F}_{iso} = \mathbf{F}_v \qquad \text{If change of phase: } \mathbf{F}_{iso} = \mathbf{1}$$

Constitutive law as a function of temperature

- If $(\theta > T_{liq})$: Viscous Kirchhoff stress in liquid phase

  $$\boldsymbol{\tau} = K \, \ln J_e + 2 \, \eta \operatorname{dev} \mathbf{d}$$

- Else if $(\theta < T_{liq})$:

  1. Elastic Kirchhoff stress in solid phase

     $$\boldsymbol{\tau} = K \, \ln J_e + \mu \operatorname{dev} \bar{\mathbf{b}}_e$$

  2. Yield function:

     $$f(\boldsymbol{\tau}, \theta, \alpha) = \sqrt{\frac{3}{2}} || \operatorname{dev} \boldsymbol{\tau} || - [\sigma_{Y0}(\theta) - \hat{q}(\theta)] \leq 0$$

  3. Plastic flow rule:

     $$\mathbf{d}_p = \dot{\gamma} \, \frac{\partial f}{\partial \boldsymbol{\tau}}$$

  4. If $\theta \in [0.5 \, T_m, \, T_m]$: Evolution of plastic strain for visco-plasticity

     $$\langle \dot{\gamma} \rangle = \frac{1}{\eta_p} f(\boldsymbol{\tau}, \alpha, \theta)$$

     If $(\theta < 0.5 \, T_m)$: Loading/ unloading conditions for elasto-plasticity

     $$f \leq 0, \qquad \dot{\gamma} \geq 0, \qquad \dot{\gamma} f(\boldsymbol{\tau}, \alpha, \theta) = 0$$

  5. Evolution of accumulated plastic strain

     $$\dot{\alpha} = \dot{\gamma}$$

Figure 4.4. Constitutive equations varying with temperature. Heat capacity, elastic stress, entropy and plastic hardening stress are derived from the free energy functional (4.14).

exceeded, that is the Kuhn-Tucker conditions (4.32) do not hold. Therefore, an additional constitutive equation is required that governs the amount of plastic flow. In the present work, the classical Bingham model is used:

$$\langle \dot{\gamma} \rangle = \frac{1}{\eta_p} f\left(\boldsymbol{\tau}, \alpha, \theta\right) \tag{4.33}$$

The Macaulay bracket $\langle \dot{\gamma} \rangle$ ensures that the expression on the right hand side only holds if it is greater or equal to zero. If $f\left(\boldsymbol{\tau}, \alpha, \theta\right)$ is less than zero, the stresses lay within the elastic domain and no plastic flow occurs.
Note that the viscous flow rule may be further adapted within the temperature range from $\theta \in [0.5,\, 0.8]\, T_{melt}$ and $\theta \in [0.8,\, 1.0]\, T_{melt}$ to model specific material behavior, see e.g. GOLDAK & AKHLAGHI (2005) for details. An overview of visco-plastic flow rules can be found in DE SOUZA NETO ET AL. (2008). To illustrate the capability of the numerical framework to display the most important effects of melting and consolidation, the Bingham model is deemed sufficient. The constitutive equations are summarized in figure 4.4.

4.2.3 Dissipation

After having defined the constitutive equations for stress and entropy, additional assumptions are made on the dissipation D_{int} (4.17). In the liquid phase, heating due to viscous dissipation is neglected since melt is nearly inviscid. In the solid phase, the dissipation D_{int} is derived from (4.17) by implementing the definition of Cauchy stress (4.21). Making use of the relation $\mathscr{L}_v \mathbf{b}_{rev} = -2\mathbf{d}_p \mathbf{b}_{rev}$ derived from $\overline{\dot{\mathbf{C}}_p^{-1}}$ (4.28) and the flow rule for $\mathbf{d}_p$ (4.30) as well as of the evolution of plastic hardening (4.31), the resulting dissipation becomes:

$$D_{int} = -\frac{1}{2}\boldsymbol{\sigma}\, \mathbf{b}_{rev}^{-1} : \left(\mathscr{L}_v \mathbf{b}_{rev}\right) - \rho \frac{\partial \psi}{\partial \alpha}\dot{\alpha} = \boldsymbol{\sigma} : \mathbf{d}_p + \hat{q}\dot{\alpha} = \left(\sqrt{\frac{3}{2}} || \operatorname{dev} \boldsymbol{\sigma} || + \hat{q}\right)\dot{\gamma} \tag{4.34}$$

In order to fit experimental observations, SIMO & MIEHE (1992) suggest that only a fraction $\chi \in [0, 1]$ of plastic dissipation is converted into heat. This yields to the redefinition of dissipation:

$$D_{int} = \chi \left(\sqrt{\frac{3}{2}} || \operatorname{dev} \boldsymbol{\sigma} || + \hat{q}\right)\dot{\gamma} \tag{4.35}$$

In the presence of laser irradiation, the plastic heating is assumed to only play a minor role in the overall energy balance and χ is set to zero.

4.3 Boundary Conditions

The evolution of deformation and temperature is described by the momentum and the energy equation which have been derived in chapter 3. The physical phenomena relevant to the SLM process are implemented into these equations as graphically illustrated in figure 4.5. The effects are accounted for either via constitutive relations or boundary conditions. The phase transition is represented by modifying the heat capacity (section 4.2) and the fading

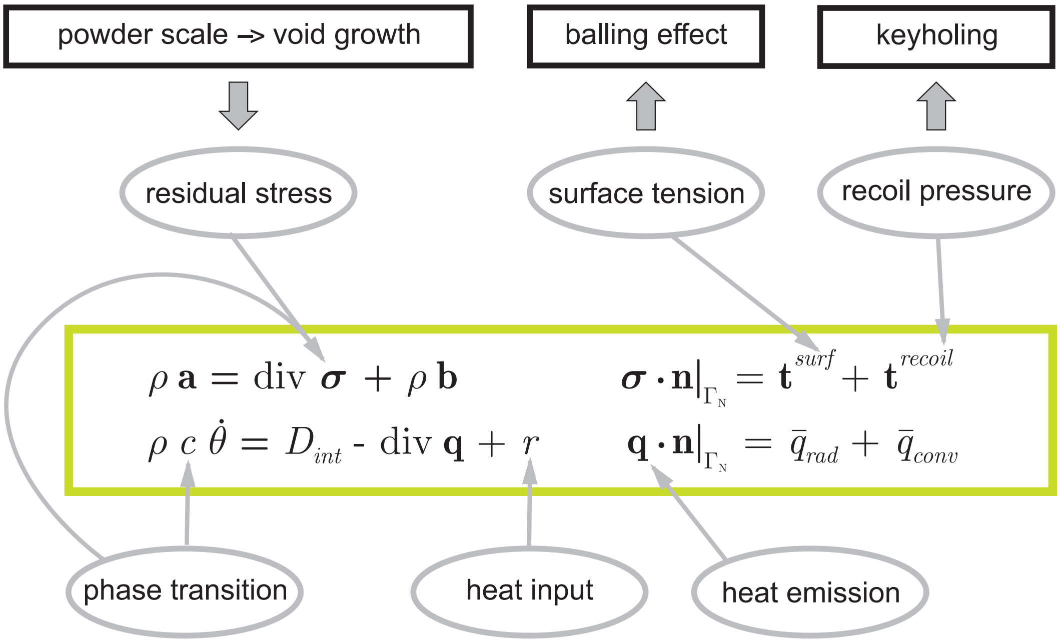
powder scale -> void growth
balling effect
keyholing
residual stress
surface tension
recoil pressure
$\rho\,\mathbf{a} = \operatorname{div}\boldsymbol{\sigma} + \rho\,\mathbf{b}$
$\boldsymbol{\sigma}\cdot\mathbf{n}|_{\Gamma_N} = \mathbf{t}^{surf} + \mathbf{t}^{recoil}$
$\rho\,c\,\dot{\theta} = D_{int}$ - $\operatorname{div}\mathbf{q} + r$
$\mathbf{q}\cdot\mathbf{n}|_{\Gamma_N} = \bar{q}_{rad} + \bar{q}_{conv}$
phase transition
heat input
heat emission

Figure 4.5. Representation of physical effects in the momentum and energy equation via constitutive equations and Neumann boundary conditions.

memory of the isochoric deformation gradient (section 4.1). Macroscopic residual stresses are described with an elasto-(visco)-plastic stress model discussed in the previous section. The local form of the momentum equation (3.18) writes with $\boldsymbol{\sigma}(\phi)$ the phase dependent Cauchy stress tensor (4.21) and Neumann boundary conditions on the liquid free surface Γ_N:

$$\rho\,\mathbf{a} = \operatorname{div}\boldsymbol{\sigma}(\phi) + \rho\,\hat{\mathbf{b}} \qquad \boldsymbol{\sigma}(\phi = 0)\cdot\mathbf{n}|_{\Gamma_N} = \mathbf{t}^{surf} + \mathbf{t}^{rec} \tag{4.36}$$

The surface tractions $\mathbf{t}^{surf}$ and $\mathbf{t}^{rec}$ caused by surface tension and recoil pressure will be discussed in sections 4.3.1 and 4.3.2.

In the energy equation, the incident laser power P can be distributed into the irradiated component by means of a volumetric intensity function $I(r, z)$. Details on the modeling of laser irradiation will be discussed in chapter 5. Assuming Fourier type heat conduction $\mathbf{q} = -k \operatorname{grad}\theta$ with isotropic thermal conductivity k and implementing the entropy work (4.20), the energy equation (3.31) becomes:

$$\rho\,(c + c_{L_\theta})\,\dot{\theta} = k \operatorname{div}(\operatorname{grad}\theta) + P\,I(r, z) \qquad \mathbf{q}\cdot\mathbf{n}|_{\Gamma_N} = \bar{q}_{rad} + \bar{q}_{conv} \tag{4.37}$$

Convective and radiative fluxes $\mathbf{q}_{conv}$ and $\mathbf{q}_{rad}$ can be imposed onto the energy equation as Robin boundary conditions $\bar{q}_i = \mathbf{q}_i \cdot \mathbf{n}$ with $\mathbf{n}$ being the surface normal. They can be expressed by Newton's law of cooling and the Stefan-Boltzmann law:

$$\bar{q}_{conv} = -\alpha_{conv}\cdot(\theta - \theta_{0\,conv}) \qquad \bar{q}_{rad} = -\sigma\,\epsilon\,\left(\theta^4 - \theta_{0\,rad}^4\right) \tag{4.38}$$

Here, α_{conv} denotes the convection coefficient, σ the Stefan Boltzmann constant, ϵ the emissivity and $\theta_{0\,i}$ reference temperatures. Since GANERIWALA & ZOHDI (2016) analyzed that thermal conduction outnumbers convection and radiation by several orders of magnitude, these boundary fluxes have been neglected in the current analysis.

4.3.1 Surface Tension and Marangoni Convection

The difference between cohesive forces of liquid metal and surrounding inert gas results in a surface tension $\mathbf{t}^{surf}$. The stress boundary condition at an interface between two media is of Neumann type and follows from a generalization of Laplace's formula:

$$(\boldsymbol{\sigma}_1 - \boldsymbol{\sigma}_2)\,\mathbf{n} = \gamma\,\kappa\,\mathbf{n} + \operatorname{grad}_{\partial a}\gamma \tag{4.39}$$

A derivation of the above statement can be found in LANDAU & LIFŠIC (1987). Here, κ denotes the curvature of the interface between the melt and surrounding inert gas. The surface tension coefficient γ is in general a function of temperature which yields the aforementioned Marangoni effect.

In SLM, the density and viscosity of the surrounding gas phase are much lower compared to the processed metal. Therefore, its influence can be neglected in the model. The surface traction $\mathbf{t}^{surf}$ caused by surface tension acting on liquid metal writes:

$$\mathbf{t}^{surf} = -\gamma\,\kappa\,\mathbf{n} - \operatorname{grad}_{\partial a}\gamma \tag{4.40}$$

The tangential gradient operator $\operatorname{grad}_{\partial a}$ can be obtained by subtracting the gradient in normal direction from the global operator (BRACKBILL ET AL., 1992):

$$\operatorname{grad}_{\partial a}\gamma = \operatorname{grad}\gamma - \mathbf{n}\;(\mathbf{n}\cdot\operatorname{grad}\gamma) \tag{4.41}$$

The curvature computes from the divergence of the normal in tangential direction. Since the divergence of the normal in normal direction is per definition equal to zero, it is assumed that the curvature can also be computed from the global derivative (BRACKBILL ET AL., 1992):

$$\kappa = \operatorname{div}\mathbf{n} \tag{4.42}$$

Note that due to numerical discretization errors, the divergence in normal direction might become non-zero. If this is the case, it is more suitable to compute the derivative as the arithmetic mean of the two principal curvatures (9.4). This methodology will be addressed in chapter 9.

4.3.2 Recoil Pressure

As has been illustrated in figure 2.2, escaping vaporized metal indents the melt pool. To avoid the simulation of the gas phase, its interaction with liquid metal can be represented by a recoil pressure. In the continuum framework, the recoil pressure is an external, mechanical, purely volumetric load. It can be computed from a relation found by ANISIMOV & KHOKHLOV (1995) used e.g. in the work of KHAIRALLAH ET AL. (2016). The recoil pressure can be incorporated as a Neumann boundary condition:

$$\mathbf{t}^{rec} = -p^{rec}(\theta)\,\mathbf{n} \quad \text{with} \quad p^{rec}(\theta) = 0.54\,p_a \exp\left(\frac{\lambda}{k_b}\left(\frac{1}{T_v} - \frac{1}{\theta}\right)\right) \tag{4.43}$$

Here, p_a is the ambient pressure, λ the evaporation energy per atom, k_b the Boltzmann constant and T_v the vaporization temperature. Note that the recoil pressure expands the liquid-vapor interface while surface tension tends to minimize it.

Beside the melt pool indentation, vaporization also has the effect of cooling the melt pool. KHAIRALLAH ET AL. (2016) account for this cooling via a vaporization heat flux which is expressed in terms of the recoil pressure. Both recoil pressure and vaporization heat flux are neglected in this work.

Chapter 5

Heat Source Modeling

Lasers can emit power in pulses and in special cases continuously (HECHT, 2011). Both types will be considered in this work[1]. A rectangular laser pulse is defined by the pulse width Δt_{pulse}, the repetition rate f_{rep} and the pulsing power P_{pulse}. The effective laser power P_{laser} is obtained from:

$$P_{laser} = f_{rep}\, \Delta t_{pulse}\, P_{pulse} \tag{5.1}$$

In a pulsed laser, the emitted power P is a function of time t. As graphically illustrated in figure 5.1, a sequence of n_{pulse} rectangular pulses can be expressed by a series of Heaviside functions:

$$P\left(t\right) = P_{pulse} \sum_{n=0}^{n_{pulse}} \left[H_n \left(t - \frac{n}{f_{rep}} \right) - H_n \left(t - \frac{n}{f_{rep}} - \Delta t_{pulse} \right) \right] \tag{5.2}$$

The spatial dependency of the emission of laser energy is expressed by an intensity function. It distributes the power $P\left(t\right)$ within an area $\mathrm{d}a$. For a circular focused beam, the intensity distribution $I_{rad}\left(r\right)$ is radially symmetric:

$$\frac{P\left(t,r\right)}{\mathrm{d}a} = P\left(t\right)\, I_{rad}\left(r\right) \quad \text{with} \quad \int_0^\infty I_{rad}\left(r\right)\, \mathrm{d}a = 1 \tag{5.3}$$

Here, the variable r is the radial distance from the laser's focal midpoint. Note that the focal midpoint of the laser is moving with the laser velocity v_{laser}. Oftentimes, a Gaussian distribution is assumed where the standard deviation is half the laser beam radius R:

$$I_{rad}\left(r\right) = \frac{2}{\pi R^2} e^{-2r^2/R^2} \tag{5.4}$$

The beam radius R can be defined as the radius where the intensity reduces to $1/e^2$ of the peak intensity. This corresponds to 86.47% of the laser power that is focused inside the circular laser spot. In this work, the Gaussian distribution is normalized in order to distribute the entire laser power within the spot:

$$I_{rad}\left(r\right) = \frac{2}{\pi R^2 \left(1 - e^{-2}\right)} e^{-2r^2/R^2} \tag{5.5}$$

---

[1] The findings of the this chapter have been published previously in WESSELS ET AL. (2019).

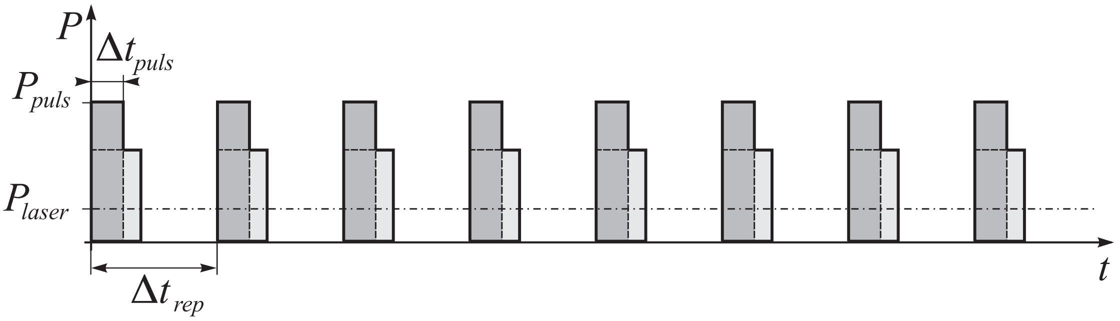

Figure 5.1. Sequence of rectangular laser pulses. Illustration of pulsing width Δt_{puls}, repetition rate $f_{rep} = 1/\Delta t_{rep}$, pulsing power P_{puls} and effective laser power P_{laser}.

An introduction into laser technology and an overview of related intensity distributions for various laser applications can be found for instance in HECHT (2011).

ZOHDI (2014) names four stages of sophistication to model the laser input: First, neglecting thermal conduction, the heating $\Delta\theta$ can be estimated from the energy absorbed by the powder bed. This assumption is clearly not accurate enough on the powder scale of SLM processes. However, in part scale simulations, the superposition of heat kernel solutions can be employed as a computationally efficient heat source (ZOHDI, 2017a, 2019). The next step of sophistication is to assume a volumetric intensity distribution. Even more precise is ray tracing, where the beam is discretized into energy portions, so-called rays. The last step of sophistication is to represent the beam by its electro-magnetic field components via Maxwell equations. While the Maxwell equations provide a high level of accuracy (ZOHDI, 2010), their solution comes at a high computational cost and is not feasible within a powder scale SLM simulation. Oftentimes, volumetric heat sources are employed because of their ease of implementation. Their formulation is usually motivated from empirical observations. A critical limitation is that the absorption highly depends on the overlap of the volumetric intensity distribution with the irradiated geometry. As illustrated in figure 5.2, this is a severe concern in powder scale SLM simulations. For an accurate description of absorption and reflection, ray tracing is most appropriate. Ray tracing is a purely geometrical approach and applicable if diffraction is not expected to occur. In SLM, this is fulfilled since the diameter of powder particles and the characteristic surface features are more than a magnitude larger than the wavelength of the incident radiation (ZOHDI, 2013).

In this work, both ray tracing and volumetric heat sources are considered. The impact of heat source modeling for the simulation of metal powder fusion will be assessed by means of numerical examples in chapters 7 and 8. In the outline of this section, the theoretical foundations of the ray tracing approach and volumetric heat source models are discussed.

5.1 Ray Tracing

Ray tracing is commonly used in optics, see e.g. GROSS (2005), ZOHDI (2006b) and ZOHDI & KUYPERS (2006). The scattering of incident radiation in particulate media has been investigated in ZOHDI (2006a), ZOHDI (2015a), and ZOHDI (2017b), for instance. Also in

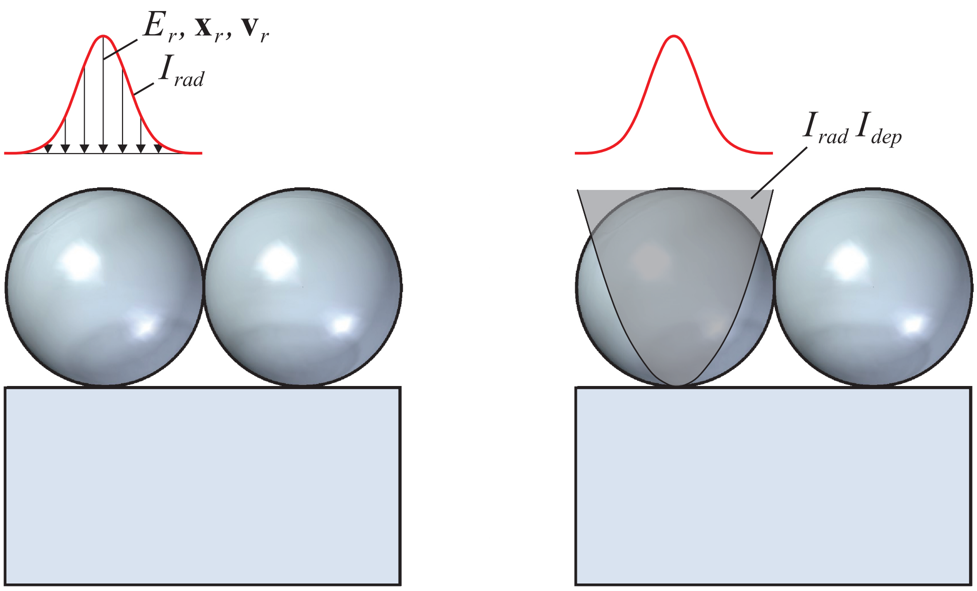

(a) Discretization of laser power into rays (b) Volumetric heat source

Figure 5.2. Heat source modeling. Left: Using ray tracing, the laser is divided into discrete energy portions (rays) that are absorbed by the irradiated part. Right: With a volumetric heat source model, most of the laser power is distributed into the grey shaded volume. Therefore, energy is lost in the gaps between powder particles.

metal processing simulations ray tracing is a useful numerical tool. ZOHDI (2013) developed a ray tracing algorithm for the Discrete Element Method (DEM) to investigate the laser-matter interaction of irradiated powdered material. KI ET AL. (2002) established a detailed model for laser keyhole welding for solution with the mesh-based Finite Difference Method. Therein, the evolution of the liquid-vapor interface is tracked with a level set method. At the same time, the level sets provide the surface normals for the coupling with a ray tracing algorithm. HU & EBERHARD (2016) used ray tracing to determine the absorptivity of metal during conduction mode laser welding. The absorptivity of solid and liquid metal is then fed into a Smoothed Particle Hydrodynamics (SPH) simulation, where a volumetric heat source is employed. In subsequent work, HU ET AL. (2016) have developed a coupling algorithm for ray tracing and SPH. To compute the reflection, a triangulation of the free surface was conducted. The triangulation is a computationally very expensive operation. Recently, WESSELS ET AL. (2019) have developed a coupling algorithm for ray tracing and meshfree solution schemes that overcomes the necessity of a surface triangulation. This algorithm will be presented in chapter 7.

The theory of ray tracing can be motivated from Maxwell's equations, see e.g. ZOHDI (2013). Ray tracing can also be regarded as a spatial and temporal discretization of a heat source into discrete energy portions (rays). A planar wavefront is represented by collinear rays that are emitted at specified time steps. Initially, the rays are placed at random positions inside the laser spot. This is sketched in figure 5.2(a). The amount of energy E_r assigned to a ray depends on its position $\mathbf{x}_r$ within the beam:

$$E_r = \Delta t_r \, P(t) \; w_r(r_r) \tag{5.6}$$

The time increment of ray creation is denoted Δt_r. The weight w_r is a function of the radial distance r_r of a ray to the laser's focal midpoint. It is obtained by normalization of the radial intensity distribution:

$$w_r = \frac{I_{rad}(r_r)}{\sum_q^{n_{rpl}} I_{rad}(r_q)} \tag{5.7}$$

Here, n_{rpl} is the number of rays per level, i.e. the number of rays that are created within a time step Δt_r. In this work, a Gaussian beam is used with I_{rad} as defined in (5.5). The rays propagate in time at constant velocity $\mathbf{v}_r$. The actual ray velocity depends on the permittivity and permeability in free space as well as on the medium the rays are traversing. It is in the order of the speed of light in Argon gas, i.e. $\approx 3 \cdot 10^8$ m/s. To resolve the conflict of scales between the thermal problem and the ray propagation, the ray velocity is scaled by a factor k^{red}. The ray positions $\mathbf{x}_r$ are updated in each time step Δt of the discrete thermal problem:

$$\mathbf{x}_{r\,n+1} = \mathbf{x}_{r\,n} + k^{red} \, \mathbf{v}_r \, \Delta t \tag{5.8}$$

The scaling factor k^{red} as well as the coupling between ray tracing algorithm and OTM are topic of chapter 7.

5.2 Volumetric Heat Sources

The idea of volumetric heating terms is to distribute the incident power into a specified volume. It is most appropriate if the heat source can disperse into the irradiated system. The shape of the function that describes the irradiated volume is based on theoretical considerations or empirical observations. Many formulations of volumetric heating terms have been developed for various applications. GOLDAK ET AL. (1984) suggested a double ellipsoidal model which is widely used by the welding community. The idea is to distribute the absorbed energy into the weld pool, whose geometry has to be estimated from experiments. YAN ET AL. (2015) use a Monte Carlo method to model electron penetration into a metal powder bed. The outcome is a physically informed volumetric heat source for the Electron Beam Melting (EBM) process, see YAN ET AL. (2017). Based on an analytical solution of the radiation transfer equation, GUSAROV ET AL. (2009) established a volumetric heat source for the SLM process which accounts for the multiple reflections inside the powder bed. GANERIWALA & ZOHDI (2016) use a volumetric heat source based on a Beer-Lambert equation to model the powder bed irradiation.

Generally, a volumetric intensity distribution consists of a radial component I_{rad} and a contribution I_{dep} that describes the penetration of the laser into the part:

$$\frac{P(t,r,z)}{\mathrm{d}v} = P(t) \; I_{rad}(r) \; I_{dep}(z) \quad \text{with} \quad \int_0^L \int_0^\infty I_{rad}(r) \; I_{dep}(z) \; \mathrm{d}a \, \mathrm{d}z = 1 \tag{5.9}$$

Here, L is the maximum penetration depth of the heat source. The concept is graphically illustrated in figure 5.2(b). The Gusarov-type heat source and the Beer-Lambert law are summarized next.

Gusarov type heat source

GUSAROV ET AL. (2009) assume a bell-like radial intensity function:

$$I_{rad}\left(r\right) = \frac{3}{\pi R^2}\left(1 - \frac{r}{R}\right)^2\left(1 + \frac{r}{R}\right)^2 \tag{5.10}$$

The dependence of the intensity on the powder bed penetration depth z is modeled as:

$$I_{dep}\left(z\right) = -\beta\,\frac{\mathrm{d}q}{\mathrm{d}\xi\left(z\right)} \quad \text{with} \quad \beta = \frac{3(1-\varepsilon_b)}{2\,\varepsilon_b\,D} = \frac{\lambda}{L} \tag{5.11}$$

Here, q denotes the dimensionless laser energy density and $\xi\left(z\right) = \beta\,z$ a dimensionless coordinate. The differentiation of q with respect to $\xi\left(z\right)$ can be found in appendix C.1. The optical extinction coefficient β takes into account the powder bed porosity ε_b and the particle diameter D. It can also be obtained from the optical thickness λ and the powder bed depth L, see GUSAROV ET AL. (2009) for details. Note that the absorptivity is highly phase and temperature dependent. In a volumetric heat source model, this effect could be incorporated by implementing a temperature dependent optical extinction coefficient $\beta\left(\theta\right)$. However, reliable experimental data is hard to obtain. Therefore, usually the temperature independent approximation of β $(5.11)_2$ is employed.

Beer-Lambert law

The Beer-Lambert law assumes an exponential decrease of absorptivity with penetration depth:

$$I_{dep}\left(z\right) = I_{0z}\,e^{-\int_0^z \beta(z)\,\mathrm{d}z} \tag{5.12}$$

For a porous metal powder bed, the extinction coefficient β can be taken as a constant value as defined in $(5.11)_2$. The coefficient I_{0z} is obtained from normalization of the intensity function over the powder bed depth L. The normalized Beer-Lambert law for the powder bed yields:

$$I_{dep}\left(z\right) = \beta\left(1 - e^{-\beta L}\right)^{-1}\,e^{-\beta z} \tag{5.13}$$

Due to the normalization, losses with respect to penetration depth are not accounted for in this formulation.

Chapter 6

Optimal Transportation Meshfree Algorithm

The OTM is an Updated Lagrangian method that has initially been introduced by LI ET AL. (2010). In the original version, in every time step a nodal rearrangement based on r-adaptivity is necessary to equilibrate the configurational forces. Recently, WEISSENFELS & WRIGGERS (2018) have developed a stabilized OTM approach. Since in this version no additional shifting algorithm is necessary, it is preferred in the present work.

The OTM belongs to the class of meshfree Galerkin methods. Primary variables and their time derivatives are nodal quantities, whereby mass, volume, density, stress and heat conduction are defined at material points. During the computation, a search algorithm establishes the connectivity between material points and nodes. The nodes connected to a material point form its support domain whose shape is in general arbitrary. This is why flexible shape functions are required that depend on the nodal positions only. LI ET AL. (2010) suggest the use of Local Maximum Entropy (LME) shape functions introduced by ARROYO & ORTIZ (2006) within the OTM framework.

Oftentimes, meshfree methods make use of explicit time integration in combination with

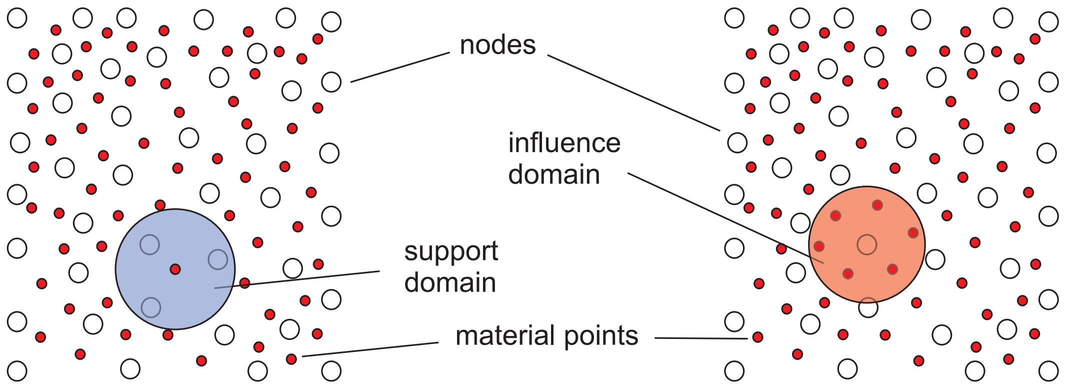

Figure 6.1. Spatial discretization into nodes and material points with the Optimal Transportation Meshfree method. The neighboorhood of a material point is referred to as support domain while the neighboorhood of a node is called influence domain.

lumping techniques because it facilitates the implementation of parallelization concepts, see e.g. LI ET AL. (2014). However, for SLM simulations the Courant-Friedrichs-Lewy (CFL) condition is very restrictive within explicit schemes. The small geometry in SLM powder scale simulations in combination with high Young's moduli of metal push the required time step size in the order of $\mathcal{O}\,(10^{-14}\,\text{s})$. KHAIRALLAH & ANDERSON (2014) face this issue by artificially raising densities. YAN ET AL. (2017) have modeled the solid and the liquid phase as an incompressible fluid with phase dependent viscosity to increase the admissible time step. Recently, WESSELS ET AL. (2018) have developed a phase change model with an elastic solid phase in combination with an implicit solution scheme in order to circumvent the CFL condition. This enables the use of time steps in the range of $\mathcal{O}\,(10^{-6}\,\text{s})$. As a new contribution, the concept is extended in this work about an elasto-visco-plastic material model in the solid phase. Beside the implicit thermo-mechanical OTM, also an explicit thermal version is described within this chapter. It is used in order to establish a coupling algorithm between OTM and a ray tracer as suggested in WESSELS ET AL. (2019).
The outline of this chapter is as follows: First, the explicit thermal scheme is described in section 6.1. The implicit thermo-mechanical scheme including the update of kinematic quantities, a local return mapping algorithm and a stabilization of the momentum equation is topic of section 6.2. Search algorithm and LME shape functions are introduced in sections 6.3 and 6.4. All iterative solution algorithms for the different non-linear equations in this work have been generated with the software *AceGen*. The concept is briefly discussed in section 6.5. A penalty contact formulation is presented in section 6.6.

6.1 Explicit Solution of the Energy Equation with OTM

WEISSENFELS & WRIGGERS (2018) have shown that the OTM can be derived from the principle of virtual work. Hence, the weak form of the energy equation is obtained by multiplying the strong form (4.37) with a trial function $\delta\theta$. After partially integrating and neglecting surface boundary heat fluxes it can be expressed as:

$$\int_v \delta\theta\,\rho\,(c + c_{L_\theta})\,\dot{\theta}\ \mathrm{d}v + \int_v k\ \operatorname{grad}\delta\theta\ \operatorname{grad}\theta\ \mathrm{d}v - \int_v \delta\theta\,P\,I\,(r,z)\ \ \mathrm{d}v = 0 \tag{6.1}$$

Following the standard Bubnov-Galerkin approximation, the same shape functions are employed to interpolate the primary variable and the trial function. This leads to the spatially discretized heat equation:

$$\mathbf{C}\,\dot{\boldsymbol{\theta}}_n + \mathbf{K}\,\boldsymbol{\theta}_n - \mathbf{Q} = \mathbf{0} \tag{6.2}$$

The discrete equations are assembled within loops over all material points n_{mp} and their support domains of size $N_{p\,n}^{sup}$ at every time step n. The conductivity matrix $\mathbf{K}$ is defined by:

$$\mathbf{K} = \bigcup_{p=1}^{n_{mp}} \sum_{I=1}^{N_{p\,n}^{sup}} \sum_{J=1}^{N_{p\,n}^{sup}} \frac{N_I\,(\mathbf{x}_{p\,n})}{\partial\mathbf{x}_{p\,n}}\,\frac{N_J\,(\mathbf{x}_{p\,n})}{\partial\mathbf{x}_{p\,n}} k_{p\,n}\,v_{p\,n} \tag{6.3}$$

The heat capacity matrix $\mathbf{C}$ is written in the lumped formulation:

$$\mathbf{C} = \bigcup_{p=1}^{n_{mp}} \sum_{I=1}^{N_{p\,n}^{sup}} \sum_{J=1}^{N_{p\,n}^{sup}} N_I\,(\mathbf{x}_{p\,n})\,\delta_{IJ}\,m_p\ (c_{p\,n} + c_{L_\theta\,p\,n}) \tag{6.4}$$

Here, δ_{IJ} denotes the Kronecker delta. The use of a lumped heat capacitance matrix is motivated from the observation of numerical temperature under- and overshoots in the presence of sharp thermal gradients. Chiumenti (1998) has illustrated that these become prominent when an open (Gauss) integration rule is used. Oscillations can be avoided when using a close (Lobatto) integration rule. A close integration rule means that the heat capacitance matrix is of non-negative type, i.e. the following conditions hold:

$$\begin{aligned} &\sum_{k=1}^{N} a_{ik} \geq 0 \quad \forall 1, ..., N \\ &a_{ik} \leq 0 \quad \text{if } i \neq k \end{aligned} \tag{6.5}$$

Details on the mathematical background can be found in Ciarlet & Raviart (1973) and Kikuchi (1977). Chiumenti (1998) remarks that the use of a lumped heat capacitance matrix is a possible alternative to enforce the requirement of a non-negative type matrix. This is the approach followed in the current work. The lumping concept is described in Hughes (2000).

The discretization of the heat input vector $\mathbf{Q}$ depends on the type of heat source model used. With P_{pn} the absorbed laser power at a material point, $\mathbf{Q}$ can be written in the general form:

$$\mathbf{Q} = \bigcup_{p=1}^{n_{mp}} \sum_{I=1}^{N_{pn}^{sup}} N_I \left(\mathbf{x}_{pn}\right) P_{pn} \tag{6.6}$$

The coupling of OTM and ray tracing will be discussed in chapter 7. When a volumetric heat source (5.9) is used, the power P_{pn} is a function of the radial distance r_{pn} and the penetration depth z_{pn}:

$$P_{pn} = P\left(t_n\right) \, I\left(r_{pn}, z_{pn}\right) \, v_{pn} \tag{6.7}$$

For a laser beam in direction of the x_3-coordinate, the radial and axial distances r_{pn} and z_{pn} of material points from the laser's focal midpoint $\mathbf{x}_{laser}\left(t\right)$ on the irradiated surface are calculated via:

$$r_{pn} = \left| \begin{pmatrix} \mathrm{x}_{laser\,1}\left(t\right) \\ \mathrm{x}_{laser\,2}\left(t\right) \end{pmatrix} - \begin{pmatrix} \mathrm{x}_{p1} \\ \mathrm{x}_{p2} \end{pmatrix} \right|_n \qquad z_{pn} = \left(\mathrm{x}_{p3}\right)_n \tag{6.8}$$

For the temporal discretization, the forward Euler scheme is employed. In combination with the lumped heat capacitance matrix, the nodal temperatures can be computed explicitly. At every node (except at Dirichlet boundaries) the temperature is updated from:

$$\theta_{I\,n+1} = \theta_{I\,n} + \sum_{p}^{N_{I\,n}^{inf}} \sum_{J}^{N_{pn}^{sup}} \frac{\Delta t}{m_{I\,n}\left(c_{pn} + c_{L_\theta\, pn}\right)} \left(-k_{pn}\, v_{pn}\, \frac{N_{Ipn}}{\partial \mathbf{x}_{pn}} \frac{N_{Jpn}}{\partial \mathbf{x}_{pn}} \theta_{J\,n} + N_{Ipn} P_{pn} \right) \tag{6.9}$$

Here, the abbreviation $N_I\left(\mathbf{x}_{pn}\right) = N_{Ipn}$ has been introduced. The nodal mass $m_{I\,n}$ is interpolated from the material point masses m_p inside the nodal influence domain of size $N_{I\,n}^{inf}$.

Regarding the choice of the time step increment within an explicit thermal scheme, Fried & Rheinboldt (2014) have shown that stability concerns override those of accuracy. They suggest the following criterion to ensure stability and convergence:

$$\Delta t \leq C \frac{\rho c}{k} h^2 \qquad 0 < C < 1 \tag{6.10}$$

Here, h is a typical length that can be chosen as the third root of averaged material point volume in three dimensional computations.

6.2 Implicit Thermo-Mechanical OTM

The strong forms of the momentum (4.36) and the energy equation (4.37) are multiplied by test functions $\boldsymbol{\eta}$ and $\delta\theta$, respectively. For simplicity, a process vector $\mathbf{p} = \{\mathbf{u}, \theta\}$ and a virtual process vector $\delta\mathbf{p} = \{\boldsymbol{\eta}, \delta\theta\}$ are introduced. After applying partial integration, the weak form can be stated as:

$$\begin{aligned} G\left(\mathbf{p}, \delta\mathbf{p}\right) = & \int_v \left[\rho\, \boldsymbol{\eta} \cdot \left(\mathbf{a} - \hat{\mathbf{b}}\right) + \operatorname{grad} \boldsymbol{\eta} : \boldsymbol{\sigma}(\phi)\right] \,\mathrm{d}v - \int_a \boldsymbol{\eta} \cdot \mathbf{t} \,\mathrm{d}a \\ & + \int_v \left[\delta\theta \left(\rho\left(c + c_{L_\theta}\right)\dot{\theta} - P\, I\left(r, z\right)\right) + k \ \operatorname{grad} \delta\theta \ \operatorname{grad} \theta\right] \,\mathrm{d}v = 0. \end{aligned} \tag{6.11}$$

As discussed in section 4.3, convective and radiative surface heat fluxes have been neglected in the energy equation. The direct imposition of surface tension as a surface traction $\mathbf{t}$ is cumbersome in meshfree methods. Due to the flexible connectivity, it is not known whether a particle lays at the free surface or not. Therefore, the Continuous Surface Force (CSF) model introduced by BRACKBILL ET AL. (1992) is employed. The CSF model is commonly applied in Smoothed Particle Hydrodynamics, see e.g. MORRIS (2000), FÜRSTENAU ET AL. (2019a) or FÜRSTENAU ET AL. (2019b). It has also been applied to the meshfree Material Point Method by CHEN ET AL. (2001). In the CSF model, an explicit tracking of the free surface is avoided by allowing the surface force to act within a small region of width $h = [\tilde{c}] / |\mathbf{c}|$ close to the free surface or interface. The model implies the definition of a color function $\tilde{c}$ and its gradient $\mathbf{c} = \operatorname{grad} \tilde{c}$. The color gradient is non-zero only in the proximity h of the free surface and points in direction of the outward normal. The quantity $[\tilde{c}]$ denotes the jump in color. Common choices for the color function are either the density (BRACKBILL ET AL., 1992), the mass (CHEN ET AL., 2001) or the volume (FÜRSTENAU ET AL., 2019a). Here, the mass is taken as color function. This choice of color will be critically analyzed in chapter 9.

With the definition of h and $\mathbf{c}$, the surface integrand $\mathrm{d}a$ is substituted by the volume integrand $\mathrm{d}v$ divided by the width h:

$$\int_a \boldsymbol{\eta} \cdot \mathbf{t}^{surf} \,\mathrm{d}a \approx - \int_v \boldsymbol{\eta}\, \gamma\, \kappa\, \mathbf{n} \frac{|\mathbf{c}|}{[\tilde{c}]} \,\mathrm{d}v = - \int_v \boldsymbol{\eta}\, \gamma\, \kappa \frac{\mathbf{c}}{[\tilde{c}]} \,\mathrm{d}v \tag{6.12}$$

The computation of a Marangoni force resulting from a temperature dependency of the surface tension coefficient γ will be addressed in section 9.1. Note that the recoil pressure from equation (4.43) could be incorporated in the same manner as a volumetric surface tension force but is neglected in the present analysis.

```
1) Compute color gradient
2) Loop over smoothing iterations
        Loop over nodes → Loop over $N_{I\,n}^{inf}$ → Loop over $N_{p\,n}^{sup}$
        { Smooth color gradient and nodal mass using (6.19) }
3) Compute nodal normal $\mathbf{n}_I$
4) Compute curvature $\kappa_p$
5) Loop over smoothing iterations
        Loop over material points → Loop over $N_{p\,n}^{sup}$ → Loop over $N_{I\,n}^{inf}$
        { Smooth curvature using (6.19) }
```

Figure 6.2. Surface tension computation with OTM.

The spatially discretized residual can be written in the form:

$$G\left(\mathbf{p}_{n+1}, \delta\mathbf{p}_{n+1}\right) = \mathbf{M}\,\mathbf{a}_{n+1} + \mathbf{R}_{\mathbf{u}}\left(\mathbf{u}_{n+1}\right) - \mathbf{P} + \mathbf{C}\,\dot{\boldsymbol{\theta}}_{n+1} + \mathbf{R}_{\boldsymbol{\theta}}\left(\boldsymbol{\theta}_{n+1}\right) - \mathbf{Q} = 0 \tag{6.13}$$

The assembly of the heat capacitance matrix $\mathbf{C}$ and the heat input vector $\mathbf{Q}$ at the current time step follow in analogy to the explicit scheme, see (6.4) and (6.6). A lumped mass matrix is employed which is defined by:

$$\mathbf{M} = \bigcup_{p=1}^{n_{mp}} \sum_{I=1}^{N_{p\,n}^{sup}} \sum_{J=1}^{N_{p\,n}^{sup}} N_I(\mathbf{x}_{p\,n})\,\delta_{IJ}\,m_p \tag{6.14}$$

The internal forces $\mathbf{R}_{\mathbf{u}}$ and the heat conduction $\mathbf{R}_\theta$ are formulated as a function of the unknown current values of the primary variables:

$$\begin{aligned} \mathbf{R}_{\mathbf{u}} &= \bigcup_{p=1}^{n_{mp}} \sum_{I=1}^{N_{p\,n}^{sup}} \sum_{J=1}^{N_{p\,n}^{sup}} \mathbf{B}_{IJ}^T\,\boldsymbol{\sigma}_{p\,n+1}\,v_{p\,n+1} \\ \mathbf{R}_\theta &= \bigcup_{p=1}^{n_{mp}} \sum_{I=1}^{N_{p\,n}^{sup}} \sum_{J=1}^{N_{p\,n}^{sup}} \frac{N_I\left(\mathbf{x}_{p\,n}\right)}{\partial\mathbf{x}_{p\,n+1}}\,\frac{N_J\left(\mathbf{x}_{p\,n}\right)}{\partial\mathbf{x}_{p\,n+1}}\,k_{p\,n}\,v_{p\,n+1}\,\theta_{J\,n+1} \end{aligned} \tag{6.15}$$

The $\mathbf{B}$-matrix involves the spatial shape function derivatives. A definition can be found in standard FEM textbooks, see for instance HUGHES (2000). Although the shape functions are constructed inside the support domains of the previous time step, their derivatives are computed with respect to the current material point coordinates $\mathbf{x}_{p\,n+1}$. This will be discussed later on in this section, see (6.22). The computation of the phase dependent stress tensor $\boldsymbol{\sigma}_{p\,n+1}$ in (6.15) follows the constitutive equations introduced in chapter 4. The local return mapping algorithm which accounts for the elasto-visco-plastic behavior in the solid phase is topic of sections 6.2.2 and 6.5.

The load vector $\mathbf{P}$ contains contributions from volumetric body forces $\hat{\mathbf{b}}$ and the volumetric surface tension force (6.12):

$$\mathbf{P} = \bigcup_{p=1}^{n_{mp}} \sum_{I=1}^{N_{pn}^{sup}} N_I\left(\mathbf{x}_{pn}\right) \left(\mathbf{f}_{pn}^{CSF} \frac{\left|\mathbf{c}_{pn}\right|}{\left[\tilde{c}_{pn}\right]} v_{pn} + m_p \hat{\mathbf{b}}_{pn} \right) \qquad \mathbf{f}_{pn}^{CSF} = -\gamma_{pn}\, \kappa_{pn}\, \mathbf{n}_{pn} \tag{6.16}$$

The curvature κ_p is evaluated at each material point from the divergence of the nodal normals inside the support domain, see also section 4.3.1. The nodal normal $\mathbf{n}_I$ is computed by normalization of a color gradient $\mathbf{c}_I$ which itself is defined as the nodal gradient of mass m_p:

$$\kappa_{pn} = \sum_{I=1}^{N_{pn}^{sup}} \frac{\partial N_I\left(\mathbf{x}_{pn}\right)}{\partial \mathbf{x}_{pn}} \cdot \mathbf{n}_{In} \qquad \mathbf{n}_{In} = \frac{\mathbf{c}_{In}}{\left|\mathbf{c}_{In}\right|} \qquad \mathbf{c}_{In} = \sum_{p}^{N_{In}^{inf}} \frac{\partial N_I\left(\mathbf{x}_{pn}\right)}{\partial \mathbf{x}_{pn}} m_p \tag{6.17}$$

The color gradient at the material point $\mathbf{c}_p$ is interpolated from the nodal values:

$$\mathbf{c}_{pn} = \sum_{I}^{N_{pn}^{sup}} N_I\left(\mathbf{x}_{pn}\right) \mathbf{c}_{In} \tag{6.18}$$

BRACKBILL ET AL. (1992) and CHEN ET AL. (2012) point out that constructing the color gradient from a smoothed color yields more accurate results. The implementation of the CSF model into OTM slightly differs from the original scheme: First, the nodal color gradient is computed. Next, the nodal mass and the color gradient are smoothed independently of each other. Additionally, the curvature κ_p is also smoothed. Smoothing is performed by averaging over the nodal or material point neighbors N_{In}^{nbr} or N_{pn}^{nbr}, respectively:

$$\tilde{m}_{In} = \frac{1}{N_{In}^{nbr}} \sum_{J}^{N_{In}^{nbr}} m_{Jn} \qquad \tilde{\mathbf{c}}_{In} = \frac{1}{N_{In}^{nbr}} \sum_{J}^{N_{In}^{nbr}} \mathbf{c}_{Jn} \qquad \tilde{\kappa}_{pn} = \frac{1}{N_{pn}^{nbr}} \sum_{q}^{N_{pn}^{nbr}} \kappa_{qn} \tag{6.19}$$

Further smoothing can be achieved by conducting subsequently more iterations of (6.19). Five iterations have been deemed sufficient in the calculations. Within the OTM framework, the neighbors can be identified via the influence and support domains of nodes and material points, respectively: Node I is considered a neighbor to node J if both are connected to at least one common material point. Accordingly, material points are considered to be neighbors if their support domains share a node. The algorithm is summarized in figure 6.2. In the implicit formulation, the weak form (6.13) is evaluated at the next time step t_{n+1}. Acceleration and velocity are integrated with an implicit Newmark and the temperature derivative with a backward Euler time integration scheme:

$$\begin{aligned}
\mathbf{a}_{n+1} &= \alpha_1\left(\mathbf{u}_{n+1} - \mathbf{u}_n\right) - \alpha_2 \mathbf{v}_n - \alpha_3 \mathbf{a}_n \\
\mathbf{v}_{n+1} &= \alpha_4\left(\mathbf{u}_{n+1} - \mathbf{u}_n\right) + \alpha_5 \mathbf{v}_n + \alpha_6 \mathbf{a}_n \\
\dot{\theta}_{n+1} &= \left(\Delta t\right)^{-1}\left(\theta_{n+1} - \theta_n\right)
\end{aligned} \tag{6.20}$$

The constants α_i are functions of the time step size $\triangle t$ and two parameters γ and β. Here, they have been chosen as $\gamma = 0.5$ and $\beta = 0.25$. Details on the Newmark time integration

```
1) Initialize
2) Loop over Newton iterations
        a) Assemble system of equations
        b) Solve
        c) Update primary variables and nodal coordinates
        d) Update kinematic quantities
        e) Check convergence
            If converged: exit loop
            Else: Update shape function derivatives and iterate again
3) Update support domains
4) Recompute shape functions
```

Figure 6.3. Algorithmic implementation of a time step in OTM.

and the admissible range for γ and β can be found in standard FEM textbooks, e.g. HUGHES (2000). Note that the backward Euler scheme is less accurate than the Newmark scheme. However, in the SLM process temperature and displacement are deemed equally important. Therefore, integrating also the temperature rate with a second order accurate method should be considered in future work.

The non-linear equations (6.13) are solved iteratively within a Newton-Raphson algorithm. For this purpose, the evolution of the residual G is expressed by a Taylor series of first order. Hence, the increment of the primary variables $\Delta\mathbf{p}_{n+1}^{k+1}$ is obtained from the solution of the following system of equations:

$$\left.\frac{\partial G\left(\mathbf{p}_{n+1}^{k}\right)}{\partial\mathbf{p}_{n+1}}\right|_{\mathbf{p}_{n+1}^{k}} \Delta\mathbf{p}_{n+1}^{k+1} = -G\left(\mathbf{p}_{n+1}^{k}\right) \tag{6.21}$$

Convergence is checked with the energy norm, see e.g. WRIGGERS (2008). The consistent linearizations of the contributions $\mathbf{R}_{\mathbf{u}}$ and $\mathbf{R}_{\theta}$ (6.15) to the global residual with respect to internal variables have been obtained with the software *AceGen* as discussed in section 6.5. The linearizations of the remaining terms are provided in the appendix B. The overall implicit stabilized OTM algorithm is sketched in figure 6.3.

As mentioned earlier, in an Updated Lagrangian scheme the previous time step t_n is chosen as the reference configuration. Consequently, the support domain and the shape functions are only updated after the Newton Raphson algorithm has converged. However, the spatial derivatives of the shape functions are updated within each iteration from:

$$\frac{\partial N_I\left(\mathbf{x}_{pn+1}^{k+1}\right)}{\partial\mathbf{x}_{pn+1}^{k+1}} \approx \frac{\partial N_I\left(\mathbf{x}_{pn}\right)}{\partial\mathbf{x}_{pn}}\frac{\partial\mathbf{x}_{pn}}{\partial\mathbf{x}_{pn+1}^{k+1}} = \frac{\partial N_I\left(\mathbf{x}_{pn}\right)}{\partial\mathbf{x}_{pn}}\left(\Delta\mathbf{F}_{pn+1}^{k+1}\right)^{-1} \tag{6.22}$$

Here, $\Delta\mathbf{F}_{pn+1}^{k+1}$ is the incremental deformation gradient. It is a kinematic quantity and as such discussed in the next section 6.2.1.

6.2.1 Update of Kinematic Quantities

The new positions of material point coordinates are interpolated from the updated positions of nodes inside the previous support domains using the shape functions of the previous time step:

$$\mathbf{x}_{p\,n+1}^{k+1} = \sum_{I=1}^{N_{p\,n}^{sup}} N_{I\,n}\left(\mathbf{x}_{p\,n}\right)\mathbf{x}_{I\,n+1}^{k+1} \tag{6.23}$$

An initial configuration is not stored to compute the deformation gradient. Alternatively, the deformation gradient is incrementally updated:

$$\mathbf{F}_{p\,n+1}^{k+1} = \frac{\partial \mathbf{x}_{p\,n+1}^{k+1}}{\partial \mathbf{X}} = \frac{\partial \mathbf{x}_{p\,n+1}^{k+1}}{\partial \mathbf{x}_{p\,n}}\frac{\partial \mathbf{x}_{p\,n}}{\partial \mathbf{X}} = \triangle\mathbf{F}_{p\,n+1}^{k+1}\mathbf{F}_{p\,n} \tag{6.24}$$

The incremental deformation gradient $\Delta\mathbf{F}_{p\,n+1}^{k+1}$ computes from the displacement increments:

$$\triangle\mathbf{F}_{p\,n+1}^{k+1} = \mathbf{1} + \sum_{I=1}^{N_{p\,n}^{sup}} \frac{\partial N_I\left(\mathbf{x}_{p\,n}\right)}{\partial \mathbf{x}_{p\,n+1}^{k}}\triangle\mathbf{u}_{I\,n+1}^{k+1} = \mathbf{1} + \sum_{I=1}^{N_{p\,n}^{sup}} \frac{\partial N_I\left(\mathbf{x}_{p\,n}\right)}{\partial \mathbf{x}_{p\,n}}\left(\Delta\mathbf{F}_{p\,n+1}^{k}\right)^{-1}\triangle\mathbf{u}_{I\,n+1}^{k+1} \tag{6.25}$$

Volume and density at each material point are updated accordingly, c.f. (3.8):

$$v_{p\,n+1}^{k+1} = \det\left(\triangle\mathbf{F}_{p\,n+1}^{k+1}\right)v_{p\,n} \qquad \rho_{p\,n+1}^{k+1} = \frac{m_p}{v_{p\,n+1}^{k+1}} \tag{6.26}$$

In the liquid phase, the material response depends on the rate of deformation rather than on its magnitude. The deviatoric stress in the liquid phase (4.24) is formulated as a function of the stretch tensor $\mathbf{d}$. It corresponds to the symmetric part of the spatial velocity gradient $\mathbf{l}$, c.f (3.12):

$$\mathbf{d}_{p\,n+1}^{k+1} = \mathrm{sym}\left(\mathbf{l}_{p\,n+1}^{k+1}\right) = \mathrm{sym}\left(\dot{\mathbf{F}}_{p\,n+1}^{k+1}\cdot\left(\mathbf{F}_{p\,n+1}^{k+1}\right)^{-1}\right) \tag{6.27}$$

The update of the rate of deformation is analogous to the update of the deformation gradient itself:

$$\dot{\mathbf{F}}_{p\,n+1}^{k+1} = \Delta\dot{\mathbf{F}}_{p\,n+1}^{k+1}\mathbf{F}_{p\,n} \tag{6.28}$$

The incremental rate of the deformation gradient is computed from the updated velocity:

$$\Delta\dot{\mathbf{F}}_{p\,n+1}^{k+1} = \frac{\partial \mathbf{v}_{p\,n+1}^{k+1}}{\partial \mathbf{x}_{p\,n}} = \sum_{I=1}^{N_{p\,n}^{sup}} \frac{\partial N_I\left(\mathbf{x}_{p\,n}\right)}{\partial \mathbf{x}_{p\,n}}\left(\Delta\mathbf{F}_{p\,n+1}^{k+1}\right)^{-1}\mathbf{v}_{I\,n+1}^{k+1} \tag{6.29}$$

6.2.2 Local Newton-Raphson Algorithm

In case of elasto-plasticity and elasto-visco-plasticity, the stresses must fulfill the additional constitutive requirements imposed by the yield criterion (4.25) and the flow rule (4.30) at each material point. In every iteration step of the global Newton-Raphson algorithm, first a trial state is computed based on the assumption that the deformation within the step is

Given: $\mathbf{C}_{p\,n}^{-1}, \gamma_n$ Find: $\mathbf{C}_{p\,n+1}^{-1}, \gamma_{n+1}$

$$\mathbf{b}_e = \mathbf{F}\,\mathbf{C}_p^{-1}\,\mathbf{F}^T$$

$$\boldsymbol{\tau} = K\,\ln J_e\,\mathbf{1} + \mu\,\mathrm{dev}\,\bar{\mathbf{b}}_e$$

$$f\left(\boldsymbol{\tau}, \theta, \alpha\right) = \sqrt{\frac{3}{2}}||\,\mathrm{dev}\,\boldsymbol{\tau}|| - \left[\sigma_{Y0}\left(\theta\right) - \hat{q}\left(\theta\right)\right] \leq 0$$

$$\mathbf{n} = \frac{\partial f}{\partial \boldsymbol{\tau}}$$

$$\dot{\alpha} = \dot{\gamma}$$

- Elasto-Plasticity $\theta < 0.5\,T_{melt}$:

$$\mathcal{Z} = \mathbf{b}_e - \exp\left(-2\,\left(\gamma_{k+1}^{j+1} - \gamma_k\right)\mathbf{n}\right)\mathbf{F}\,\mathbf{C}_{p\,n}^{-1}\,\mathbf{F}^T$$

$$\mathbf{h}_p = \left\{C_{p,11}^{-1}, C_{p,22}^{-1}, C_{p,22}^{-1}, C_{p,33}^{-1}, C_{p,12}^{-1}, C_{p,13}^{-1}, C_{p,23}^{-1}, \gamma\right\}$$

$$\mathbf{Q}_p = \left\{\mathcal{Z}_{11}, \mathcal{Z}_{22}, \mathcal{Z}_{33}, \mathcal{Z}_{12}, \mathcal{Z}_{13}, \mathcal{Z}_{23}, f\right\}$$

- Elasto-Visco-Plasticity $\theta \in [0.5, 1.0]\;T_{melt}$:

$$\langle\dot{\gamma}\rangle = \frac{1}{\eta_p} f\left(\boldsymbol{\tau}, \alpha, \theta\right) \geq 0$$

$$\mathcal{Z} = \mathbf{b}_e - \exp\left(-2\,\Delta t\,\dot{\gamma}\,\mathbf{n}\right)\mathbf{F}\,\mathbf{C}_{p\,n}^{-1}\,\mathbf{F}^T$$

$$g = \left(\gamma_{k+1}^{j+1} - \gamma_n\right) - \Delta t\,\dot{\gamma}_{n+1}$$

$$\mathbf{h}_p = \left\{C_{p,11}^{-1}, C_{p,22}^{-1}, C_{p,22}^{-1}, C_{p,33}^{-1}, C_{p,12}^{-1}, C_{p,13}^{-1}, C_{p,23}^{-1}, \gamma\right\}$$

$$\mathbf{Q}_p = \left\{\mathcal{Z}_{11}, \mathcal{Z}_{22}, \mathcal{Z}_{33}, \mathcal{Z}_{12}, \mathcal{Z}_{13}, \mathcal{Z}_{23}, g\right\}$$

Figure 6.4. Within the local Newton-Raphson algorithm, the internal variables $\mathbf{h}_p$ are iteratively updated such that the conditions imposed by the elasto-(visco)-plastic constitutive equations are fulfilled, i.e. such that the residual $\mathbf{Q}_p$ converges towards zero. This figure is adapted from Korelc & Stupkiewicz (2014).

purely elastic. Next, it is checked whether the trial state violates the yield criterion (4.25). If not, the actual state has been found and the computation is not different from the elastic one. However, if the yield criterion is violated, the internal variables need to be updated and the stress is returned in direction of the yield surface. This is done within a return-mapping algorithm, i.e. a local Newton-Raphson algorithm that is executed at each material point where the trial state violates the yield criterion (4.25). The concept is briefly described in this section. For details, the reader is referred to SIMO & HUGHES (1998) and KORELC & STUPKIEWICZ (2014).

Note that the evolution of the inverse plastic right Cauchy Green tensor $\mathbf{C}_p^{-1}$ from (4.28) is of a type which is conveniently integrated with the exponential map integrator: The equation $\dot{\mathbf{B}} = \mathbf{A}\,(t)\,\mathbf{B}$ has the solution $\mathbf{B} = \exp\left((t - t_0)\,\mathbf{A}\right)\mathbf{B}\,(t_0)$. Hence, the discrete evolution of $\mathbf{C}_p^{-1}$ can be implicitly integrated by:

$$\mathbf{C}_{p\,n+1}^{-1} = \exp\left(-2\,\Delta\gamma_{n+1}\,\mathbf{F}^{-1}\,\mathbf{n}\,\mathbf{F}\right)\mathbf{C}_{p\,n}^{-1} \tag{6.30}$$

Since $\mathbf{b}_e$ is a push-forward of $\mathbf{C}_p^{-1}$ and by making use of the identity $\exp\left(\mathbf{B}\,\mathbf{A}\,\mathbf{B}^{-1}\right) = \mathbf{B}\left(\exp\mathbf{A}\right)\mathbf{B}^{-1}$, (6.30) can also be expressed in terms of the elastic left Cauchy Green tensor $\mathbf{b}_e$:

$$\mathbf{b}_{e\,n+1} = \exp\left(-2\Delta\gamma_{n+1}\,\mathbf{n}\right)\mathbf{F}\,\mathbf{C}_{p\,n}^{-1}\,\mathbf{F}^T \tag{6.31}$$

In the return mapping algorithm, the vector of local unknowns $\mathbf{h}_p$ consists of the six entries of the symmetric inverse plastic left Cauchy Green tensor $\mathbf{C}_p^{-1}$ and the accumulated plastic strain $\alpha = \gamma$. The residual $\mathbf{Q}_p$ contains the six entries of the tensor $\mathcal{Z}$ which is obtained by rearranging (6.31) to zero. The seventh entry depends on the plasticity formulation. In elasto-plasticity, it consists of the yield function $f\left(\boldsymbol{\tau}, \alpha, \theta\right)$ which is enforced to be zero as part of the Kuhn-Tucker-conditions (4.32). The plastic increment $\Delta\gamma_{n+1} = \gamma_{k+1}^{j+1} - \gamma_k$ in (6.31) is the difference between the accumulated plastic strain γ_{k+1}^{j+1} at the current local iteration step $(j+1)$ and its value γ_k at the previous global step k.

Contrary, in visco-plasticity the Kuhn-Tucker conditions do not hold. The evolution of plastic strain is restricted to an additional constitutive equation for the plastic multiplier $\dot{\gamma}$ which in the present work is the Bingham model (4.33). As a consequence, the stress is projected in the direction of the yield surface, but not necessarily returned onto it as in the rate independent case. The amount of plastic flow is governed by (4.33) and f is allowed to be greater than zero. Backward Euler integration of the plastic multiplier yields:

$$\dot{\gamma}_{n+1}^{j+1} = \frac{\gamma_{n+1}^{j+1} - \gamma_n}{\Delta t} \quad \Leftrightarrow \quad \left(\gamma_{k+1}^{j+1} - \gamma_n\right) - \Delta t\,\dot{\gamma}_{n+1} = 0 \tag{6.32}$$

Inserting $\dot{\gamma}_{n+1}$ obtained from the Bingham model (4.33) into the above equation yields the seventh entry of the local residual $\mathbf{Q}_p$ in case of visco-plasticity.

The return mapping algorithm for both rate dependent and independent plasticity is summarized in figure 6.4. The consistent linearizion has been derived with the software *AceGen* which makes use of Automatic Differentiation (AD). The principle will be briefly introduced in section 6.5.

6.2.3 Stabilization of the Momentum Equation

WEISSENFELS & WRIGGERS (2018) have shown that the OTM suffers from insufficient integration. Motivated from similar observations of GANZENMÜLLER (2015) with the SPH method, they have suggested a stabilization term for the momentum equation. This stabilization is also employed in the current work. For this purpose, the distance vectors $\mathrm{d}\mathbf{x}_{I\,p\,n+1}$ between nodes and material points are computed in each support domain:

$$\mathrm{d}\mathbf{x}_{I\,p\,n+1} = \mathbf{x}_{I\,n+1} - \mathbf{x}_{p\,n+1} \tag{6.33}$$

The distance vector can also be obtained from the mapping of the distance vector $\mathrm{d}\mathbf{x}_{I\,p\,n}$ of the previous time step with the incremental deformation gradient. If the solution of the momentum equation was correct, the difference between the distance vector from (6.33) and the updated distance vector would be zero. As a consequence of reduced integration this is not always fulfilled. The discrepancy $\mathbf{e}^{k+1}_{p\,n+1}$ is defined by:

$$\mathbf{e}_{I\,p\,n+1} = \mathrm{d}\mathbf{x}_{I\,p\,n+1} - \Delta\mathbf{F}_{p\,n+1}\,\mathrm{d}\mathbf{x}_{I\,p\,n} \tag{6.34}$$

This error is enforced to be zero by applying the penalty method:

$$\mathbf{E} = \bigcup_{p=1}^{n_{mp}} \sum_{I=1}^{N^{sup}_{p\,n}} \varepsilon_s\, N_{I\,p\,n} \frac{\mathbf{e}_{I\,p\,n+1}}{||\mathrm{d}\mathbf{x}_{I\,p\,n}||} \tag{6.35}$$

The above defined tensor $\mathbf{E}$ acts as an additional force and is added to the discretized weak form of the equation of motion (6.13). The influence of the penalty parameter ε_s on the accuracy of the solution has been studied extensively by WEISSENFELS & WRIGGERS (2018) in various numerical examples. The consistent linearization of the penalty regularization $\mathbf{E}$ is provided in appendix B.

6.3 Search algorithm

The support domain of each material point is updated in every time step via a search algorithm. LIU ET AL. (1997) have formulated basic topological requirements for Galerkin meshfree methods. An algorithm with respect to these requirements has been introduced for the OTM by WEISSENFELS & WRIGGERS (2018). This algorithm is also used in the present work. The first step is to identify all nodes which lay within a radius r_p around a material point p:

$$\begin{aligned} S_{p\,n+1} &= \left\{ \mathbf{x}_{I\,n+1} \middle| ||\mathbf{x}_{I\,n+1} - \mathbf{x}_{p\,n+1}|| \leq \alpha^{ext}\, r_p \right\} \\ \text{with} \quad r_p &= \min\left(||\mathbf{x}_{I\,n+1} - \mathbf{x}_{p\,n+1}||\right) \quad \forall I \in S_{p\,n} \end{aligned} \tag{6.36}$$

Here, the radius r_p is obtained from the minimal distance of a node belonging to the old support domain $S_{p\,n}$. The search radius extension factor α^{ext} has been introduced to control the number of nodes inside the support domain. A particle distribution is regarded as admissible if all particles in each support domain $S := \bigcup_{p=1}^{n_{mp}} S_{p\,n+1}$ represent the whole body B_t

```
1) Determine radius of new support domain $\alpha^{ext} r_p$
2) Find nodes belonging to support domain (6.36)
3) If $N_p^{sup} \geq 4$ and $v_{p\,n+1}^{sup} > v_{p\,n+1}$
          Check all combinations until tetrahedron is found which encloses the material point
   Else
          Increase factor $\alpha^{ext} = c^{enla} \cdot \alpha^{ext}$ with $c^{enla} = const$ and go back to step 1)
```

Figure 6.5. Algorithmic implementation of the search algorithm.

without any spaces in between $B_t \subseteq S$. This requirement is met if the volume of a support domain $v_{p\,n+1}^{sup}$ is larger than the corresponding material point volume:

$$v_{p\,n+1}^{sup} > v_{p\,n+1} \tag{6.37}$$

In 3D computations, at least four nodes are necessary to form a convex hull around a material point. Additionally, in order to reduce the computational effort, the size of support domains should be kept as low as possible. The algorithm is summarized in figure 6.5.
Note that in the particle fusion analysis of chapter 8 particles fuse together. When fusing, the size of the free surface decreases. As a consequence, nodes may come to close to each other. Unnecessary nodes are deleted during the computation.

6.4 Local Maximum Entropy Shape Functions

Local Maximum Entropy (LME) shape functions have first been introduced by Arroyo & Ortiz (2006). They belong to the class of radial basis functions with an exponential ansatz:

$$Z_I\left(\mathbf{x}_p\right) = e^{-\beta_p ||\mathbf{x}_I - \mathbf{x}_p||^2 + \boldsymbol{\lambda}_p (\mathbf{x}_p - \mathbf{x}_I)} \qquad \beta_p = \frac{\gamma^{LME}}{h_p^2} \tag{6.38}$$

The parameter β_p determines the locality of the LME shape functions and ensures a smooth transition from meshfree approximants to Delaunay affine basis functions (Arroyo & Ortiz, 2006). It is the quotient of a constant $\gamma^{LME} > 0$ and the characteristic nodal spacing h_p which can be defined as twice the radius r_p of the support domain (6.36), see also Weissenfels & Wriggers (2018). Rosolen et al. (2009) have indicated $\beta_p = \left[0.8/h_p^2,\, 4/h_p^2\right]$ as an optimal interval for the locality parameter. The partition of unity is achieved by normalization, i.e. division by the sum Z of all functions Z_J inside the support domain:

$$N_I = \frac{Z_I\left(\mathbf{x}_p\right)}{Z}, \qquad Z = \sum_{J=1}^{N_p^{sup}} Z_J\left(\mathbf{x}_p\right) \tag{6.39}$$

The Lagrange multiplier $\boldsymbol{\lambda}_p$ has been introduced to meet the first order consistency criterion. It is restricted to the constraint:

$$\mathbf{r}\left(\mathbf{x}_p, \boldsymbol{\lambda}_p\right) = \sum_{I=1}^{N_p^{sup}} N_I\left(\mathbf{x}_p\right)\left[\mathbf{x}_p - \mathbf{x}_I\right] = 0 \tag{6.40}$$

The Lagrange multiplier $\boldsymbol{\lambda}_p$ is iteratively computed at each material point within a local Newton-Raphson algorithm using the software *AceGen* which will be discussed in the subsequent section. Note that the LME shape functions posses a weak Kronecker delta property. This means that it is only fulfilled on convex boundaries. For a mathematical explanation see Arroyo & Ortiz (2006) and for a graphical illustration in 2D Weissenfels & Wriggers (2018).

6.5 Automatic Code Generation

The computation of shape functions (6.40) as well as the solution of the global (6.21) and the local (figure 6.4) residuals are supported by the software *AceGen*. *AceGen* enables the fast generation of efficient numerical code at the Gauss point level, i.e. at the material point level in the context of OTM. The software combines automatic differentiation (AD) with symbolic description and automatic code generation as well as code optimization (Korelc & Stupkiewicz, 2014). Using AD, functions defined by a computer program can be differentiated (Korelc, 2009). An introduction to the topic can be found e.g. in Griewank (2008). The symbolic description comes into *AceGen* by a coupling with the software *Mathematica* (Mathematica 11.1, 2017). Code optimization strategies are discussed e.g. in Korelc (1997). For an in-depth discussion of automation of finite element methods, see Korelc & Wriggers (2016). Recently, *AceGen* has been applied to the Virtual Element Method (VEM), in which the number of nodes per element is arbitrary (Hudobivnik et al., 2018). This flexibility makes *AceGen* an efficient tool also for meshfree methods such as the OTM. As mentioned in the previous section, the computation of the LME shape functions requires the iterative solution of the Lagrange multiplier $\boldsymbol{\lambda}_p$ from the first order consistency condition (6.40) within a local Newton-Raphson algorithm at each material point. The derivation of the local tangent is conveniently obtained with *AceGen*:

$$\left.\frac{\partial \mathbf{r}}{\partial \boldsymbol{\lambda}}\right|_j \Delta \boldsymbol{\lambda}^{j+1} = -\mathbf{r}^j, \qquad \frac{\partial \mathbf{r}}{\partial \boldsymbol{\lambda}} = \frac{\hat{\delta} \mathbf{r}}{\hat{\delta} \boldsymbol{\lambda}} \tag{6.41}$$

The operator $\hat{\delta}$ denotes the computational derivative. It involves the aforementioned steps of automatic differentiation and expression optimization.

Next, the solution of the global Newton-Raphson algorithm (6.21) with *AceGen* for the unknown nodal displacements and temperatures is discussed. Transient terms as well as volumetric body forces, source terms and the stabilization (6.35) have been linearized analytically. Details are given in appendix B. Hence, in the momentum equation, only the internal forces while in the energy equation, only the heat conduction term (6.15) have been linearized with *AceGen*. Using the push-forward of the shape function derivatives (6.22), the discretized *AceGen* contribution $\mathbf{R}_{p\,ace}$ of a material point to the global residual writes:

$$\begin{aligned} \mathbf{R}^{k+1}_{p\,ace} = {} & \frac{N_I\left(\mathbf{x}_{pn}\right)}{\partial \mathbf{x}_{pn}} \left(\Delta \mathbf{F}^{k+1}_{pn+1}\right)^{-1} \cdot \boldsymbol{\sigma}^{k+1}_{pn+1}\, \Delta J^{k+1}_{pn+1}\, v_{pn} \\ & + \frac{N_I\left(\mathbf{x}_{pn}\right)}{\partial \mathbf{x}_{pn}} \left(\Delta \mathbf{F}^{k+1}_{pn+1}\right)^{-1} \frac{N_I\left(\mathbf{x}_{pn}\right)}{\partial \mathbf{x}_{pn}} \left(\Delta \mathbf{F}^{k+1}_{pn+1}\right)^{-1} \theta^{k+1}_{pn+1}\, \Delta J^{k+1}_{pn+1}\, v_{pn} \end{aligned} \tag{6.42}$$

Here, the current volume increment $v_{p\,n+1}^{k+1}$ has been expressed in terms of the volume increment of the previous time step $v_{p\,n}$ with the aid of the determinant of the incremental deformation gradient $\Delta J_{p\,n+1}^{k+1}$, c.f. (6.26). In the sense of an Updated Lagrangian formulation, the linearization of $v_{p\,n}$ is zero. As explained in section 6.2, the same applies to the linearizations $\Delta N_I\left(\mathbf{x}_{p\,n}\right)$ and $\Delta N_{I,\mathbf{x}_{p\,n}}\left(\mathbf{x}_{p\,n}\right)$. Therefore, the shape functions and their derivatives with respect to $\mathbf{x}_{p\,n}$ are fed into the *AceGen* routine as input variables. Within this routine, the deformation gradient, the Cauchy stress and the temperature at the material point are computed from the primary variables belonging to the nodes of the support domain, see sections 6.2.1 and 4.2. For elastic and visco-elastic materials, differentiation of (6.42) with respect to the vector $\mathbf{p}_p$ of nodal unknowns inside a support domain yields:

$$\frac{\partial \mathbf{R}_{p\,ace}^{k}}{\partial \mathbf{p}_p} = \frac{\hat{\delta} \mathbf{R}_{p\,ace}^{k}}{\hat{\delta} \mathbf{p}_p} \tag{6.43}$$

In case of elasto-(visco)-plasticity, the history variables are updated within a local return mapping algorithm at each material point, see section 6.2.2. This algorithm has again been generated with *AceGen*. The local tangent $\mathbf{A}_p^j$ is obtained by differentiating the local residual $\mathbf{Q}_p$ with respect to the internal variables $\mathbf{h}_p$. With $\mathbf{Q}_p$ and $\mathbf{h}_p$ from figure 6.4, the local Newton-Raphson algorithm writes:

$$\mathbf{A}_p^j\,\Delta \mathbf{h}_p^{j+1} = -\mathbf{Q}_p^j, \qquad \mathbf{A}_p^j = \left.\frac{\partial \mathbf{Q}_p}{\partial \mathbf{h}_p}\right|_j = \left.\frac{\hat{\delta} \mathbf{Q}_p}{\hat{\delta} \mathbf{h}_p}\right|_j \tag{6.44}$$

After the algorithm has converged, the global tangent is derived. Note that the local iteration procedure introduces an algorithmic dependency of the internal variables $\mathbf{h}_p$ on the deformation gradient $\mathbf{F}$, which in turn is a function of primary variables $\mathbf{p}_p$. This algorithmic dependency is not identical to the analytical one. Therefore, the correct dependency is specified for the automatic differentiation in terms of an AD exception. Using the product rule and the definition of the local tangent $\mathbf{A}_p$ (6.44), the contribution of a material point to the global tangent becomes, c.f. KORELC & STUPKIEWICZ (2014):

$$\mathbf{K}_{p\,ace} = \frac{\partial \mathbf{R}_{p\,ace}}{\partial \mathbf{p}_p} + \frac{\partial \mathbf{R}_{p\,ace}}{\partial \mathbf{h}_p}\frac{\partial \mathbf{h}_p}{\partial \mathbf{F}}\frac{\partial \mathbf{F}}{\partial \mathbf{p}_p} = \frac{\partial \mathbf{R}_{p\,ace}}{\partial \mathbf{p}_p} + \frac{\partial \mathbf{R}_{p\,ace}}{\partial \mathbf{h}_p}\left(-\mathbf{A}_p^{-1}\frac{\partial \mathbf{Q}_p}{\partial \mathbf{F}}\right)\frac{\partial \mathbf{F}}{\partial \mathbf{p}_p} \tag{6.45}$$

The computational derivative can now be written directly with the exception:

$$\mathbf{K}_{p\,ace} = \left.\frac{\hat{\delta} \mathbf{R}_{p\,ace}}{\hat{\delta} \mathbf{p}_p}\right|_{\frac{D\mathbf{h}_p}{D\mathbf{F}} = -\mathbf{A}_p^{-1}\frac{\partial \mathbf{Q}_p}{\partial \mathbf{F}}} \tag{6.46}$$

The local tangents $\mathbf{K}_p$ are assembled into the global tangent as discussed in standard textbooks, see e.g. DHATT & TOUZOT (1985).

6.6 Contact Formulation

In the numerical examples of chapter 8, rigid contact boundaries are imposed on the momentum and the energy equation. This is modeled via the penalty method which is briefly described here. An in-depth discussion of computational contact mechanics can be found in WRIGGERS (2006).

Displacement boundary

In the momentum equation, a penalty force $\mathbf{R}_{\mathbf{u}}^{con}$ is defined to model the contact with a rigid wall:

$$\mathbf{R}_{\mathbf{u}}^{con} = \bigcup_{p=1}^{n_{mp}} \sum_{I=1}^{N_{p\,n}^{sup}} \varepsilon_c \, g_{I\,n+1} \, \mathbf{n}_I \tag{6.47}$$

The gap $g_{I\,n+1}^{k+1}$ is defined as the difference between the current nodal position and the prescribed boundary displacement $\bar{\mathbf{x}}_I$ in direction of the surface normal to the rigid wall $\mathbf{n}_I$:

$$g_{I\,n+1} = \left(\mathbf{x}_{I\,n+1} - \bar{\mathbf{x}}_I\right) \cdot \mathbf{n}_I \tag{6.48}$$

For rigid contact, the prescribed boundary displacement $\bar{\mathbf{x}}_I$ and hence the nodal normal $\mathbf{n}_I$ are constant in time. Only the current nodal position $\mathbf{x}_{I\,n+1}^{k+1}$ is a function of the displacement increment and has to be linearized.

Thermal boundary

Motivated from Newton's law of cooling $(4.38)_1$, a penalty heat flux $\bar{q}$ is defined:

$$\bar{q} = -\alpha \left(\theta - \theta_0\right) \tag{6.49}$$

Here, the penalty parameter is identified as the heat transfer coefficient α. For a heat flux through a rigid wall, the area can be regarded as constant throughout the simulation. The surface increment related to an integration point $\mathbf{x}_l$ on the triangulated surface follows from the norm of the cross product of nodal coordinates $\mathbf{x}_I$:

$$\mathrm{d}A_l = \frac{1}{2} \left| \left(\mathbf{x}_1 - \mathbf{x}_2\right) \times \left(\mathbf{x}_3 - \mathbf{x}_2\right) \right| \tag{6.50}$$

In OTM, the initial configuration is a tetrahedral mesh. Hence, a triangulation of the surface is already known and imposes no additional computational effort. Nodal surface increments can be interpolated from:

$$\mathrm{d}A_I = \sum_{l} N_I\left(\mathbf{x}_l\right) \, \mathrm{d}A_l \qquad N_I\left(\mathbf{x}_l\right) = \frac{1}{3} \tag{6.51}$$

This yields to a node-wise imposition of the Robin boundary condition. The contribution to the global residual (6.13) becomes:

$$\mathrm{R}_{\theta}^{con} = \bigcup_{p=1}^{n_{mp}} \sum_{I=1}^{N_{p\,n}^{sup}} \frac{k}{h} \left(\theta_{I\,n+1} - \theta_0\right) \, \mathrm{d}A_I \tag{6.52}$$

Only the current temperature $\theta_{I\,n+1}$ must be linearized within the Newton-Raphson algorithm. While Newton's law of cooling is postulated for convection problems, the heat transfer coefficient α can also be motivated from a different standpoint. Assuming Fourier type heat flux, i.e. a linear temperature profile from the boundary temperature θ to a region in distance h where the temperature $\theta_0 = const.$ is in equilibrium, the boundary heat flux writes:

$$\bar{q} = -k \,\mathrm{grad}\, \theta \approx -k \frac{(\theta - \theta_0)}{h} \tag{6.53}$$

The quotient k/h is identified as the heat transfer coefficient α. This definition is useful for the interpretation of results in chapter 8, where the influence of cooling conditions on metal particle fusion is analyzed. Note that in the limit $\alpha \to \infty$, the penalty force mimics a Dirichlet boundary in the sense that $\theta \to \theta_0$. The linearizations of $\mathbf{R}_{\mathbf{u}}^{con}$ and $\mathbf{R}_{\theta}^{con}$ are provided in appendix B.

Chapter 7

Coupling of Ray Tracing and OTM

The theoretical basis of laser heat source modeling was discussed in chapter 5. Two common modeling approaches were introduced, namely volumetric heat sources and ray tracing. Here, a coupling algorithm for the Optimal Transportation Meshfree Method (OTM) with a ray tracing scheme developed in WESSELS ET AL. (2018) is described[1].

Using ray tracing, the laser beam is discretized into rays that strike the surface of the irradiated part. This is why the irradiation is often expressed by a surface integral. To compute the required surface increments, a triangulation of the free surface is necessary - a computationally very expensive operation. An additional challenge in meshfree methods is that surface nodes are not explicitly specified. In surface tension computations, this problem has been avoided by employing the Continuous Surface Force (CSF) model. This approach transforms the surface into a volume integral which is only defined in the proximity of the free surface. Following the same motivation, the ray energy can be absorbed at material points near the free surface. This is implemented by defining a detection sphere at each material point, see figure 7.1(a). Here, the detection radius r_p^{det} is set equal to the characteristic length of a support domain. The latter is obtained from the third root of material point volume v_p. A ray is absorbed by the material point that first detects it. The power P_p in the heat input vector $\mathbf{Q}$ (6.6) is obtained from the summation of all incident rays at that material point:

$$P_p = \sum_{r=1}^{n_{ray}} \begin{cases} (1 - R_r)\,\frac{E_r}{\Delta t} & \forall\, |\mathbf{x}_r - \mathbf{x}_p| < r_p^{det} \\ 0 \quad \text{else} \end{cases} \tag{7.1}$$

Here, n_{ray} is the total number of rays. The ray energy E_r has been defined in (5.6). The reflection coefficient R_r will be introduced later on in section 7.3. A graphical illustration of the ray detection according to (7.1) is provided in figure 7.1(a).

As discussed in section 5.1, the ray velocity $\mathbf{v}_r$ is scaled by a factor k^{red}. It has to be chosen carefully in order to fulfill the Courant-Friedrichs-Lewy condition. In any given time step, a ray may not travel further than the average characteristic length of support domains. This measure can be obtained prior to the first time step from the cubic root of averaged material point volume $\bar{v}_p$. The admissible ray velocity is directly computed from the product of

---

[1] The findings of this chapter are an extension of the master thesis of BODE (2017) and have been published previously in WESSELS ET AL. (2019).

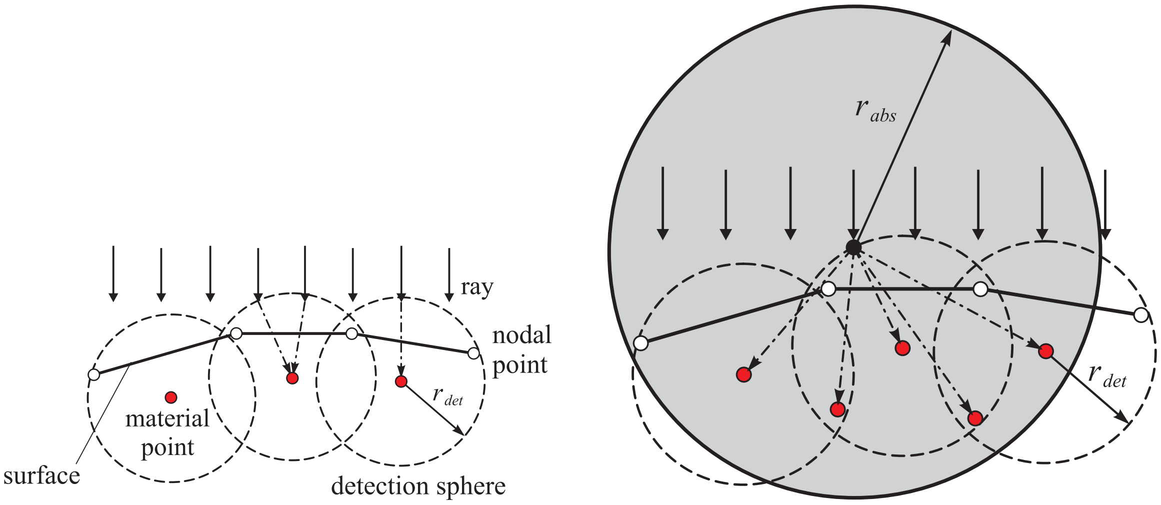

(a) Direct absorption at material point of incidence (b) Distribution of incident ray energy within r_{abs}

Figure 7.1. Absorption of rays. Left: Direct absorption at the material point that first detects a ray. Right: Redistribution of detected ray energy into a sphere of absorption radius r_{abs}.

physical ray velocity and scaling factor k^{red}:

$$k^{red}|\mathbf{v}_r| \leq C \, \frac{\bar{v}_p^{1/3}}{\Delta t} \tag{7.2}$$

The constant $C \in (0, 1]$ has been set to $2/3$. In the subsequent sections, the coupling of the ray tracing algorithm with the stabilized OTM method is discussed. Note that the presented coupling algorithm can be easily applied to other meshfree methods.

7.1 Influence of Spatial OTM Discretization

A perfectly insulated cubic block with an edge length of $40\,\mu$m is irradiated with a uniform, rectangular heat source. The laser beam is continuous. The setup is sketched in figure 7.2(a). In order to satisfy the stability criterion for explicit thermal schemes (6.10), the time increment in all simulations has been set to $\Delta t = 10^{-8}$ s. The material data can be found in table 8.2, (8.1) and (8.2). The laser discretization has been chosen such that a further refinement does not affect the results ($\Delta t_r = 10^{-7}$ s, $n_{rpl} = 500$).

The curve depicted in figure 7.2(b) shows that the maximum temperature increases with increasing number of nodal points. This can be explained mathematically from the volumetric heating (P_p/v_p):

$$\frac{P_p}{v_p} = \frac{1}{h_p}\frac{P_p}{a_p} \sim \frac{1}{h_p} \tag{7.3}$$

In the above equation, the material point volume v_p has been replaced by the product of characteristic length h_p and area a_p. Since the power P_p is proportional to a_p, the power per volume (P_p/v_p) is inversely proportional to h_p.

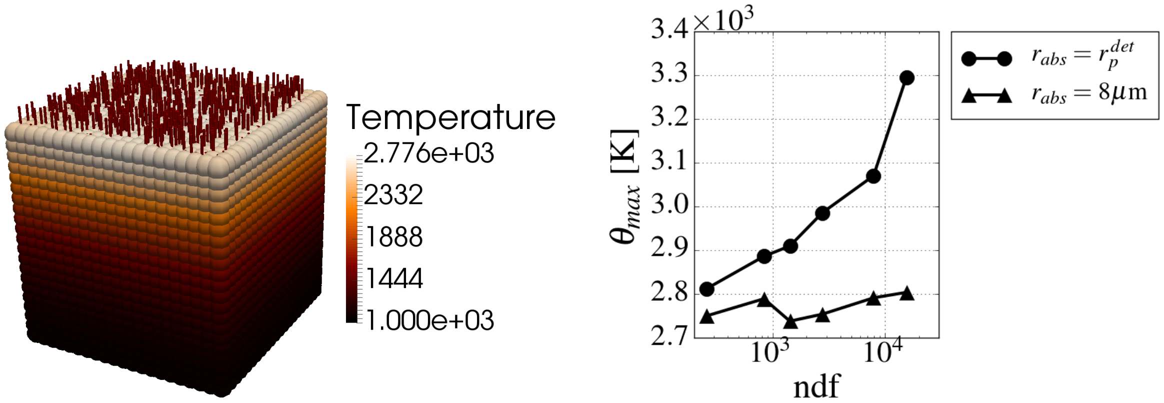

(a) Geometrical set up (b) Convergence study

Figure 7.2. Left: A cubic bloc with an edge length of $40\,\mu$m is irradiated with an uniform, rectangular heat source discretized into rays. Right: The maximum temperature in the block as a function of spatial OTM discretization with an absorption radius r_{abs} equal to and greater than r_p^{det}. These results have been published earlier in WESSELS ET AL. (2019).

For the coupled OTM ray tracing algorithm to converge, the power per volume needs to be independent of the OTM discretization. This can be achieved by distributing the incident ray energy within the neighborhood of a material point. The neighborhood can be modeled as a sphere with an absorption radius r_{abs} in the vicinity of a ray, see figure 7.1(b). Inside the absorption sphere, the incident ray energy is distributed with the weights w_p^{abs}. Their computation is based on a normalized Beer-Lambert law:

$$w_p^{abs} = \frac{Z_p}{\sum_q^{N_r^{abs}} Z_q} \qquad Z_p = \begin{cases} e^{-\beta|\mathbf{x}_r - \mathbf{x}_p|/r_{abs}} & \forall\, |\mathbf{x}_r - \mathbf{x}_p| < r_{abs} \\ 0 \quad \text{else} & \end{cases} \tag{7.4}$$

The use of a Beer-Lambert law can be motivated from the physical observation that the laser disperses into the irradiated body. In this work, the optical extinction coefficient has been set to $\beta = 1$. The concept is graphically illustrated in figure 7.1(b). A summary of the overall algorithmic implementation follows in figure 7.5.

Figure 7.2(b) highlights that convergence of the maximum temperature is reached with the presented non-local distribution of ray energy. Within the considered range, the deviation of the maximum temperature decreases from 17.2% to only 2.4%. The influence of r_{abs} on maximum temperature will be investigated in section 7.4.

7.2 Laser Discretization

The same perfectly insulated cubic block from the previous section is examined to study the influence of laser discretization in space and time. The block is discretized into 1422 nodes and 6587 material points. The laser beam is continuous in time and has a uniform, rectangular shape.

The ratio $n_{rpl}/\Delta t_r$ indicates the number of rays created per second. From a computational point of view, this ratio should be as small as possible in order to reduce cost. In figure 7.3,

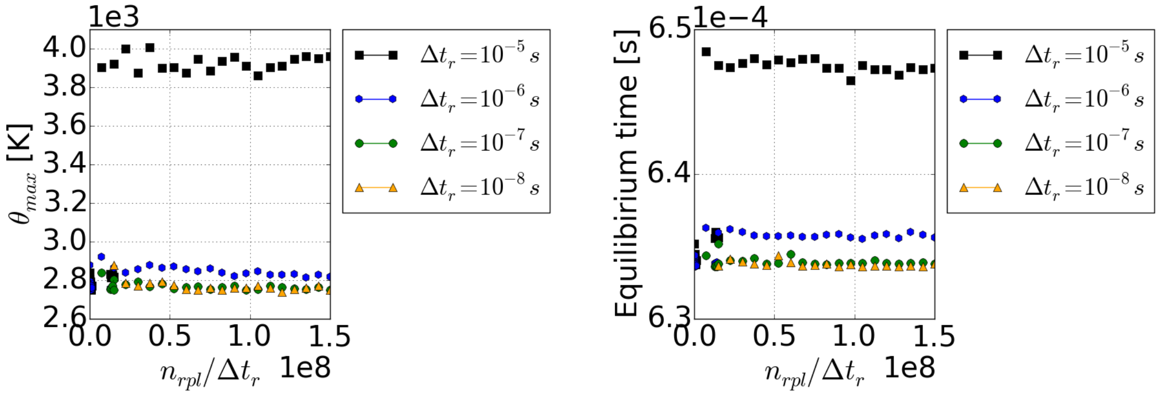

Figure 7.3. Irradiation of a perfectly insulated cubic block as depicted in figure 7.2(a). Influence of laser discretization on maximum temperature (left) and on the time to achieve equilibrium temperature (right). These results have been published earlier in WESSELS ET AL. (2019).

the maximum temperature and the time until equilibrium temperature is reached are plotted against the rays created per second. Four different time steps of ray creation Δt_r have been examined. The results suggest a time step size of ray creation Δt_r less or equal to ten times the simulation time step size Δt:

$$\frac{\Delta t_r}{\Delta t} \leq 10 \tag{7.5}$$

From figure 7.3 it can be deduced that 10^8 rays per second are enough to accurately discretize the laser beam, provided that the above condition is satisfied. To ensure convergence when an arbitrarily shaped part is irradiated, the laser spot must be accurately represented by absorption spheres with radius r_{abs}. The following criterion is proposed to estimate the necessary number of rays per level n_{rpl} to represent a laser spot of size A_{laser}:

$$n_{rpl} = \max\left(C\frac{A_{laser}}{\pi r_{abs}^2}, \quad 50\right) \tag{7.6}$$

Here, C is a safety factor accounting for the random positioning of rays. Its value has to be always larger than 1 and is set to $C = 15$ in the current analysis. This condition will be verified in section 7.4.

7.3 Reflection

The computation of reflection exhibits two main challenges within meshfree methods: First, a surface needs to be defined in order to compute the direction of the emergent ray. Second, the position of incidence is unknown. In this work, it is traced back and set as anchor point $\mathbf{x}_c$ of the surface. The surface normal $\mathbf{n}_{refl}$ at the anchor point is then computed from the weighted material point normals in its vicinity. The advantage of this methodology is that reflection can be computed without the need of a surface triangulation, since the rays identify the free surface themselves.

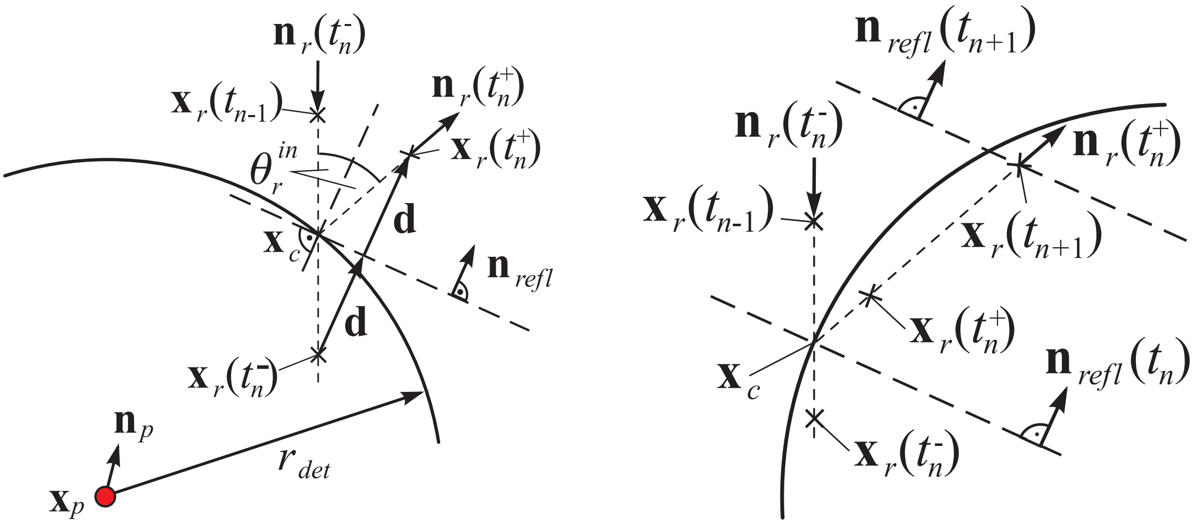
$\mathbf{n}_r(t_n^-)$
$\mathbf{x}_r(t_{n-1})$
$\mathbf{n}_r(t_n^+)$
$\mathbf{x}_r(t_n^+)$
θ_r^{in}
$\mathbf{d}$
$\mathbf{x}_c$
$\mathbf{n}_{refl}$
$\mathbf{d}$
$\mathbf{x}_r(t_n^-)$
$\mathbf{n}_p$
r_{det}
$\mathbf{x}_p$
$\mathbf{n}_{refl}(t_{n+1})$
$\mathbf{n}_r(t_n^-)$
$\mathbf{n}_r(t_n^+)$
$\mathbf{x}_r(t_{n-1})$
$\mathbf{x}_r(t_{n+1})$
$\mathbf{x}_r(t_n^+)$
$\mathbf{n}_{refl}(t_n)$
$\mathbf{x}_c$
$\mathbf{x}_r(t_n^-)$

(a) Reflection of an incident ray (b) Special case

Figure 7.4. Left: A surface is constructed from the OTM discretization at the anchor point $\mathbf{x}_c$ in order to compute the reflection. Right: The ray is reflected in time step t_n. It can not leave the detection sphere within one time step, i.e. the scalar product $(\mathbf{n}_r\,(t_n^+) \cdot \mathbf{n}_{refl}\,(t_{n+1}))$ is positive. Therefore, the ray proceeds without being reflected.

The anchor point $\mathbf{x}_c$ is defined as the intersection of a ray trajectory with the detection sphere of a material point. It lays on the line segment of length Δs from the ray position of the previous time step $\mathbf{x}_r\,(t_{n-1})$ to the ray position of the current time step prior to reflection $\mathbf{x}_r\,(t_n^-)$. This is illustrated in figure 7.4(a). The anchor point $\mathbf{x}_c$ is approached iteratively:

$$\mathbf{x}_c^{j+1} = \mathbf{x}_c^j \begin{cases} + \left(\Delta s/2^{j+1}\right) \cdot \mathbf{n}_r\left(t_n^-\right) & \forall \left|\mathbf{x}_c^j - \mathbf{x}_p\right| > r_p^{det} \\ - \left(\Delta s/2^{j+1}\right) \cdot \mathbf{n}_r\left(t_n^-\right) & \forall \left|\mathbf{x}_c^j - \mathbf{x}_p\right| < r_p^{det} \end{cases} \tag{7.7}$$

In the first iteration, $\mathbf{x}_c^0$ is initialized with the ray position prior to reflection. Ten iterations of (7.7) are sufficient. In order to keep the computational effort as low as possible, the surface normal $\mathbf{n}_{refl}$ at $\mathbf{x}_c$ is approached by the normal vector at the current ray position $\mathbf{x}_r\,(t_n^-)$. It is obtained by weighting the N_r^{abs} material point normals $\mathbf{n}_p$ inside the absorption radius r_{abs}. The material point normals are obtained by normalization of the color gradient $\mathbf{c}_p$ (6.18):

$$\mathbf{n}_{refl} = \sum_p^{N_r^{abs}} \mathbf{n}_p\, w_p^{norm} \qquad \mathbf{n}_p = \frac{\mathbf{c}_p}{|\mathbf{c}_p|} \tag{7.8}$$

This approximation acts as a smoothing of material point normals with the weights w_p^{norm}:

$$w_p^{norm} = \frac{Z_p}{\sum_{q=1}^{N^{abs}} Z_q} \qquad Z_p = \begin{cases} e^{-|\mathbf{x}_p - \mathbf{x}_r|/r_{abs}} & \forall \left|\mathbf{x}_p - \mathbf{x}_r\right| < r_{abs} \\ 0 \quad \text{else} \end{cases} \tag{7.9}$$

Based on the assumption that the emergent is equal to the incident angle, the ray positions are updated via:

$$\mathbf{x}_r\left(t_n^+\right) = \mathbf{x}_r\left(t_n^-\right) + 2\mathbf{d} \qquad \mathbf{d} = \left[\left(\mathbf{x}_c - \mathbf{x}_r\left(t_n^-\right)\right) \cdot \mathbf{n}_{refl}\right] \mathbf{n}_{refl} \tag{7.10}$$

```
1) Compute material point normals (equation 7.8)
2) If $(\Delta t_r \% \Delta t == 0)$: Initialize new layer of rays (equation 5.6)
3) Loop over rays $r$:
    Update ray positions (equation 5.8)
    Loop over material points $q$:
        If $|\mathbf{x}_r - \mathbf{x}_q| < r_q^{det}$:
            Compute anchor point $\mathbf{x}_c$ (equation 7.7)
            Loop over material points $p$:
                If $|\mathbf{x}_r - \mathbf{x}_p| < r_{abs}$:
                    Assemble weights $w_p^{abs}$ and surface normal $\mathbf{n}_{refl}$ (equation 7.4 and 7.8)
                    Store index of absorbing material point in list
            Normalize weights $w_p^{abs}$ and $\mathbf{n}_{refl}$ (equation 7.4 and 7.8)
            If $\operatorname{sgn}(\mathbf{n}_r \cdot \mathbf{n}_{refl}) < 0$:
                Compute reflectivity $R_r$ (equation 7.11 and 7.12)
                Update the reflected ray's position, energy and direction (equation 7.10 and 7.11)
                Loop over absorbing material points $p$:
                    Distribute ray power: $P_p {+}= (1 - R_r)\frac{\Delta E_r}{\Delta t} w_p^{abs}$
```

Figure 7.5. Algorithmic implementation of the coupled ray tracing OTM algorithm including ray absorption and reflection. The efficiency of the algorithm can be improved using linked lists or linked cells, see e.g. GRIEBEL ET AL. (2007).

The vector $\mathbf{d}$ is a projection of the vector pointing from the ray position prior to reflection to the anchor point $\mathbf{x}_c$ onto the surface normal $\mathbf{n}_{refl}$, see figure 7.4(a). The direction of the ray after reflection $\mathbf{n}_r\left(t_n^+\right)$ and the angle of incidence θ_r^{in} are obtained from:

$$\mathbf{n}_r\left(t_n^+\right) = \frac{\mathbf{x}_r\left(t_n^+\right) - \mathbf{x}_c}{\left|\mathbf{x}_r\left(t_n^+\right) - \mathbf{x}_c\right|} \qquad \theta_r^{in} = \arccos\frac{\mathbf{n}_r\left(t_n^-\right) \cdot \mathbf{n}_{refl}}{\left|\mathbf{n}_r\left(t_n^-\right) \cdot \mathbf{n}_{refl}\right|} \tag{7.11}$$

The energy associated with a reflected ray computes from the reflectivity R_r. It can be derived from the Fresnel-equations and yields (ZOHDI, 2013):

$$R_r = \frac{1}{2}\left[\left(\frac{\frac{\hat{n}^2}{\hat{\mu}}\cos\theta_r^{in} - \left(\hat{n}^2 - \sin^2\theta_r^{in}\right)^{1/2}}{\frac{\hat{n}^2}{\hat{\mu}}\cos\theta_r^{in} + \left(\hat{n}^2 - \sin^2\theta_r^{in}\right)^{1/2}}\right)^2 + \left(\frac{\cos\theta_r^{in} - \frac{1}{\hat{\mu}}\left(\hat{n}^2 - \sin^2\theta_r^{in}\right)^{1/2}}{\cos\theta_r^{in} + \frac{1}{\hat{\mu}}\left(\hat{n}^2 - \sin^2\theta_r^{in}\right)^{1/2}}\right)^2\right] \tag{7.12}$$

The ratios of magnetic permeabilities and refractive indices in the absorbing and the surrounding medium are denoted $\hat{\mu}$ and $\hat{n}$, respectively. A graphical illustration of the function $R_r\left(\theta_r^{in}, \hat{n}, \hat{\mu} = 1\right)$ can be found in ZOHDI (2013). In this work, the reflectivity (7.12) has been implemented with the constant values $\hat{\mu} = 1$ and $\hat{n} = 2.4$. The temperature and phase dependency of the reflectivity is therefore not included in the model.

Note that the speed of reflected rays may be too low to leave the detection sphere within one time step. To guarantee that a reflected ray is not reflected again before it has left the detection sphere, the sign of the scalar product $(\mathbf{n}_r \cdot \mathbf{n}_{refl})$ is checked. A positive sign indicates an already reflected and a negative sign an incident ray. This is illustrated in figure

7.4(b). The algorithmic implementation of the ray tracing scheme is summarized in figure 7.5.

7.4 Comparison of Heat Source Modeling

A sphere with a radius of $20\,\mu$m is irradiated for the duration $t_{irr} = 0.1$ ms. The sphere is discretized into 343 nodes and 1465 material points. The time step size in all simulations is $\Delta t = 10^{-7}$ s. The radial intensity distribution of the laser energy follows a normalized Gaussian distribution (5.5). The beam radius is $R = 20\,\mu$m and the laser power of the constant beam is given by $P_{laser} = 2.5$ W. The resulting temperature evolution using a Beer-Lambert type heat source and the ray tracing scheme are compared. With the ray tracing scheme, the absorption radius is $r_{abs} = 8\,\mu$m and reflection is computed as described in section 7.3.

It has been found that 82% of the emitted energy were absorbed with the ray tracing scheme. This result has been validated by comparison with the theoretical value of 81.3% obtained with the software *Mathematica*, see appendix C.2 for details. Hence, with the Beer-Lambert model a static absorption coefficient $\zeta = 0.82$ has been used. The powder bed depth L in (5.13) is equal to the diameter of the sphere, i.e. $L = 40\,\mu$m.

As was graphically illustrated in figure 5.2(b), the geometry of the sphere and the volumetric intensity distribution do not fully overlap. To overcome this issue, the following correction is introduced:

$$I^{corr}(r,z) = I(r,z)\,\frac{\pi R^2 L}{v_h^{HAZ}} \tag{7.13}$$

Here, $\pi R^2 L$ is the cylindrical volume affected by the intensity function $I(r,z)$ with R the laser beam radius. The discretized volume of the actual heat affected zone is denoted v_h^{HAZ}. The influence of the corrected intensity distribution (7.13) is evaluated in table 7.1 and graphically illustrated in figures 7.6(a) and 7.6(b). Without correction, about 25% less energy is absorbed by the sphere. However, the difference in equilibrium time is negligible. The reason is that the laser power is quite evenly distributed inside the volume according to the Beer-Lambert law. Hence, with the volumetric heat source increasing the power does not cause significantly larger temperature gradients.

The results obtained with the ray tracing scheme are depicted in figures 7.6(c) and 7.6(d). In figure 7.6(c), a very fine laser discretization has been used with $\Delta t_r = \Delta t$ and $n_{rpl} = 250$. In figure 7.6(d), the laser discretization has been chosen according to (7.5) and (7.6) yielding to $\Delta t_r = 10\Delta t$ and $n_{rpl} = 94$. The convergence study in figure 7.7 demonstrates that the criteria used to estimate the optimal laser discretization are valid. The maximum temperature obtained with $\Delta t_r = 10\Delta t$ only deviates about 2.42% compared to the smaller time step $\Delta t_r = \Delta t$ if n_{rpl} is chosen appropriately. Comparing the ray tracing approach with the volumetric heat source, it can be seen that the heat input is much more localized. The maximum temperature is about 66% higher and it takes 20% longer to achieve equilibrium time, see table 7.1. Even the maximum temperature and the consolidation time obtained with the corrected volumetric heat source heavily differ from the ray tracing results.

Additionally, in figure 7.8(a) the influence of the absorption radius r_{abs} is illustrated. For small values of r_{abs}, the heat input is strongly localized yielding to an increase of maximum

Temperature
2.200e+03
1900
1600
1300
1.000e+03
Temperature
2.200e+03
1900
1600
1300
1.000e+03

(a) Beer-Lambert

(b) Corrected Beer-Lambert

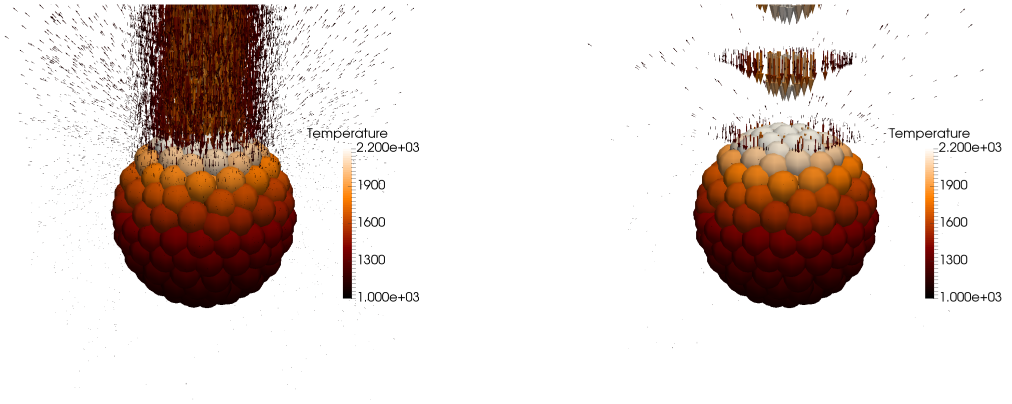
Temperature
2.200e+03
1900
1600
1300
1.000e+03
Temperature
2.200e+03
1900
1600
1300
1.000e+03

(c) High resolution ray tracing

(d) Sufficient ray discretization

Figure 7.6. Temperature distribution at $t = 0.1$ ms caused by laser irradiation with $P_{laser} = 2.5$ W (WESSELS ET AL., 2019).

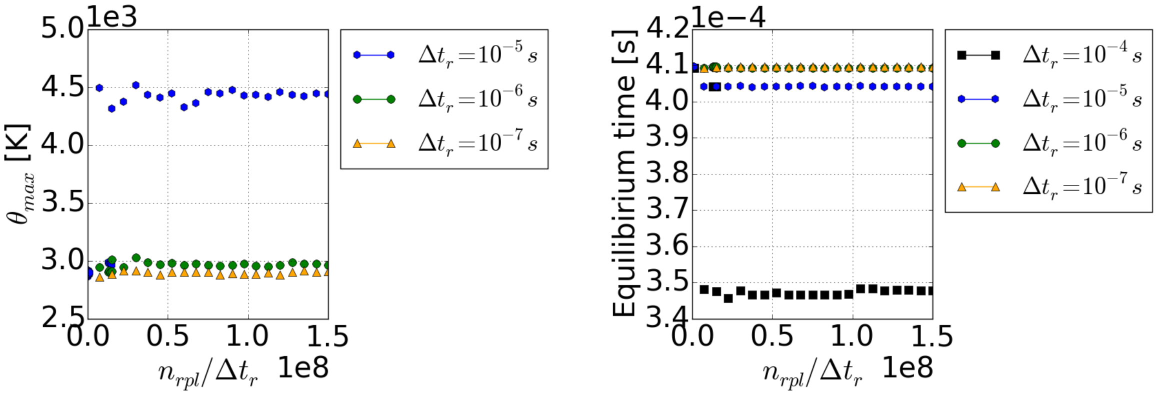

Figure 7.7. Influence of ray discretization on maximum temperature (left) and on the time to achieve equilibrium temperature (right) for an irradiated sphere. The time increment of the thermal problem is $\Delta t = 10^{-8}$ s. These results have been published earlier in WESSELS ET AL. (2019).

	Beer-Lambert	Corr. Beer-Lambert	Ray Tracing
Absorbed energy	0.152 mJ	0.206 mJ	0.206 mJ
Maximum temperature	1520 K	1758 K	2528 K
Equilibrium time	0.205 ms	0.207 ms	0.249 ms

Table 7.1. Results of sphere irradiation test case (WESSELS ET AL., 2019).

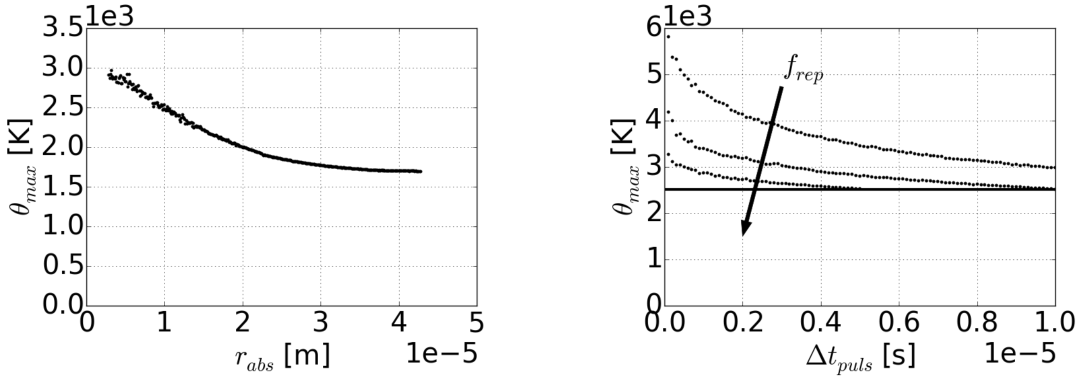

(a) Influence of absorption radius

(b) Effect of laser pulsing

Figure 7.8. Left: Influence of absorption radius r_{abs} on maximum temperature. Right: The effect of laser pulsing on maximum temperature (dotted) compared to a continuous laser beam (solid line) with $\Delta t = \Delta t_r = 10^{-8}$ s and $t_{irr} = 0.1$ ms. These results have been published earlier in WESSELS ET AL. (2019).

temperature. When larger values of r_{abs} are used, the laser is allowed to disperse deeper into the part. The heat is distributed more evenly. As a consequence, the maximum temperature is lower. With r_{abs} increasing further, θ_{max} converges towards a horizontal asymptote. In the outline of this work, the absorption radius has been set to $r_{abs} = 8\,\mu$m.

Note that in this simple numerical example, the CPU time using ray tracing is with 128% increase dramatically higher as compared to the volumetric heat source approach. This is due to the simplicity of the spherical geometry and its coarse spatial discretization. When the thermo-mechanical problem is solved and the number of degrees of freedom increases as in the example discussed in section 8.4, the additional computational effort is only about 3.3%.

7.5 Investigation of Laser Pulsing

The effect of laser pulsing on maximum temperature has been studied for the insulated sphere from the previous section. A rectangular laser pulse (5.2) is assumed and discretized into rays. Irradiation time and laser power have been set to $t_{irr} = 0.1$ ms and $P_{laser} = 0.25$ W, respectively. In figure 7.8(b), the maximum temperature is plotted as a function of the pulsing width Δt_{puls}. The effect of varying repetition rates $f_{rep} = \{50, 100, 200\}$ kHz is also investigated.

As graphically illustrated in figure 5.1, at constant repetition rate a smaller pulsing period yields a higher pulsing power. Per consequence, the maximum temperature decreases exponentially with increasing pulsing period. Keeping the pulsing period fixed, the pulsing power decreases with increasing repetition rate and the resulting maximum temperature drops. These effects are displayed by the curves in figure 7.8(b).

ZOHDI (2015b) has shown that in addition to a pulsing heat source a thermally relaxed heat equation is necessary to accurately predict heat waves. However, this requires the relaxation time as an additional model parameter. While CAPRIO ET AL. (2018) and MUMTAZ & HOPKINSON (2010) have investigated the effect of pulsing laser beams on melt pool characteristics and part quality experimentally, in practice often continuous laser beams are used. Therefore, the particle fusion analysis presented in the preceding chapter 8 will be restricted to this case.

Chapter 8

Metal Particle Fusion Analysis

The capability of the presented OTM framework to display the crucial physical phenomena in SLM is illustrated and examined by the means of numerical examples. Special focus lays on the influence of surface tension, laser power and cooling conditions on the processing result.

The choice of material parameters is discussed in section 8.1. The presented simulations illustrate that surface tension is the driving force for the fusion of powder particles. This result is confirmed by an order of magnitude analysis in section 8.2. In section 8.3, the influence of cooling conditions on the final processing result is analyzed. The impact of heat source modeling in SLM simulations is highlighted in section 8.4 by comparing ray tracing and a volumetric heat source. Note that the aforementioned evaluations have already been published in WESSELS ET AL. (2018) and WESSELS ET AL. (2019). As a new contribution, the enhanced consolidation model taking into account inelastic material behavior is assessed in section 8.5. While so far only a simple test case consisting of two metal powder particles has been considered, a more complex particle agglomerate is subject to laser irradiation in section 8.6.

8.1 Material Data

The determination of reliable material data for the high temperature range of interest is a crucial uncertainty for every simulation approach. Material data has been collected from various sources to account for the multiple physics occurring in SLM. The radical change of material properties related to a phase change is smoothed within a transition interval ΔT. For this purpose, artificial solidus and liquidus temperatures were defined as $T_{sol} = T_m - 0.5\Delta T$ and $T_{liq} = T_m + 0.5\Delta T$, respectively. Analogously, the artificial bubble and dew temperatures are $T_{bub} = T_v - 0.5\Delta T$ and $T_{dew} = T_v + 0.5\Delta T$. The latent heat of melting is incorporated in the heat capacity by increasing it about $c_{L_\theta} = L_m/\Delta T$ in the interval $\theta \in [T_{sol}, T_{liq}]$. For the latent heat of vaporization, the contribution is $c_{L_\theta} = L_v/\Delta T$ in the interval $\theta \in [T_{bub}, T_{dew}]$. The melting temperature as well as the latent heat of melting are taken from CHAWLA ET AL. (1981) while the vaporization temperature and the latent heat of vaporization were reported in GANERIWALA & ZOHDI (2016).

Mostly piece-wise linear simplifications of the primary material data were implemented. A

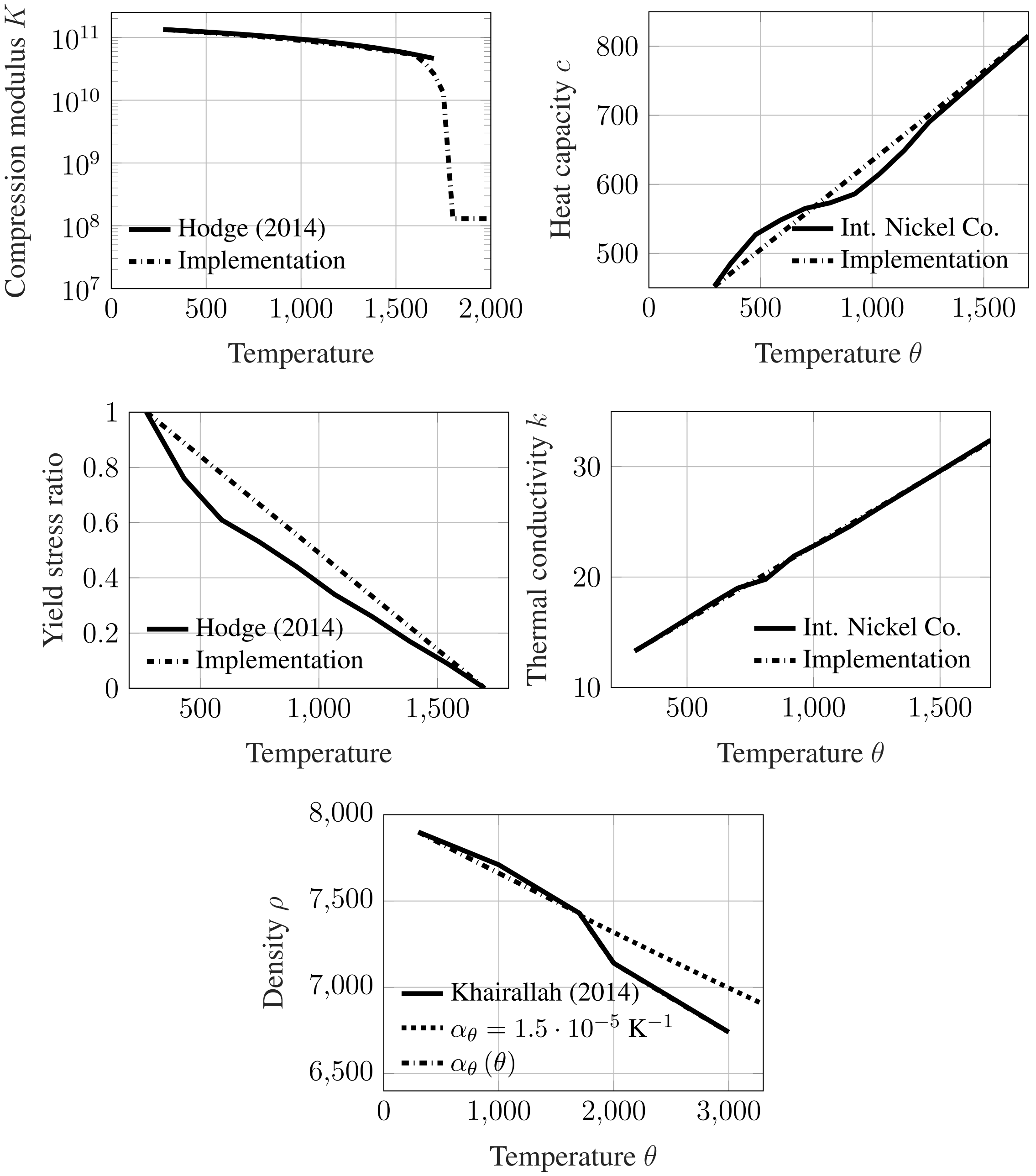

Figure 8.1. Dash-dotted the simplified piecewise linear temperature dependency of material properties compared to values reported by HODGE ET AL. (2014), KHAIRALLAH & ANDERSON (2014) and THE INTERNATIONAL NICKEL COMPANY (1978).

Thermomechanical parameter	Symbol	Value
Initial density	$\rho_0\,(\theta_{ini} = 300\,\mathrm{K})$	7900 kg/m^3
Poisson's ratio	ν	0.25
Viscosity of molten metal	η	0.1 kg/(s·m)
Surface tension coefficient	γ	1.7 N/m
Melting (evaporating) temperature	$T_m\ (T_v)$	1700 K (3130 K)
Latent heat of melting (vaporization)	$L_m\ (L_v)$	270.33 kJ/kg (6.09 MJ/kg)
Transition interval	ΔT	200 K
Initial yield limit	$\sigma_{Y0}\,(\theta_{ini} = 273\,\mathrm{K})$	206.85 MPa
Plastic hardening modulus	H_α	413.7 MPa
Thermal softening coefficient	H_θ	(1/1427) K^{-1}
Plastic viscosity	η_p	1 MPa·s
Perfectly elastic solid		
Compression modulus	K	130 MPa
Thermal expansion coefficient	α_θ	1.5 ·10^{-5} K^{-1}

Table 8.1. Material data of SS316L.

graphical comparison of the primary data and the simplified linear implementation is shown in figure 8.1. For the present purpose of analyzing the feasibility of the OTM as a predictive simulation tool for SLM, the accuracy is deemed sufficient. The heat capacity and the thermal conductivity reported by THE INTERNATIONAL NICKEL COMPANY (1978) have been slightly simplified in assuming a linear dependency of temperature in the range from room to melting temperature. The thermal conductivity is obtained from the relation:

$$k = \begin{cases} \left(0.0135\,\frac{1}{\mathrm{K}}\cdot\theta + 9.345\right)\frac{\mathrm{W}}{\mathrm{m\,K}} & \forall\,\theta\,\in[300\,\mathrm{K}, T_m] \\ 32.4\,\frac{\mathrm{W}}{\mathrm{m\,K}} & \forall\,\theta > T_m \end{cases} \tag{8.1}$$

And for the heat capacity it holds:

$$c = \begin{cases} \left(0.258\,\frac{1}{\mathrm{K}}\cdot\theta + 376.406\right)\frac{\mathrm{J}}{\mathrm{kg\,K}} & \forall\,\theta\,\in[300\,\mathrm{K}, T_m] \\ 815\,\frac{\mathrm{J}}{\mathrm{kg\,K}} & \forall\,\theta > T_m \end{cases} \tag{8.2}$$

In the range $\theta < T_{sol}$, the Young's modulus E is based on a linear approximation of the data reported by HODGE ET AL. (2014). For $\theta > T_{liq}$, E is set high enough to approach mechanical incompressibility in the liquid phase. In the transition interval $\theta \in [T_{sol}, T_{liq}]$, a linear relation between $E\,(T_{sol})$ and $E\,(T_{liq})$ is modeled to smooth the drastic change in material stiffness:

$$E = \begin{cases} \left(225.916 - 0.092\,\frac{1}{K}\cdot\theta\right)\ \mathrm{GPa} & \forall\,\theta < T_{sol} \\ \left(706.884 - 0.392605\,\frac{1}{K}\cdot\theta\right)\ \mathrm{GPa} & \forall\,\theta \in [T_{sol}, T_{liq}] \\ 0.195\,\mathrm{GPa} & \forall\,\theta > T_{liq} \end{cases} \tag{8.3}$$

In an approximation of the data reported by THE INTERNATIONAL NICKEL COMPANY (1978), a constant Poisson's ratio $\nu = 0.25$ is chosen. The compression modulus K and the second Lamé constant μ are related to Young's modulus E and Poisson's ratio ν via:

$$K = \frac{E}{3\,(1-2\nu)}, \qquad \mu = \frac{E}{2\,(1+\nu)} \tag{8.4}$$

Dilation and contraction in the presence of solid-liquid phase transformations are accounted for with a temperature dependent thermal expansion modulus α_θ (GOLDAK & AKHLAGHI, 2005). A piece-wise linear fit of the data reported by KHAIRALLAH & ANDERSON (2014) has been assumed. This yields to the following choice of α_θ and reference temperature θ_0:

$$(\alpha_\theta, \theta_0) = \begin{cases} (1.4604 \cdot 10^{-5}, 300\,\mathrm{K}) & \forall\, \theta < T_m \\ (4.4235 \cdot 10^{-5}, 1700\,\mathrm{K}) & \forall\, \theta \in [T_m, 3000\,\mathrm{K}] \\ (1.9218 \cdot 10^{-5}, 2000\,\mathrm{K}) & \forall\, \theta > 2000\,\mathrm{K} \end{cases} \tag{8.5}$$

Note that for a perfectly elastic model as described in WESSELS ET AL. (2018), compression modulus and thermal expansion coefficient are taken as constant with $K = 130$ MPa and $\alpha_\theta = 1.5 \cdot 10^{-5}\,\mathrm{K}^{-1}$.
The initial yield stress σ_{Y0} is taken from KARDITSAS & BAPTISTE (2018). In a reasonable approximation of the data reported by HODGE ET AL. (2016), σ_{Y0} is assumed to decay linearly with temperature. As already mentioned in section 4.2.1, the yield limit vanishes at the melting point and the thermal softening modulus computes from the relation $H_\theta = (T_m - \theta_0)^{-1}$. The initial yield stress σ_{Y0} and the thermal softening modulus H_θ are given in table 8.1. The hardening modulus is estimated to be in the order of twice the initial yield stress while the plastic viscosity is assumed to be constant at $\eta_p = 1$ MPa·s.

Remark: *The values for plastic hardening modulus and plastic viscosity are in the range of material data reported in the literature, see e.g.* GOLDAK & AKHLAGHI *(2005) and* SIMO & MIEHE *(1992). Clearly, for elasto-plasticity it is more accurate to approximate the hardening modulus from tensile strength data. Regarding elasto-visco-plasticity, more sophistacted models and material data can be found e.g. in* GOLDAK & AKHLAGHI *(2005). For the present purpose of analyzing the applicability of the OTM to SLM powder scale simulations, the choice of material parameter is deemed acceptable and provides qualitatively reasonable results.*

The viscosity of molten metal has been taken from HE ET AL. (2003). It is higher than the viscosity reported by KHAIRALLAH & ANDERSON (2014). SALDI ET AL. (2013) and PITSCHENEDER ET AL. (1996) also used higher viscosities. In the present work the higher viscosity from HE ET AL. (2003) has been used to enhance numerical stability.
KHAIRALLAH ET AL. (2016) report a linear temperature dependency of the surface tension coefficient γ:

$$\gamma\,(\theta) = \left(3.282 - 8.9 \cdot 10^{-4}\,\mathrm{K}^{-1}\,\theta\right) \frac{\mathrm{N}}{\mathrm{m}} \tag{8.6}$$

In the test cases presented in this chapter, the surface tension coefficient is assumed to be constant at $\gamma = 1.7$ N/m (CHAWLA ET AL., 1981). A graphical illustration of material parameters can be found in figure 8.1 and a tabular overview in table 8.1.

8.2 Influence of Surface Tension

To get an idea of the main driving forces in SLM, an order of magnitude analysis is performed. The relative importance of surface tension, Marangoni and gravity forces as well as recoil pressure is assessed. The momentum equation (4.36) including surface tension, Marangoni effect and recoil pressure as Neumann boundary conditions writes in strong form:

$$\begin{aligned} \rho\,\mathbf{a} &= \operatorname{div}\boldsymbol{\sigma} + \rho\,\hat{\mathbf{b}} \\ \boldsymbol{\sigma}\cdot\mathbf{n}|_{\Gamma_N} &= -\gamma\,\kappa\,\mathbf{n} - \operatorname{grad}_{\partial a}\gamma - p^{rec}\,\mathbf{n} \end{aligned} \tag{8.7}$$

A single sphere with a radius of $r = 20\,\mu$m is considered. Using Gauss's theorem, the divergence of Cauchy stress can be transferred into a surface integral to evaluate the relative importance of the Neumann boundary conditions. With the curvature $\kappa = 1/r$, the surface tension coefficient at the melting point $\gamma = 1.7$ N/m and the spherical surface $\mathrm{d}a = 4\pi r^2$, surface tension is estimated to be of the order $\mathcal{O}_{surf}\,(10^{-4}\,\mathrm{N})$:

$$\left|\int_a \gamma\,\kappa\,\mathbf{n}\;\mathrm{d}a\right| = 1.7\,\frac{\mathrm{N}}{\mathrm{m}}\cdot\frac{1}{r}\,4\pi r^2 = 4.27\cdot 10^{-4}\,\mathrm{N} \rightarrow \mathcal{O}_{surf}\left(10^{-4}\,\mathrm{N}\right) \tag{8.8}$$

Regarding the Marangoni force, a linear dependency of the surface tension coefficient γ on temperature as stated in (8.6) is assumed. The tangential gradient of γ can be derived using the chain rule:

$$\left|\int_a \operatorname{grad}_{\partial a}\gamma\;\mathrm{d}a\right| = |\frac{\partial\gamma}{\partial\theta}\operatorname{grad}_{\partial a}\theta|\,4\pi r^2 = 4.47\cdot 10^{-12}\,\frac{\mathrm{Nm}}{\mathrm{K}}\,|\operatorname{grad}_{\partial a}\theta| \tag{8.9}$$

Depending on the temperature gradient, the Marangoni force may reach an order of magnitude similar to the surface tension force. The recoil pressure is evaluated at the boiling point T_v, where the exponential in (4.43) equals one. With the ambient pressure $p_a = 10^5$ Pa, the order of magnitude is in the range $\mathcal{O}_{rec}\,(10^{-4}\,\mathrm{N})$:

$$\left|\int_a p^{rec}\,\mathbf{n}\;\mathrm{d}a\right| = 0.54\,p_a\,4\pi r^2 = 2.71\cdot 10^{-4}\,\mathrm{N} \rightarrow \mathcal{O}_{rec}\left(10^{-4}\,\mathrm{N}\right) \tag{8.10}$$

Since density decays with increasing temperature, the gravity force has its maximum at the initial ambient temperature prior to laser heating. Assuming $\rho = 7900$ kg/m^3, a gravity acceleration of $|\hat{\mathbf{b}}| = 10$ m/s^2 and substituting the volume integrand by $\mathrm{d}v = (4/3)\,\pi r^3$ yields:

$$\left|\int_v \rho\,\hat{\mathbf{b}}\;\mathrm{d}v\right| = 7900\frac{\mathrm{kg}}{\mathrm{m}^3}\cdot 10\frac{\mathrm{m}}{\mathrm{s}^2}\cdot\frac{4}{3}\pi r^3 = 2.64\cdot 10^{-9}\,\mathrm{N} \rightarrow \mathcal{O}_{grav}\left(10^{-9}\,\mathrm{N}\right) \tag{8.11}$$

The comparison suggests that surface tension, Marangoni effect and recoil pressure are equally important to the SLM process. Gravity forces and related buoyancy phenomena are outnumbered by these effects by five orders of magnitude. Note that the relative importance of driving forces can also be assessed with a dimensional analysis, see e.g. HE ET AL. (2003). FÜRSTENAU ET AL. (2019b) have shown that both dimensional analysis and the order of magnitude analysis as discussed here yield qualitatively the same result.

Gusarov source parameter	Symbol	Value	Numerical parameter	Symbol	Value
Optical thickness	λ	2	Time step	Δt	10^{-6} s
Hemispherical reflectivity	ρ_h	0.7	Stabilization constant	ε_s	10^{-8}
Powder bed depth	L	40 μm	Contact parameter	ε_c	$3 \cdot 10^6$
Particle diameter	D	40 μm	LME constant	γ^{LME}	1.2

Table 8.2. Heat source and numerical parameter.

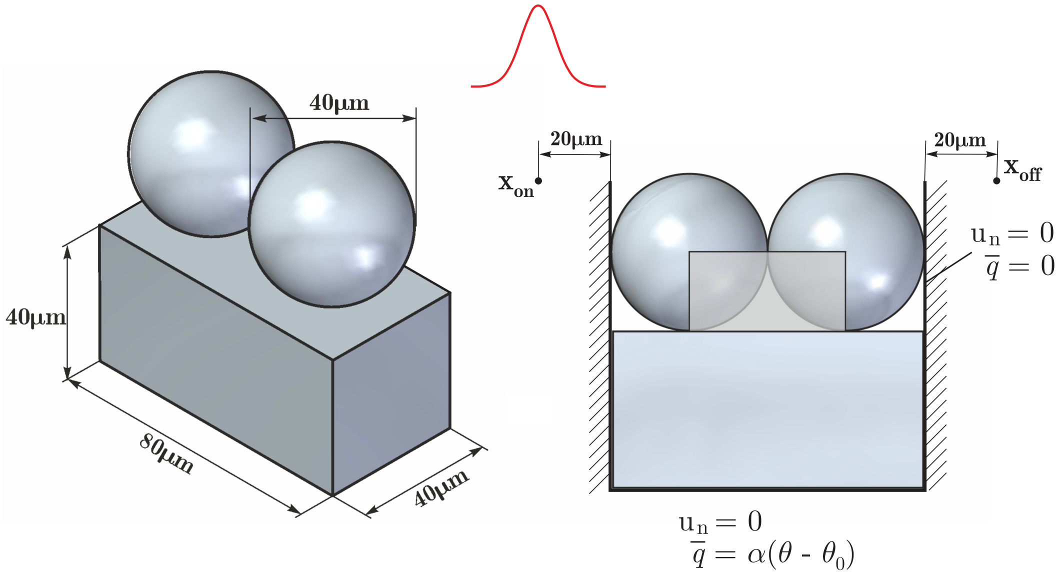
40µm
40µm
80µm
40µm
20µm
20µm
x_{on}
x_{off}
$u_n = 0$
$\overline{q} = 0$
$u_n = 0$
$\overline{q} = \alpha(\theta - \theta_0)$

Figure 8.2. Left: Geometrical set up of the numerical examples discussed in sections 8.2 - 8.4. Laser irradiation starts at the position x_{on} and ends at x_{off}. Right: Definition of the gap indicator as one minus the metal volume divided by the volume of the transparent box.

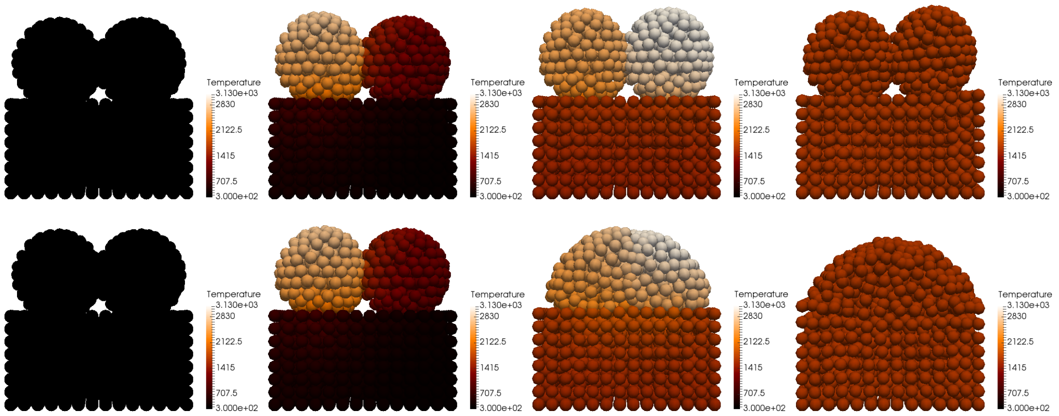
Temperature
3.130e+03
2830
2122.5
1415
707.5
3.000e+02

(a) $t = 0$ms (b) $t = 0.25$ms (c) $t = 0.75$ms (d) $t = 8.5$ms

Figure 8.3. Melting and solidification of two laser irradiated particles of 40 μm diameter. The laser power is $P = 22$ W. On the top, neglecting and on the bottom including surface tension effects (WESSELS ET AL., 2018).

A simple test case consisting of two metal powder particles with an equal diameter of 40 μm deposited on a solid substrate of $40\,\mu$m depth is considered[1]. The spatial discretization consists of 1691 nodes and 7441 material points. The ground plate is cooled from the bottom by imposing a Robin boundary condition (see section 6.6) with heat transfer coefficient $\alpha =$ 10^3 W/(m^{2}K). The laser power is 22 W, the beam radius is $R = 60$ μm and the scan speed $v_{laser} = 0.2$ m/s. Irradiation starts when the laser's focal midpoint is 20 μm in front of the part. The laser is turned off after the focal midpoint has crossed and traveled 20 μm away from the two particles. The geometrical setup is sketched in figure 8.2. The simulations were run until all nodal temperatures had dropped below the melting point. Residual stress formation is not investigated in this test case. Therefore, the perfectly elastic material model is employed. In the numerical examples, a constant surface tension coefficient $\gamma = 1.7$ N/m is used. Marangoni convection and recoil pressure have been neglected for reasons discussed later on in chapter 9. A volumetric Gusarov type heat source is employed. The heat source and numerical parameter can be found in table 8.2.

Figure 8.3 shows a comparison of simulations neglecting (top) and including (bottom) surface tension effects. If surface tension is neglected, only an expansion of the particles can be observed. While cooling, the particles go back to their initial shape. This is because the rapid consolidation prevents the metal from flowing. The time in the liquid phase is simply to short for gravity to accelerate the metal such that noticeable viscous deformation can occur. If surface tension is included in the model, the powder particles immediately fuse together once they become liquid - although the cooling is even faster. The greater contact area between the powder particles enhances the heat transfer through thermal conduction. With surface tension, the consolidation time decreases from 9.4 ms to 8.5 ms. This example shows that surface tension is the driving force for the fusion of powder particles. The result agrees with the findings from the order of magnitude analysis.

8.3 Influence of Cooling Conditions

The same test case from the previous section is considered to study the effect of laser heating and cooling conditions[1]. For this purpose, multiple parameter sets have been simulated in parallel automatically with a python script. The stabilized OTM code itself is serial, only the solution of the algebraic system of equations was performed with the parallel solver PARDISO. The work of LI ET AL. (2014) on a massively parallelized explicit OTM showcases future potential regarding computational time.

The fusion of metal powder particles is investigated by means of a gap indicator, the maximum temperature occurring during laser irradiation and the consolidation time. The latter is measured as the time until all nodal temperatures have dropped below the melting point. The gap indicator provides a measure of the fusion bond and is graphically illustrated in figure 8.2. It is defined as one minus the ratio of metal volume that lays inside a box spanned by the two midpoints of the powder particles and the initial surface of the solid substrate. For a perfect fusion bond the gap indicator becomes zero. In the initial state, the gap indicator Π

---

[1] The results presented in this section have been published earlier in WESSELS ET AL. (2018).

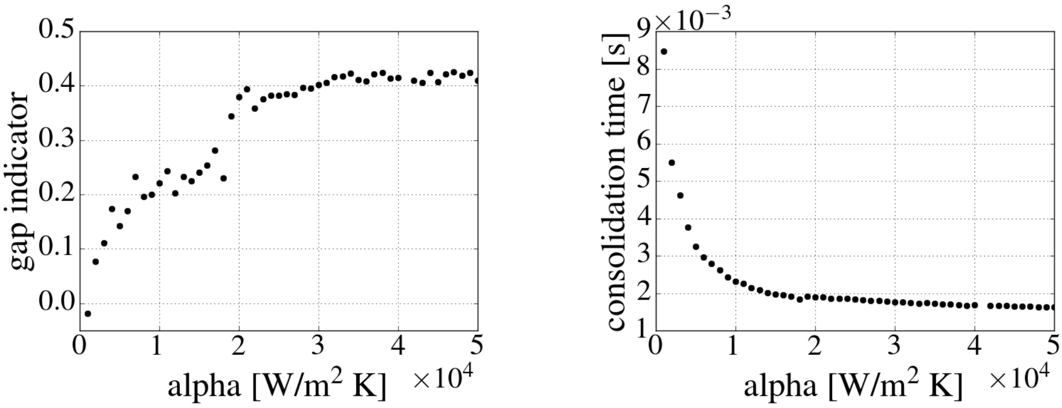

Figure 8.4. Gap indicator and cooling time as a function heat transfer coefficient at a laser power of $P = 22$ W (WESSELS ET AL., 2018).

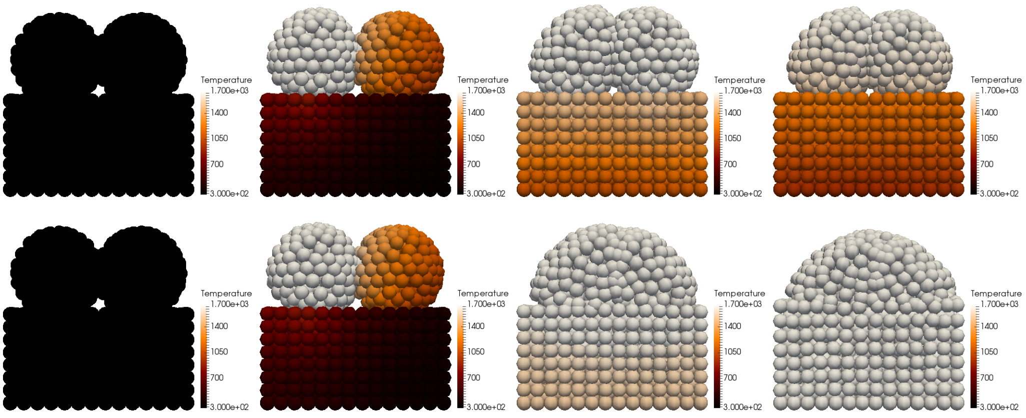

(a) $t = 0$ ms (b) $t = 0.25$ ms (c) $t = 0.75$ ms (d) $t = 1.76$ ms

Figure 8.5. Fusion of metal powder with a heat transfer coefficient $\alpha_{bulk} = 3 \cdot 10^4$ W/(m^{2}K) (top) and $\alpha_{powder} = 10^3$ W/(m^{2}K) (bottom) at a laser power of $P = 22$ W. White nodes are liquid. Melting of the underlying substrate is necessary to achieve optimal fusion. The consolidation time for α_{powder} is with $t = 8.5$ ms considerably longer (see figure 8.6). This figure is taken from WESSELS ET AL. (2018).

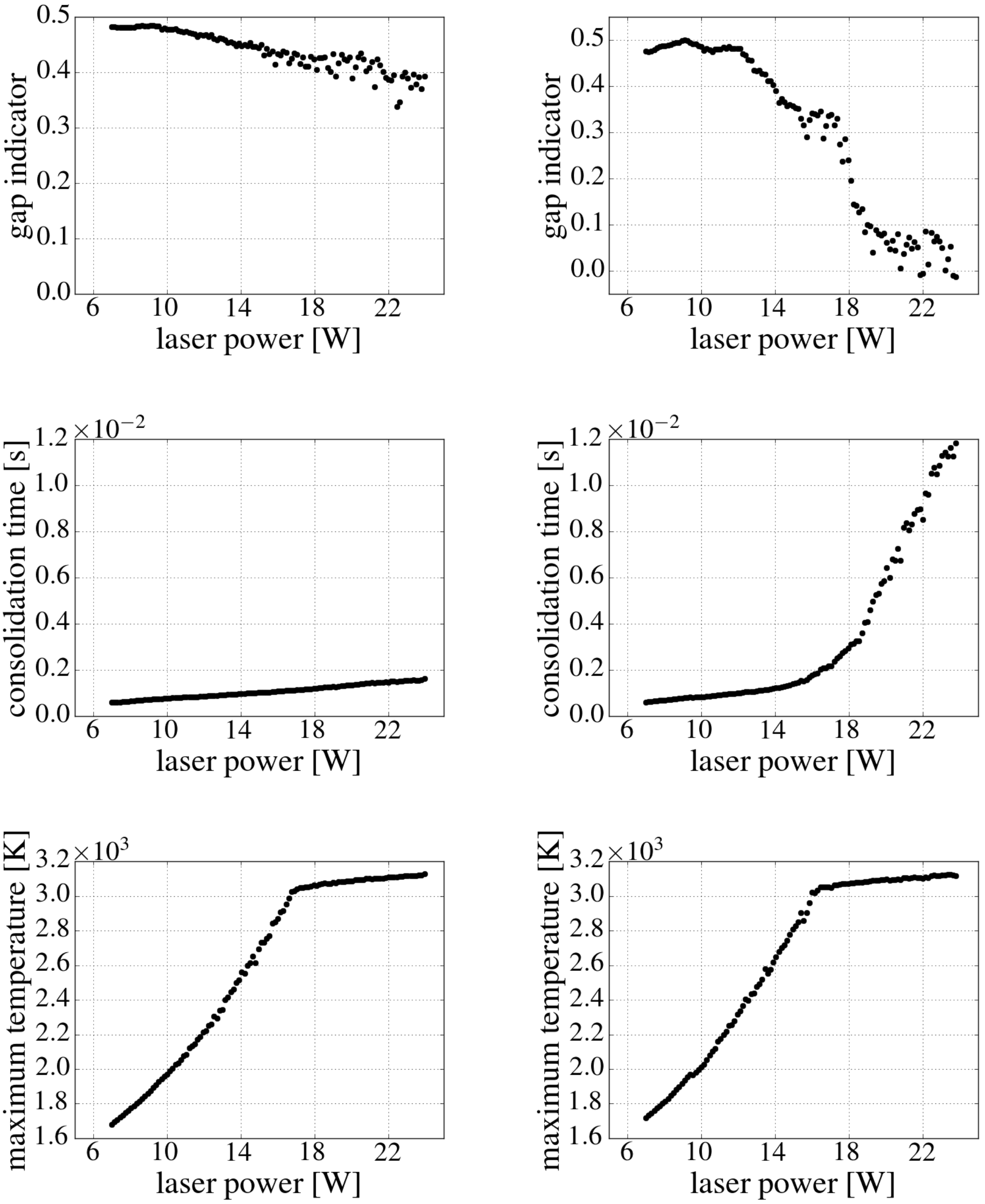

Figure 8.6. Gap function, cooling time and maximum temperature as a function of laser power for different heat transfer coefficients α. Left: $\alpha_{bulk} = 3 \cdot 10^4$ W/(m^2 K). Right: $\alpha_{powder} = 10^3$ W/(m^2 K). These results have been published earlier in WESSELS ET AL. (2018).

is equal to one minus the packing density:

$$\Pi = 1 - \frac{v_{metal}}{v_{box}} \approx 0.48 \tag{8.12}$$

The effect of heat transfer coefficient on gap indicator and consolidation time is investigated at a laser power of 22 W in figure 8.4. The lower the heat transfer coefficient, the more heat gets trapped and the better the fusion. The consolidation time decreases exponentially with increasing heat transfer coefficient. For a value of α larger than $3 \cdot 10^4$ W/(m^{2}K), gap indicator and consolidation time remain nearly constant.

In section 6.6, the heat transfer coefficient has been introduced as the quotient of thermal conductivity k and the distance h to a region with equilibrium temperature $\theta_0 = const.$ Keeping h constant, a variation of α is related to a different thermal conductivity within that region. In the context of SLM, this can occur due to the difference in thermal conductivity of bulk and powdered material. The heat transfer coefficients $\alpha_{bulk} = 3 \cdot 10^4$ W/(m^{2}K) and $\alpha_{powder} = 10^3$ W/(m^{2}K) have exemplary been chosen to investigate the effect of bulk and powdered material in the proximity h of the simulation domain. For these two cases, gap indicator, consolidation time and maximum temperature are plotted as functions of laser power in figure 8.6. With the heat transfer coefficient of bulk material the heat can easily escape. Within the considered power interval the gap remains nearly constant. As graphically illustrated in figure 8.5, the solid substrate does not melt. Melting of the substrate is crucial for a proper fusion of metal powder particles. The consolidation time is a linear function of laser power. In the region around the boiling point, the latent heat of evaporation is absorbed and released. This leads to a decay of the temperature evolution and to a sharp kink in the maximum temperature.

In case of underlying powder, heat gets trapped in the melt pool causing the solid substrate to melt. This is again illustrated in figure 8.5. Here, the gap indicator decreases with laser power. It approaches zero for a laser power greater than 20 W. While the maximum temperature evolution is not affected by the difference in heat transfer coefficient, it takes considerably longer for the material to drop below the melting point.

Note that no significant influence of the spatial and temporal discretization on the presented results have been observed. Details on the convergence behavior for this test case are given in appendix D.1.

Remark: *The stability of the LME shape function computation (see section 6.4) is highly sensitive to the particle distribution. Large deformations occur especially at higher laser powers where strong surface tension forces act on the melt pool. In this regime, the LME Newton-Raphson algorithm may suffer from convergence problems and cause early interruptions of the simulations. In the present work, this type of instability has been circumvented by incrementally increasing the enlarge factor* c^{enla} *which controls the size of support domains via the search radius extension factor (6.36). It was introduced in the context of the search algorithm in section 6.3. Cleary, this procedure is computationally expensive and the fact that the stability of the OTM is influenced by a numerical factor is alarming. The enlarge factors corresponding to the results shown in figure 8.6 are provided in appendix D.2. Other limitations of the OTM will be discussed in chapter 9.*

8.4 Impact of Heat Source Modeling

The ray tracing algorithm and the Gusarov-type volumetric heat source are compared by means of a parameter study[2]. Again, the same test case from the preceding sections depicted in figure 8.2 is considered. The heat transfer coefficient on the bottom is $\alpha_{powder} = 10^3$ W/(m^{2}K).

The three quantities of interest, i.e. gap indicator, consolidation time and maximum temperature are plotted as functions of laser power and absorbed energy in figure 8.7. When plotted against the laser power, the difference between ray tracing and volumetric Gusarov model is significant. Two reasons are responsible for this difference: First, in the Gusarov model, a bell-like radial intensity distribution (5.10) has been used, while a normalized Gaussian distribution (5.5) was assumed with the ray tracing model. Second, and most importantly, at the same laser power less energy is distributed into the part with the Gusarov model. This is due to the insufficient overlap of volumetric intensity distribution and geometry, c.f. figure 5.2(b).

Figure 8.8 shows that the absorbed energy linearly depends on the laser power. Note that the absorbed energy is an outcome of the simulation and depends on the heat source formulation. Only the laser power can be used as an input parameter. When plotted against the absorbed energy, gap function and consolidation time are nearly identical for both heat source models. An important difference exists in the maximum temperature evolution. With both schemes, the maximum temperature increases up to a kink, where the slope of the curve drastically decreases. This is the onset of vaporization. The absorption of latent heat in the temperature interval around the boiling point $T_v = 3130$ K delays the maximum temperature evolution. With the ray tracing scheme, the slope within this region is larger compared to the Gusarov-type heat source. After leaving the absorption interval, the slope of the maximum temperature increases again. The difference in the evolution of the maximum temperature can be explained graphically from figure 8.9. With both heat source models, the same amount of energy has been absorbed by the system. Using the volumetric heat source, the heat is more evenly distributed. Vaporization occurs homogeneously within a relatively large region. The maximum temperature lies within the absorption interval of the latent heat of vaporization. Using ray tracing, the heat input is much more localized, leading to a small region near the surface where the metal is vaporized. In the simulations, vaporized material points have not been removed from the computations but instead have been modeled as melt, so that the final geometry looks identical to the one obtained with the volumetric heat source. Nevertheless, the dramatic effect of heat source modeling on vaporization is illustrated.

The simulations highlight two key advantages of ray tracing over volumetric heat source approaches: First, the absorbed energy can be computed much more precisely based on the Fresnel equations. Second, a local layer of vaporization can be predicted. Numerical parameters in the Fresnel equations and the absorption radius can be adjusted to fit experimentally measured results independently of the irradiated geometry.

---

[2] The results presented in this section have been published earlier in WESSELS ET AL. (2019).

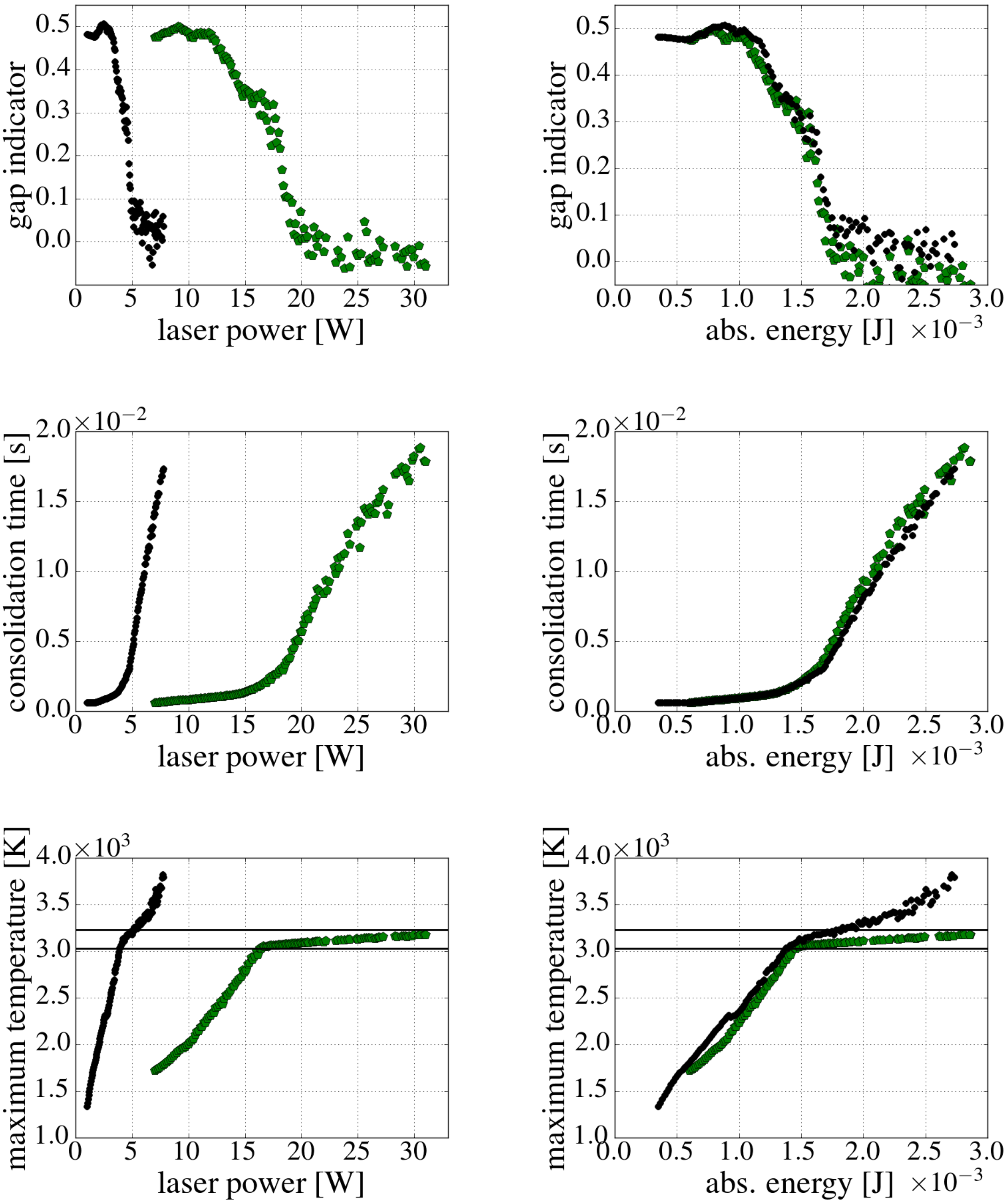

Figure 8.7. Gap function, cooling time and maximum temperature as a function of laser power (left) and absorbed energy (right) with $\alpha_{powder} = 10^3$ W/(m^2 K). The results obtained with the ray tracing algorithm (black dots) are compared to those when a Gusarov-type heat source (green pentagon) is used. The solid lines in the third row mark the interval in which the latent heat of vaporization is absorbed. These results have been published earlier in WESSELS ET AL. (2019).

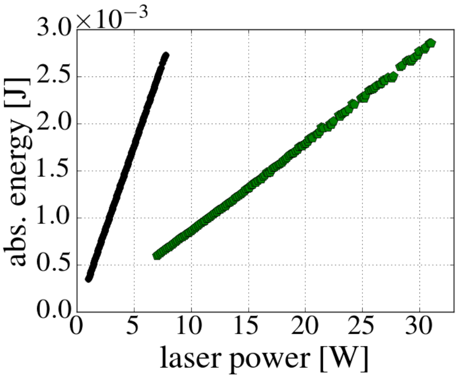

Figure 8.8. Absorbed energy as a function of laser power with the ray tracing scheme (black dots) and a volumetric heat source (green pentagons). This result has been published earlier in WESSELS ET AL. (2019).

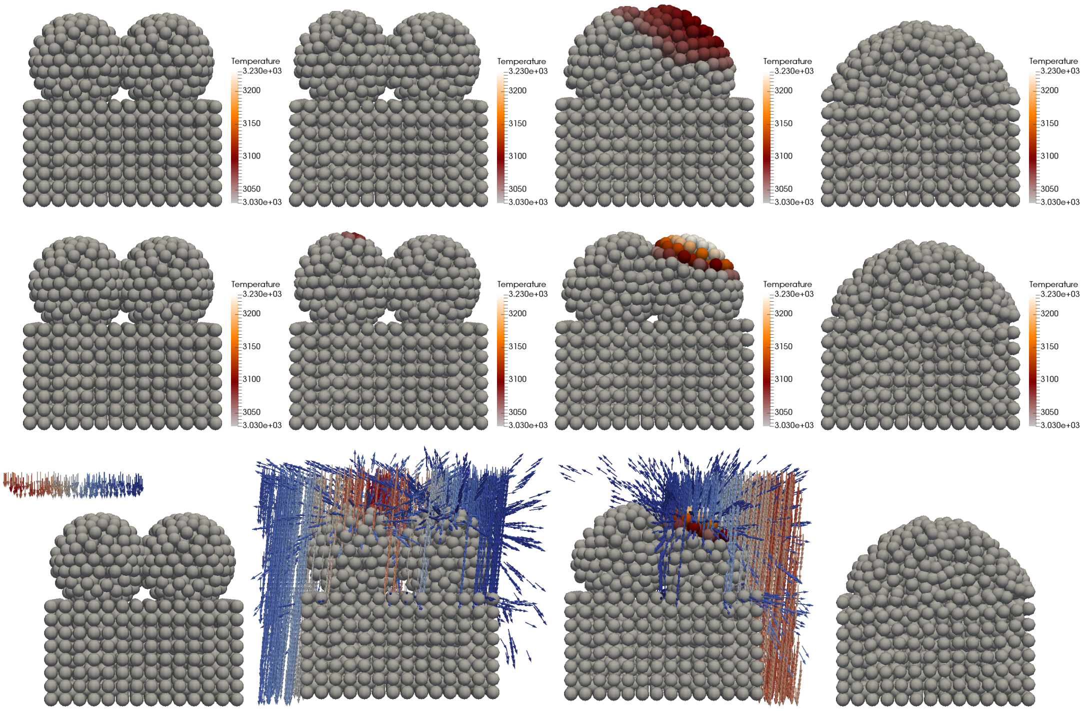

(a) $t = 0$ ms (b) $t = 0.25$ ms (c) $t = 0.6$ ms (d) $t = 6.65$ ms

Figure 8.9. Melting and solidification of two laser irradiated metal particles that absorb the energy 1.97 mJ. On the top, the laser is described with a volumetric heat source and in the middle and on the bottom with the ray tracing algorithm. In the middle, the rays are hidden to highlight the localized heat input. The temperature is scaled to the interval in which the latent heat of vaporization is absorbed. This figure is taken from WESSELS ET AL. (2019).

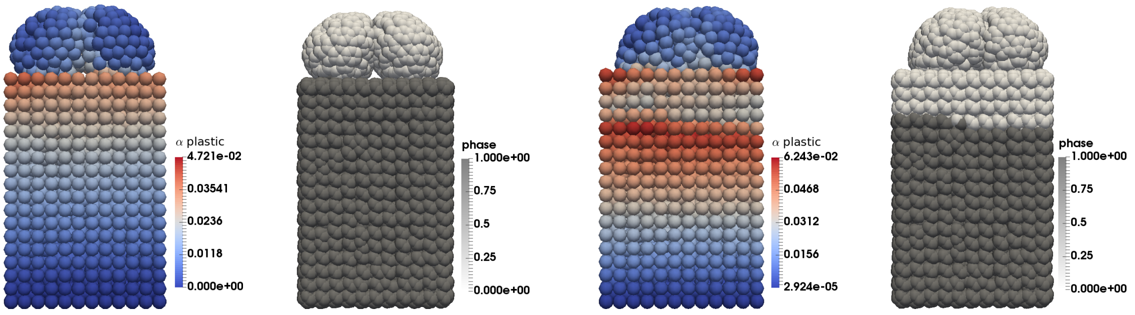

(a) $P = 9.85$ W (b) $P = 21.85$ W

Figure 8.10. Accumulated plastic strain and phase fractions of solid and resolidified regions at the cooled stated for two different laser powers. Plastic deformation concentrates unbeneath the resolidified zone. The plastic deformation at the topmost corners is related to inhibited thermal expansion caused by the Dirichlet type displacement boundary conditions.

8.5 Consolidation Analysis

In order to investigate the formation of residual stress in a two-particle system, it is necessary to cool the system down to ambient conditions. To accelerate the cooling process, the Neumann boundary on the bottom of the solid substrate as depicted in figure 8.2 is replaced by a Dirichlet type boundary. The ambient temperature is increased to 823.15 K, which is also the value of the boundary temperature. The increased ambient temperature mimics a preheated build chamber, which in SLM is a strategy to reduce residual stress formation caused by sharp thermal gradients. Additionally, the solid substrate beneath the two metal powder particles is stretched to a depth of $120\,\mu$m. The spatial discretization consists of 2508 nodes and 9165 material points. The heat source is of Gusarov type with the parameters listed in table 8.2. The simulations are run until all nodal temperatures have dropped below 10 K above the ambient temperature. Beside the cooling time, the total accumulated plastic strain as the sum of material point values, the gap indicator, the maximum temperature and the melt depth are evaluated. The melt depth is measured from the top of the two particles, i.e. the solid substrate is molten for a melt depth greater than $40\,\mu$m.

The measures of interest are plotted as functions of laser power in figure 8.11. In the power interval from 16 to 18 W, the cooling time remains nearly constant. The reason is a significant drop of the gap indicator from 0.35 to about 0.2 within this interval. The improved fusion bond allows the heat to escape faster. As a consequence, an increase in laser power has no effect on the cooling time.

Above 16 W, the melt depth increases linearly with laser power. Interestingly, from this point on the total accumulated plastic strain becomes independent of the melt depth and remains constant. This may be explained from the maximum temperature, which enters the absorption interval of latent heat at a laser power of 14 W. From there on, the maximum temperature increases only slightly. While the maximum temperature occurs at the top of the domain, the temperature on the ground plate is fixed to ambient conditions. When top and bottom temperatures are constant, the thermal gradients which are responsible for the residual stresss formation vary only due to geometrical changes. A measure for the geomet-

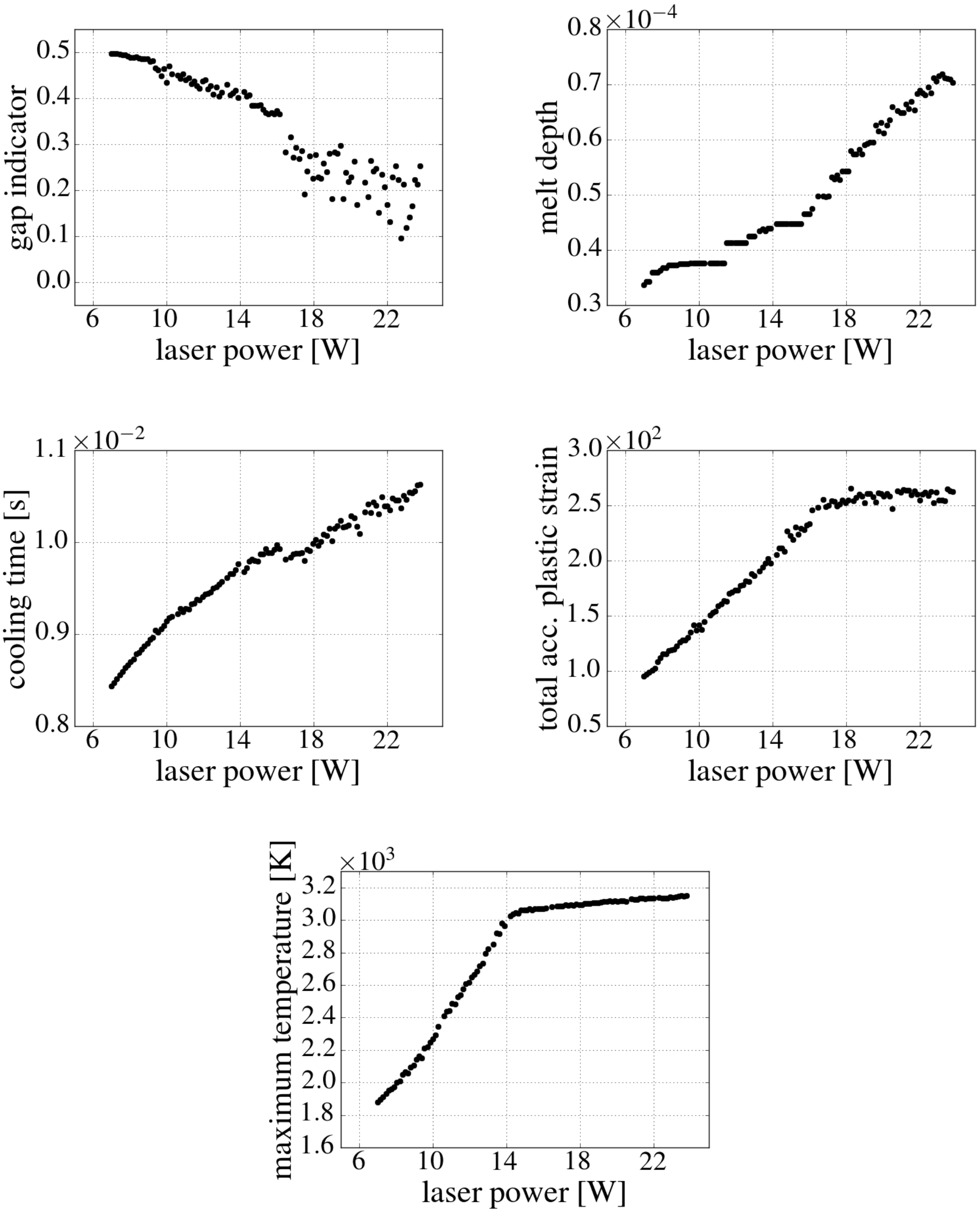

Figure 8.11. Gap function, melt depth, cooling time, total accumulated plastic strain and maximum temperature as functions of laser power.

rical change is the gap indicator, which is constant for laser powers greater than 16 W. Since above 16 W both maximum temperature and gap indicator are constant, the same applies to the total accumulated plastic strain.

Figure 8.10 illustrates that the accumulated plastic strain concentrates in the proximity of the re-solidified zone. During laser processing, the yield limit in this region has nearly vanished. However, no phase change occurred and the accumulated plastic strain was never deleted, which explains the concentration at exactly this position. Other peaks in accumulated plastic strain are observed at the topmost corners of the solid bloc. These originate from the Dirichlet type displacement boundaries on the faces. The boundaries inhibit thermal expansion, which favors residual stress formation and plastic deformation.

Different from the results discussed in the preceding sections, the gap indicator does not reach zero in this test case. The reason is that the period in which the metal is liquid and subject to strong surface tension is much shorter. Note that a Dirichlet type boundary corresponds to a heat transfer coefficient $\alpha \to \infty$.

8.6 Melting of Packed Powder

The applicability of the OTM to display melting of more complex powder agglomerates is investigated next. For this purpose, five particles were deposited on a solid substrate with a DEM packing algorithm described in BODE (2017). The ground plate has the dimension $(120 \times 120 \times 80)\,\mu$m. Heat escapes via a Robin type boundary condition with heat transfer coefficient $\alpha_{powder} = 10^3$ W/(m^{2}K) through the bottom of the domain. The spatial discretization consists of 2740 nodes and 12124 material points. The laser starts $20\,\mu$m before the part and travels at a constant speed of 0.2 m/s as far as $20\,\mu$m behind the part. Due to the complex geometry, ray tracing is the heat source model of choice. The laser beam of radius $R = 60\,\mu$m is discretized into $n_{rpl} = 1074$ rays per layer and the time step of ray creation Δt_r is equal to the simulation time step of $\Delta t = 10^{-6}$ s.

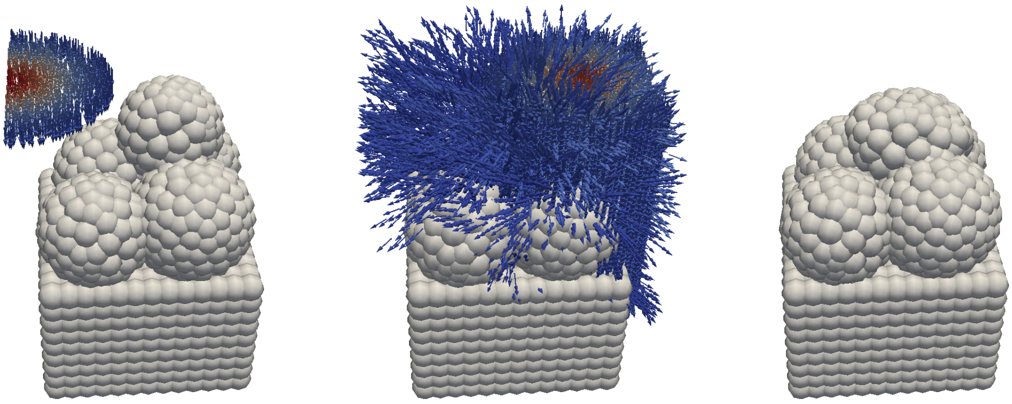

(a) $t = 0$ ms (b) $t = 0.6$ ms (c) $t = 1.767$ ms

Figure 8.12. Laser irradiation and melting of a powder agglomerate. The laser power is $P = 14$ W, the scan speed $v_{laser} = 0.2$ m/s and the beam radius $R = 60\,\mu$m.

Figure 8.12 shows the simulation result for this test case obtained with a laser power of $P = 14$ W. Only the topmost particle is deformed and fuses to the surrounding particles. Within the considered laser power interval from 5 to 23 W, no satisfying fusion result could be obtained. The reason are inaccuracies in the surface tension computation that have been identified. This issue will be addressed in detail in the next chapter.

Chapter 9

Limitations of the OTM

Although the results presented in the preceding chapter are promising, severe limitations have been encountered in the OTM framework. Two issues have already been mentioned earlier: WEISSENFELS & WRIGGERS (2018) have found that the OTM suffers from insufficient integration and suggested a stabilization through a penalty regularization. This stabilization has been introduced in section 6.2.3. Another problem is the limited stability of the Newton-Raphson algorithm for the computation of LME shape functions on arbitrary support domains. This issue has been circumvented by incrementally adapting a numerical parameter impacting the size of support domains (see sections 8.3 and 6.4). In this chapter, an additional limitation will be discussed. It has been found that severe difficulties exist in the OTM method which discredit the trustworthiness of simulations including surface tension effects. In this chapter, first the implementation of Marangoni convection is addressed in section 9.1. This effect has been neglected in the numerical examples presented earlier. Next, the curvature is analyzed in section 9.2. A general discussion of accuracy within OTM computations follows in section 9.3.

9.1 Marangoni Convection

Marangoni convection is caused by a temperature induced tangential gradient of the surface tension coefficient $\gamma(\theta)$. TONG & BROWNE (2014) suggest a transformation of surface tension into a volumetric force analogously to the Continuous Surface Force (CSF) model introduced by BRACKBILL ET AL. (1992). As discussed in section 6.2, this force is nonzero only within a narrow region of width $h = [\tilde{c}]/|\mathbf{c}|$ in the proximity of the free surface or interface, where $\tilde{c}$ is a smoothed color function and $\mathbf{c}$ its gradient (6.17). The surface integrand $\mathrm{d}a$ is substituted by the volume integrand $\mathrm{d}v$ divided by the width h. In analogy to (6.12), the surface traction caused by Marangoni convection yields in weak form:

$$\int_a \boldsymbol{\eta} \cdot \mathbf{t}^{rec} \, \mathrm{d}a = -\int_a \boldsymbol{\eta} \cdot \mathrm{grad}_{\partial a} \, \gamma \, \mathrm{d}a \approx -\int_v \boldsymbol{\eta} \cdot \mathrm{grad}_{\partial a} \, \gamma \, \frac{|\mathbf{c}|}{[\tilde{c}]} \, \mathrm{d}v \tag{9.1}$$

As discussed in section 4.3.1, the tangential gradient $(\mathrm{grad}_{\partial a} \, \gamma)$ can be expressed in terms of the global gradient minus the gradient in normal direction (4.41). Implementing (4.41) into

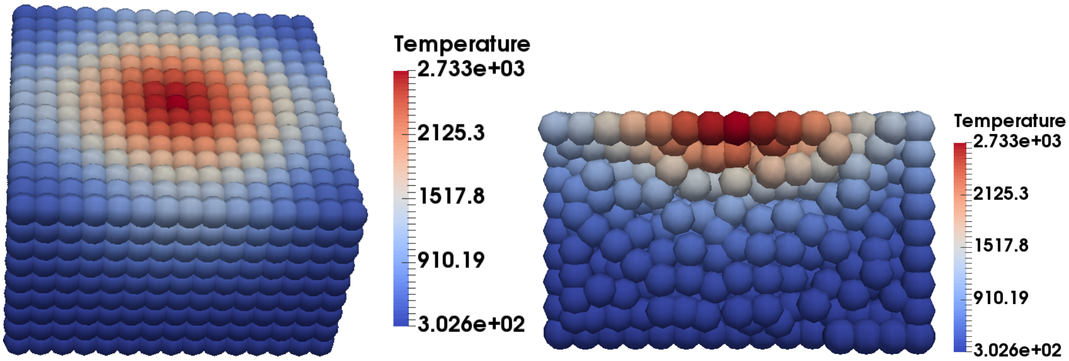
Temperature
2.733e+03
2125.3
1517.8
910.19
3.026e+02
Temperature
2.733e+03
2125.3
1517.8
910.19
3.026e+02

Figure 9.1. Nodal temperature profile after 20 ms of laser irradiation with $P_{laser} = 1800$ W, $R = 0.95$ mm and $L = 0.2$ mm. Left: full bloc, right: mid-section.

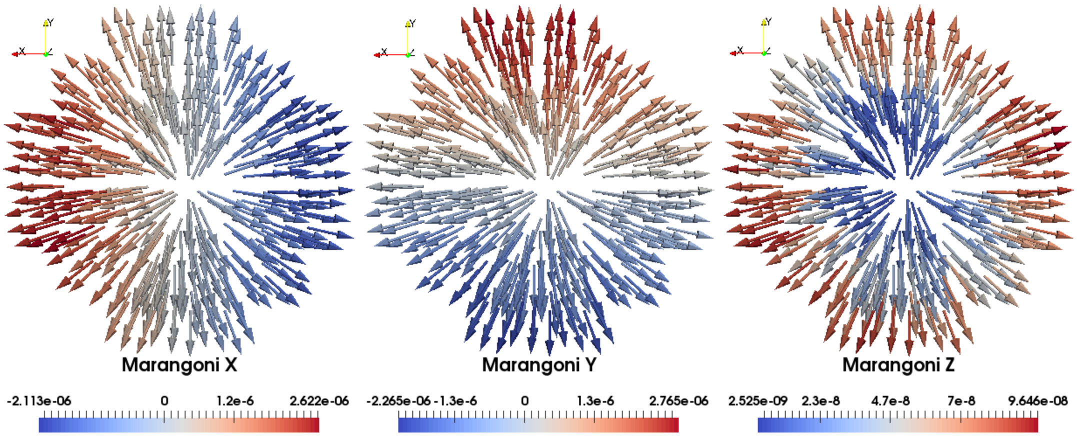
Y
X
Marangoni X
-2.113e-06
0
1.2e-6
2.622e-06
Y
X
Marangoni Y
-2.265e-06
-1.3e-6
0
1.3e-6
2.765e-06
Y
X
Marangoni Z
2.525e-09
2.3e-8
4.7e-8
7e-8
9.646e-08

Figure 9.2. Top view on Marangoni force vector at material points near the molten free surface. Coloring is according to the x, y, z components (from left to right). The z-component is two orders of magnitude smaller compared to the tangential components, i.e. the force is neatly oriented parallel to the free surface.

(9.1) yields in discrete form the following Marangoni force vector:

$$\begin{aligned} \mathbf{P}^{mar} &= \bigcup_{p=1}^{n_{mp}} \sum_{I}^{N_I^{inf}} \sum_{J}^{N_p^{sup}} N_I\left(\mathbf{x}_{pn}\right) \mathbf{f}_{pn}^{mar} \frac{|\mathbf{c}_{pn}|}{[\tilde{c}_{pn}]} v_{pn} \\ \text{with} \quad \mathbf{f}_{pn}^{mar} &= -\frac{\partial N_J\left(\mathbf{x}_{pn}\right)}{\partial \mathbf{x}_{pn}} \gamma_{Jn}\left(\theta_{Jn}\right) + \mathbf{n}_{pn}\left(\mathbf{n}_{pn} \cdot \frac{\partial N_J\left(\mathbf{x}_{pn}\right)}{\partial \mathbf{x}_{pn}} \gamma_{Jn}\left(\theta_{Jn}\right)\right) \end{aligned} \tag{9.2}$$

The Marangoni force vector $\mathbf{P}^{mar}$ is added to the load vector $\mathbf{P}$ (6.16). Here, the normal at the material point $\mathbf{n}_{pn}$ is interpolated from the nodal values as already introduced in the context of ray reflection (7.8). Note that $\mathbf{f}_{pn}^{mar}$ is smoothed within five iterations over the neighboring material points analogously to the smoothing of curvature (6.19).

Next, the implementation of Marangoni convection into the OTM framework is illustrated by means of a numerical example. In a simple test case motivated from HU & EBERHARD (2016), a $(2 \times 2 \times 1.15)$ mm bloc discretized into 2242 nodes and 10791 material points is

irradiated for 20 ms with a laser. The laser has a Gaussian shape (5.5) and penetration into the part is modeled with the Beer Lambert law (5.12). The power is P_{laser} = 1800 W, the beam radius $R = 0.95$ mm and the penetration depth $L = 0.2$ mm. As in WESSELS ET AL. (2018), inelastic contributions in the solid phase are neglected and a constant compression modulus $K = 130$ MPa is employed. Thermal expansion is also neglected. A linear temperature dependency of the surface tension coefficient γ is assumed (8.6). The remaining parameters for this test case are the same as listed in section 8.1.
In figure 9.1, the temperature profile at $t = 20$ ms is plotted. Figure 9.2 shows the resulting Marangoni force. The arrows are neatly oriented parallel to the free surface and the results qualitatively agree with the ones presented in HU & EBERHARD (2016). While this sounds promising, difficulties arise when the free surface is uneven as in a metal powder bed. The problem lays in the identification of the narrow region of width h in which the Marangoni force is acting. The error also affects curvature computations which are independent of temperature and therefore are easier to analyze than the Marangoni effect. Details will be discussed in the subsequent section.

9.2 Curvature

The accuracy of curvature computations with FEM and OTM using two concurrent approaches is analyzed. The first approach is already known from chapter 6, where the curvature at material points was defined as the global divergence of nodal normals inside the support domain (6.17). Alternatively, the curvature can also be defined as the arithmetic mean of principal curvatures calculated from a curvature tensor. While only the second approach yields accurate results with FEM, no reliable approach could be found for OTM. In the remainder of this section, first the different methods are introduced. Subsequently, the numerical results and their implications are discussed.

Methodology

As discussed in BRACKBILL ET AL. (1992), the global divergence operator can be additively split into a tangential and a normal part. When assuming that the divergence of the normal in normal direction is equal to zero, the global derivatives can be used directly to compute the curvature. This assumption leads to the definition of curvature according to (6.17):

$$\kappa_{p\,n} = \sum_{I}^{N_{p\,n}^{sup}} \frac{\partial N_I\left(\mathbf{x}_{p\,n}\right)}{\partial \mathbf{x}_{p\,n}} \cdot \mathbf{n}_{I\,n} \tag{9.3}$$

BRACKBILL ET AL. (1992) have employed this approach in two dimensional computations and obtained accurate results. It has also been used throughout the preceding chapters. However, FÜRSTENAU ET AL. (2019b) have shown that in three dimensional computations it overestimates the curvature. To overcome this problem, the curvature is alternatively computed as the arithmetic mean of two principal curvatures in tangential direction:

$$\kappa_{p\,n} = \frac{1}{2}\left(\kappa_{1\,n} + \kappa_{2\,n}\right) \tag{9.4}$$

The principal curvatures are the variation of the normal in tangential direction with respect to the local coordinate system. In order to avoid the direct computation of local derivatives, a global curvature matrix is calculated which is then transformed into the local space. From the local curvature matrix, the principal curvatures are computed from the eigenvalues corresponding to the tangential bases. For this purpose, first the global curvature matrix $\mathbf{K}^{p\,global}$ is introduced as the gradient of nodal normals computed at a material point:

$$\mathbf{K}^{p\,global} = \sum_{I}^{N_{pn}^{sup}} \mathbf{n}_{I\,n} \otimes \frac{\partial N_I\left(\mathbf{x}_{pn}\right)}{\partial \mathbf{x}_{pn}} \tag{9.5}$$

The local bases consist of the material point normal $\mathbf{n}_p$ (7.8) and two tangents. The first tangent is computed as the cross product of the normal with any Cartesian basis vector that is linearly independent of $\mathbf{n}_p$, for instance:

$$\mathbf{t}_{pn}^1 = \begin{cases} \mathbf{n}_{pn} \times (0,1,0) & \text{if} \quad |\mathbf{n}_{pn} \times (0,1,0)\,| \geq 0.01 \\ \mathbf{n}_{pn} \times (1,0,0) & \text{else} \end{cases} \tag{9.6}$$

The second tangent $\mathbf{t}_p^2$ must be orthogonal to both $\mathbf{n}_p$ and $\mathbf{t}_p^1$, which is fulfilled for the cross product of both vectors:

$$\mathbf{t}_{pn}^2 = \mathbf{n}_{pn} \times \mathbf{t}_{pn}^1 \tag{9.7}$$

The metric $T_{ij} = \mathbf{G}_i \cdot \mathbf{L}_j$ transforms the components of the curvature tensor from the global into the local coordinate system. The tensor $\mathbf{G}_i$ is the identity matrix representing the global Cartesian basis vectors while $\mathbf{L}_p = \left(\mathbf{n}_p, \mathbf{t}_p^1, \mathbf{t}_p^2\right)$ represents the local bases. The components of the local curvature tensor $\mathbf{K}^{p\,local}$ become:

$$K_{kl}^{p\,local} = T_{ki}^T\, K_{ij}^{p\,global}\, T_{jl} \tag{9.8}$$

Since only derivatives in tangential direction are of interest, the row and the column of $K_{kl}^{p\,local}$ related to the local base vector $\mathbf{n}_p$ can be deleted. The eigenvalues of the remaining two by two matrix are the principal curvatures of interest whose arithmetic mean (9.4) yields the curvature κ_p at the material point. As suggested by BRACKBILL ET AL. (1992) and discussed in chapter 6, the curvatures are smoothed within the neighborhood, see (6.19) and figure 6.2.

Remember that the surface force is only allowed to act within a narrow band of width $h = [\tilde{c}]\,/|\mathbf{c}|$. The color gradient $\mathbf{c}$ must only be non-zero within this region. Nodes where the color gradient is equal to zero must not contribute to the curvature. It will be demonstrated that this condition can not be fulfilled within the OTM. To illustrate this deficiency by means of numerical examples, the color gradient is slightly modified from the definition in (6.17). The first modification is that the color gradient is set to zero if its magnitude falls below a threshold ε. Initially, the threshold is simply set to $\varepsilon = 10^{-16}$, which is deemed to be numerically equivalent to zero. The importance of the threshold for the accuracy of curvature computations is studied later on. Secondly, instead of using the density as color like in BRACKBILL ET AL. (1992) or the mass as in chapter 6, here the volume is employed. When evaluating the curvature in the very first time step, the density is constant and interchanging

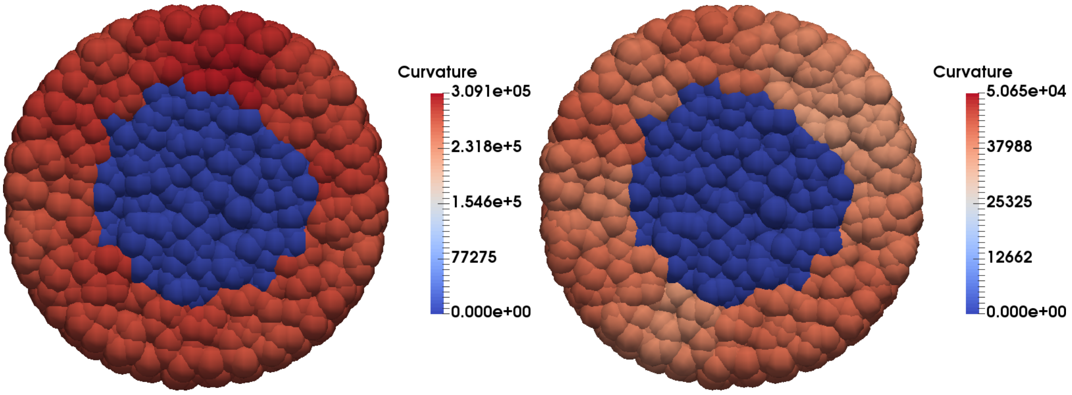
Curvature
3.091e+05
2.318e+5
1.546e+5
77275
0.000e+00
Curvature
5.065e+04
37988
25325
12662
0.000e+00

Figure 9.3. FEM curvature computation using a global divergence operator (left) and using principal curvatures (right). The analytical value is $\kappa = 5{\cdot}10^4$ m^{-1}. The figures show cutting planes through the center of a 3D sphere.

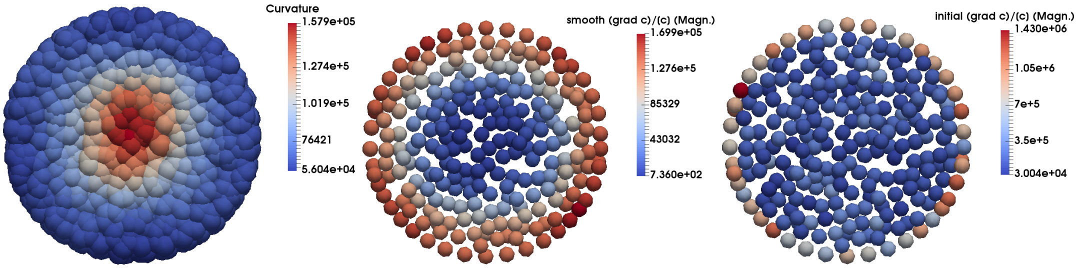
Curvature
1.579e+05
1.274e+5
1.019e+5
76421
5.604e+04
smooth (grad c)/(c) (Magn.)
1.699e+05
1.276e+5
85329
43032
7.360e+02
initial (grad c)/(c) (Magn.)
1.430e+06
1.05e+6
7e+5
3.5e+5
3.004e+04

Figure 9.4. Left: Curvature at material points computed with OTM from principal curvatures. The maximum curvature is in the center of the sphere. Center: The smoothed nodal color gradient does not vanish inside the sphere, yielding to false curvatures. Right: The initial nodal color gradient prior to smoothing. Some large magnitudes are observed in the center and some low magnitudes on the surface of the sphere. All figures are midsections of a 3D sphere.

mass, density and volume as color function does not affect the results. However, the choice of the volume is necessary for the interpretation of numerical results. Hence, the nodal color gradient can be rewritten as:

$$\mathbf{c}_I = \begin{cases} \sum_p^{N_I^{inf}} \frac{\partial N_I(\mathbf{x}_p)}{\partial \mathbf{x}_p} v_p & \text{if} \quad |\mathbf{c}_I| \geq \varepsilon \\ 0 & \text{else} \end{cases} \tag{9.9}$$

The nodal volume v_I is interpolated inside the influence domain. Again, color gradient $\mathbf{c}_I$ and nodal color $\tilde{c}_I = \tilde{v}_I$ are smoothed independently of each other according to (6.19).

Numerical results

A simple test case with an analytical solution is considered. The curvature of a sphere with radius $r = 20\,\mu$m is known to be equal to the inverse of its radius, i.e. $\kappa = 1/r = 5 \cdot 10^4$ m^{-1}. For the FEM computations, linear tetrahedral elements with one integration point are used. This is also the initial setup for the OTM computations. The sphere is discretized into

	Material points	Nodes	min(C)	max(C)
CUBIT	11924	2325	$0.6 \cdot 10^{-7}$	$1.0 \cdot 10^{-7}$
CUBIT	13366	2992	$3.0 \cdot 10^{-7}$	$5.0 \cdot 10^{-7}$
Abaqus	20135	4006	$3.0 \cdot 10^{-7}$	$5.0 \cdot 10^{-7}$

Table 9.1. Admissible range of the cutoff parameter C for a tolerance in curvature error of $\pm 20\%$ at different discretizations.

a total of 2325 nodes and 11924 material, i.e. integration points. In figure 9.3, the curvature obtained with FEM is plotted for the two different approaches. In agreement with the results reported by FÜRSTENAU ET AL. (2019b), calculating the curvature from (9.3) largely overestimates the real curvature, here about a factor greater than five. When the principal curvatures are used, the error in maximum curvature is reduced to only 1.3%. Although when using this second approach FEM reproduces realistic curvatures, their computation with OTM is still ambiguous. Results obtained with OTM and the principal curvature approach are shown in figure 9.4. The maximum curvature is observed within the center of the sphere and is considerably larger compared to the realistic maximum curvature.

The reason becomes clear when looking at the color gradient from which the surface normals are computed. In figure 9.4 (right), the initial non-smoothed color gradient has some large values in the center and some low values at the boundary. Per consequence, when smoothing, the magnitude of the smoothed color gradient becomes never zero. Hence, all interior nodes are considered within the curvature computation, which introduces large gradients. In an attempt to improve accuracy, a discretization dependent cutoff criterion ε is introduced. It is motivated from SPH simulations, where MORRIS (2000) could show that a cutoff criterion depending on the smoothing length yields excellent results. For OTM computations, a criterion is employed which takes into account the nodal volume v_I and a constant C:

$$\varepsilon = C\, v_I^{\frac{1}{3}} \tag{9.10}$$

Different meshes using Abaqus and CUBIT have been tested and it has been found that the admissible range of C heavily depends on the initial mesh. Even if large errors in curvature of $\pm 20\%$ are accepted, the admissible range of C is prohibitively narrow for dynamic computations, see table 9.1. In addition, it was found that increasing the size of support domains has no positive effect on the accuracy of surface tension. The narrow range of C and its sensitivity to changes in the initial discretization make surface tension computations with OTM unreliable: If C is too low, an erroneous surface tension force is acting inside the entire continuum; if C is too high, the surface tension force becomes discontinuous. Since in SLM surface tension is the main driving force, this is a severe problem. Nevertheless, as illustrated in chapter 8, the computations show a trend pointing in the right direction. The general accuracy of the OTM method will be discussed in the following section.

9.3 Accuracy

The fact that the normal computation yields vectors inside the continuum has another consequence. CHEN ET AL. (2001) have introduced an integration constraint for Galerkin mesh-

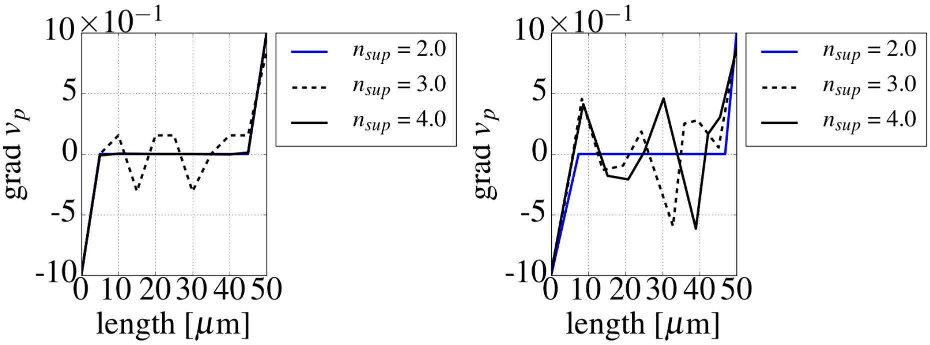

Figure 9.5. The integration constraint on an even (left) and irregular (right) discretization consisting of 11 nodes and 10 material points. Only FEM ($n_{sup} = 2$) and OTM with symmetric support domains (even discretization, $n_{sup} = 4$) meet the criterion in the center of the domain.

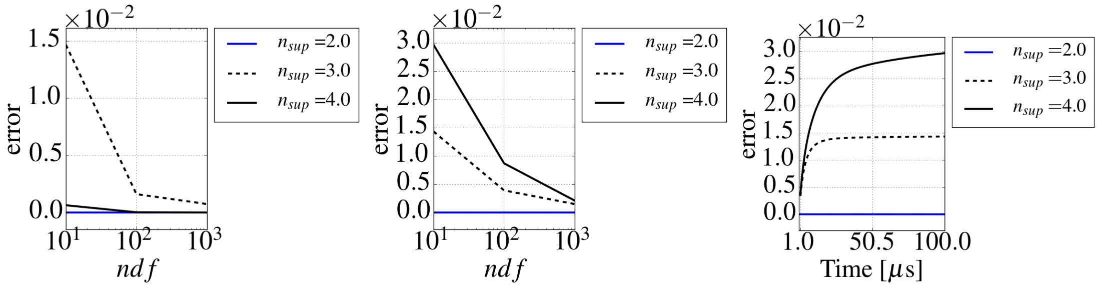

Figure 9.6. Error in displaying a constant gradient on even (left) and irregular (center) discretizations with respect to the size of support domains. The error on an irregular discretization is higher but approaching an assymptote (right) even for the coarsest discretization with 10 material points.

free methods. Starting point to derive this constraint is the weak form of the static momentum equation with tractions on the Neumann boundary:

$$\int_v \operatorname{grad} \boldsymbol{\eta} : \boldsymbol{\sigma} \, \mathrm{d}v = \int_a \mathbf{t} \cdot \boldsymbol{\eta} \, \mathrm{d}a \tag{9.11}$$

For a stress state with constant principal stresses $\sigma = \sigma_{11} = \sigma_{22} = \sigma_{33}$ and no shear stresses, the Cauchy stress tensor can be expressed as the product of a scalar σ multiplied with the unity tensor, i.e $\boldsymbol{\sigma} = \sigma \, \mathbf{1}$. Implementing this expression into the above weak form while additionally making use of the Cauchy theorem and the identity $\operatorname{grad} \boldsymbol{\eta} : \mathbf{1} = \operatorname{div} \boldsymbol{\eta}$ yields to:

$$\int_v \operatorname{div} \boldsymbol{\eta} \, \mathrm{d}v = \int_a \mathbf{n} \cdot \boldsymbol{\eta} \, \mathrm{d}a \tag{9.12}$$

Note that for the considered stress state, the equilibrium equation becomes independent of the stress magnitude. In the discrete form of (9.12), the left hand side can be identified as the color gradient (9.9), which is the nodal volume gradient. It follows then directly that the color gradient must be zero inside the domain where no traction is applied. On the boundary, it must point into the direction of the outward normal and its magnitude must equal the

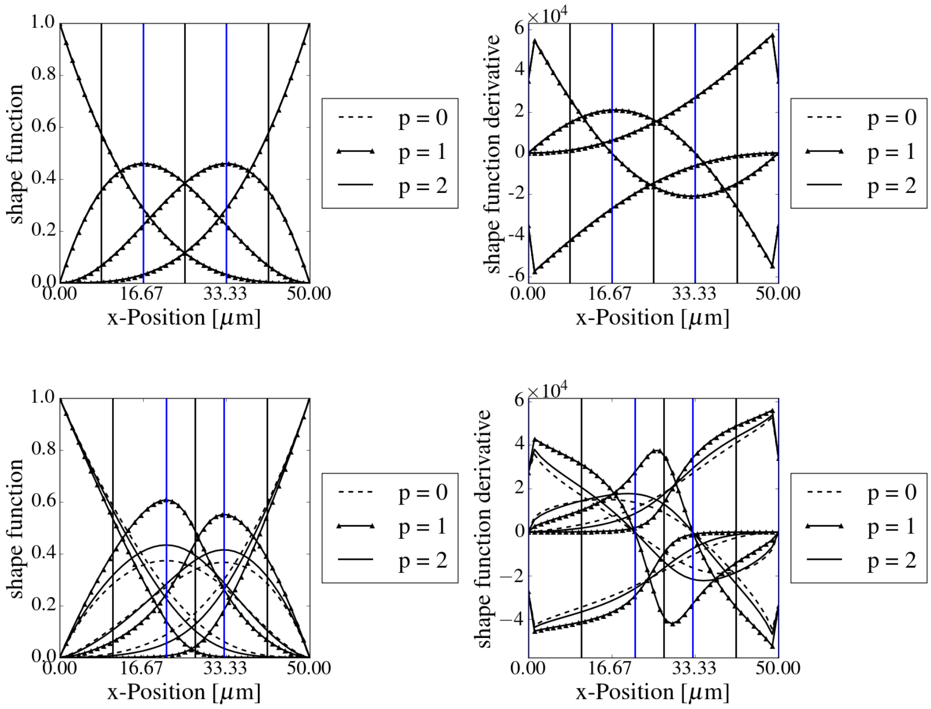

Figure 9.7. 1D LME shape functions (left) and derivatives (right) with $n_{sup} = 4$ using a regular (top) and an irregular nodal spacing (bottom).

surface increment:

$$\sum_{p}^{N_I^{inf}} \frac{\partial N_I\left(\mathbf{x}_p\right)}{\partial \mathbf{x}_p} v_p = \begin{cases} \mathbf{0} & \forall \, \text{inner nodes} \\ \mathbf{n} \, \mathrm{d}a & \forall \, \text{outer nodes} \end{cases} \tag{9.13}$$

Therefore, for an accurate method, a cutoff criterion as proposed in (9.10) is not necessary. Since in OTM the color gradient does not vanish inside the continuum, the divergence of stress and heat flux cannot be solved correctly, i.e. a numerical error is introduced. The impact of this error is further investigated in one dimensional examples. Special focus lays on the influence of the shape and size of support domains as well as on the LME shape functions.

Error analysis

The accuracy of OTM computations in displaying a constant thermal gradient is evaluated by solving the one dimensional energy equation with an explicit time integration scheme (6.9). A linear temperature profile from 2000 K to 0 K is imposed as initial condition onto a bar of 50 μm length. The edges of the bar are subject to Dirichlet boundary conditions. Following ZIENKIEWICZ ET AL. (2013), the relative error ε_p at a material point is obtained from:

$$\varepsilon_p = \frac{\left[\sum_p \left(\theta_p - \hat{\theta}\left(\mathbf{x}_p\right)\right)^2 v_p\right]^{\frac{1}{2}}}{\left[\sum_p \hat{\theta}^2\left(\mathbf{x}_p\right) v_p\right]^{\frac{1}{2}}} \tag{9.14}$$

Here, $\hat{\theta}$ is the analytical solution which in the present case is equal to the initial temperature distribution. The temperature at the material point θ_p is interpolated from the nodal values. The accuracy is checked on even and on irregular discretizations with varying refinement. The irregular discretizations were obtained by randomly placing nodes inside the domain. Only restriction was that the minimal distance between two nodes must be 0.6 times the nodal spacing of the corresponding even discretization. From figure 9.5 it becomes clear that the OTM can only correctly meet the integration constraint (9.13) if the support domain is symmetric, i.e. for $n_{sup} = 4$ regularly spaced nodes per support domain. For irregular discretizations, errors are introduced which remain acceptable in the present test case. Figure 9.6 illustrates that the error significantly decreases with increasing spatial refinement. Also, with time evolving it asymptotically approaches an upper bound even on a very coarse irregular discretization.

LME shape functions

In figure 9.7, the LME shape functions are plotted on regular and irregular 1D discretizations for a support domain size of $n_{sup} = 4$. If the nodal spacing is regular, the shape functions resemble NURBS functions, while for irregular discretizations, they become highly nonlinear. The non-linearity of the shape functions suggests that the violation of the integration constraint is related to insufficient integration. Clearly, the functions can not be properly integrated with only one integration point as it is the case in OTM. However, CHEN ET AL. (2001) have shown in a comparison of five point Gauss and nodal integration schemes that the simple insertion of additional integration points does not guarantee the fulfillment of the integration constraint. Therefore, the error related to the violation of the integration constraint of CHEN ET AL. (2001) remains also in the stabilized OTM according to WEISSENFELS & WRIGGERS (2018).

In the original publication of LI ET AL. (2010), a nodal shifting algorithm has been used to overcome inaccuracies related to asymmetric support domains. To the knowledge of the author, details on the shifting algorithm have not been published. The use of nodal shifting is controversial and has not been examined in this work.

Remark: *In an attempt to increase the accuracy of OTM computations, linearity of the shape functions has been enforced via the locality parameter $\beta = \gamma/h$. Therefore, the characteristic nodal spacing h_I has been computed for each node individually as a function of its distance to the material point. While the approach yields a significant improvement in 1D, a generalization to higher dimensions is not possible. This is because in 3D the closest nodes are not necessarily those who form a convex hull around a material point. Also, it would be more straightforward to directly remove nodes whose influence is known to be negligible in the search algorithm. Hence, the approach was abandoned and is not further discussed here.*

In summary, it has been shown that the OTM suffers from numerical errors due to the violation of the integration constraint (9.13) suggested by CHEN ET AL. (2001). The consequence of this deficiency depends on the physics that are to be solved. As illustrated in this section, the error in displaying a constant thermal gradient becomes negligible for sufficiently fine spatial discretizations. For plasticity, WEISSENFELS & WRIGGERS (2018) have obtained satisfactory results for the Taylor-anvil benchmark. In surface tension, the error is prohibitive because the region in which surface tension is allowed to act cannot accurately be captured. More generally, effects involving boundary conditions on the free surface can currently not be displayed with the OTM.

Chapter 10

Conclusion and Outlook

Interest in Additive Manufacturing (AM) has grown significantly in recent years. Selective Laser Melting (SLM) is an innovative AM process where a powder bed is locally melted with a laser layer by layer. SLM enables the production of complex, individualized metal parts. Compared to traditional techniques like milling or casting, SLM is a relatively new process. A current research goal is to increase production rates and efficiency. Another aspect is to enable the processability of new powder materials. Since experiments are time consuming and expensive, numerical simulation is a promising tool to support research and development in the field.

In this work, a continuum theory for finite deformation phase change problems has been presented in which all physical phenomena relevant for the SLM process can be incorporated. The phase change approach based on the fading memory of the isochoric deformation gradient has already been published in earlier work (WESSELS ET AL., 2018). In the present thesis, the solid phase model has been extended about inelastic contributions to account for residual stress formation. The combination of large deformations and free surface effects which are typical for the SLM process is hard to solve with traditional mesh based methods. Therefore, for the numerical solution of the theoretical model, meshfree methods seem promising. Particularly, the novel Optimal Transportation Meshfree Method (OTM) was chosen. LI ET AL. (2010) promoted the OTM as a versatile tool for both solid and fluid dynamics. Numerical results showcase that the OTM can qualitatively represent the major effects of metal powder melting and fusion.

It could be demonstrated that the heat source model has a large effect on the temperature evolution and the vaporization behavior. Two different models, namely a volumetric heat source and a ray tracing algorithm have been compared. For this purpose, a novel coupling scheme for meshfree methods and ray tracing was employed. The coupling algorithm has recently been proposed in WESSELS ET AL. (2019). While it has been explicitly described for the OTM, it is also easy to adopt in combination with other methods. In order to avoid a computationally expensive surface triangulation, the rays themselves identify the free surface. Convergence is ensured with a non-local formulation of ray absorption, i.e. a parameter is introduced which controls the locality of ray absorption. This parameter has a physical interpretation: It represents the penetration of laser radiation into the part. The reflection of rays depends on the incident angle and is object to the Fresnel equations.

Although promising results were presented, it was also found that the OTM exhibits se-

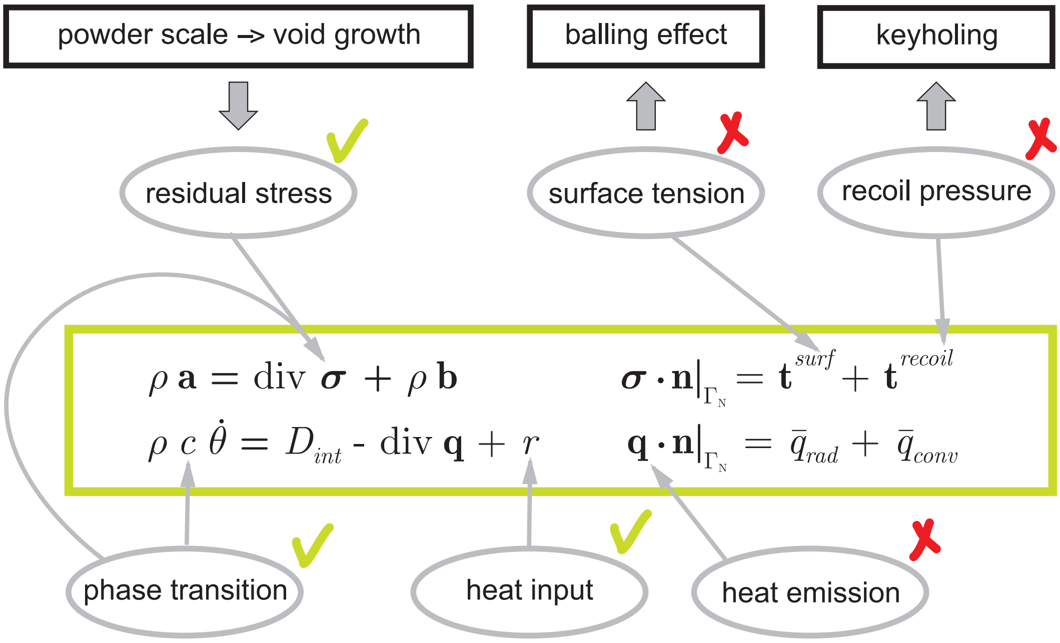
powder scale -> void growth
balling effect
keyholing
residual stress
surface tension
recoil pressure
$\rho\,\mathbf{a} = \operatorname{div}\boldsymbol{\sigma} + \rho\,\mathbf{b}$
$\boldsymbol{\sigma}\cdot\mathbf{n}|_{\Gamma_N} = \mathbf{t}^{surf} + \mathbf{t}^{recoil}$
$\rho\,c\,\dot{\theta} = D_{int}$ - div $\mathbf{q} + r$
$\mathbf{q}\cdot\mathbf{n}|_{\Gamma_N} = \bar{q}_{rad} + \bar{q}_{conv}$
phase transition
heat input
heat emission

Figure 10.1. Overview of physics in the SLM process that currently can and cannot be accurately described with the OTM. Generally, the imposition of Neumann boundary conditions is problematic due to unreliable surface recognition. The reason for this deficiency is the violation of the integration constraint (9.13) introduced by CHEN ET AL. (2001).

vere limitations. WEISSENFELS & WRIGGERS (2018) have shown that the original OTM suffers from under-integration. This problem could be alleviated by introducing a stabilizing term based on a penalty regularization. Another problem of the OTM is related to the use of Local Maximum Entropy (LME) shape functions (ARROYO & ORTIZ, 2006). The convergence of the local Newton-Raphson algorithm in which the LME's are computed is sensitive to the particle distribution and might fail on arbitrary point clouds. This problem has been circumvented by iteratively increasing the enlarge factor which controls the size of support domains. Additionally, it was found that the implicit solution scheme first presented in WESSELS ET AL. (2018) increases the stability of the OTM compared to the original explicit algorithm. Finally, the most critical limitation of the OTM is that it fails to meet the integration constraint postulated in CHEN ET AL. (2001). This criterion requires the norm of the nodal volume gradient to vanish inside the geometry and to equal the surface increment on the boundary. If the criterion is violated, the divergence of a constant field cannot be displayed correctly. While it could be shown that the OTM converges nevertheless in 1D heat conduction (chapter 9) and in 3D finite elasto-plasticity simulations (WEISSENFELS & WRIGGERS, 2018), the violation of the integration constraint causes severe problems for the imposition of Neumann boundary conditions on moving surfaces. In meshfree methods that fulfill the integration constraint, the free surface is conveniently identified from the volume gradient. Since the OTM fails to meet the integration constraint, this surface recognition technique is not reliable in OTM computations and surface tension forces can not accurately be imposed. The same applies to other boundary conditions like recoil pressure and heat emission through radiation and convection. An overview of the physics in SLM that cur-

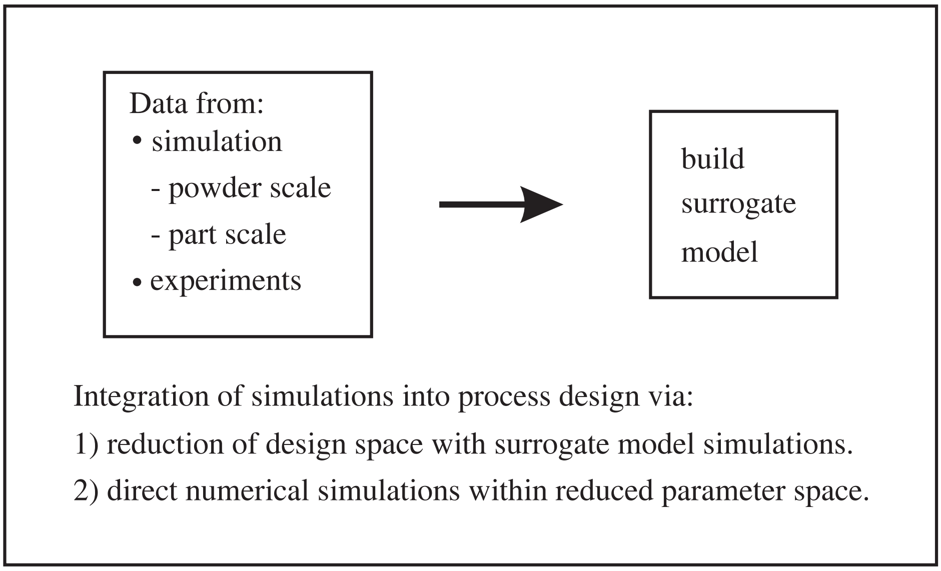
Data from:
• simulation
- powder scale
- part scale
• experiments
build surrogate model
Integration of simulations into process design via:
1) reduction of design space with surrogate model simulations.
2) direct numerical simulations within reduced parameter space.

Figure 10.2. Application scenario of powder scale process simulation in the product and process development for SLM.

rently can and cannot be described with OTM is shown in figure 10.1.

The problems related to the surface recognition could be remedied with two alternative approaches: First, by implementing alternative surface recognition algorithms such as the alpha shape technique employed in the Particle Finite Element Method (PFEM) (Oñate et al., 2004). However, the additional computational effort is not deemed acceptable in view of the fact that an improved surface recognition would not increase the accuracy of the spatial derivative operators, which is at the core of the problem. A second possibility would be to develop a nodal shifting algorithm as was briefly mentioned in the original work on OTM (Li et al., 2010). However, to the knowledge of the author, details on a shifting algorithm for the OTM have not been published. Additionally, the use of nodal shifting is controversial because the particles are moved differently from the converged solution. Therefore, nodal shifting has not been considered in this work.

The development of reliable meshfree methods that provide high accuracy in both fluid and solid mechanics is a key challenge for future research activities. A possible alternative for the solution of the proposed continuum framework is for instance the stabilized conforming nodal integration scheme for meshfree Galerkin methods suggested by Chen et al. (2001). The stabilization employed therein is based on a Voronoi tessellation. Another alternative are meshfree methods making use of a background grid, e.g. the Material Point or the Element Free Galerkin method. Also the aforementioned PFEM is a promising option, since it has been applied to a variety of fluid dynamics and fluid-structure-interaction problems (Oñate et al., 2004).

Recently, powerful meshfree powder scale SLM simulations with Smoothed Particle Hydrodynamics (SPH) have been presented in Fürstenau et al. (2019b). In the SPH framework, the solid mechanics were neglected. While the energy equation was solved in the entire domain, the momentum equation was only considered inside the melt pool. Since residual stress formation is mainly governed by part scale parameters such as laser scanning pattern and build height, neglecting the solid mechanics can be considered a reasonable assumption on the powder scale.

So far, only the suitability of different numerical methods for SLM powder scale simulations has been discussed. A general question to be answered is still open: How to make powder scale SLM computations a useful tool for designers? One critical limitation for a practical implementation of powder scale simulations into the design workflow is the required computational time. The SPH approach of FÜRSTENAU ET AL. (2019b) is an important step towards industrial applicability. However, the conceptual division of the SLM process into part and powder scale is a barrier remaining. Ultimately, decision making should be supported by all kind of available information, that is simulation as well as experimental data. Therefore, a link between the different sources of information must be found. As has been discussed in section 2.2, such a link could be established with surrogate models. Surrogate models are especially useful for parameter studies as presented in chapter 8, where the influence of laser power has been evaluated by means of only three output parameters (gap indicator, consolidation time, maximum temperature). A reliable powder scale simulation tool could therefore be used in a two step process as sketched in figure 10.2: First, to inform a surrogate model which can then be used to reduce the design space. Afterwards, a limited number of detailed, direct numerical simulations can be performed for visualization and further investigations.

Appendix A

Free energy potential

In chapter 4, the temperature dependency of material parameters was neglected in the derivation of the thermal contribution (4.12) to the free energy potential (4.14). For completeness, the exact derivation of the elastic volumetric free energy potential $\psi_{vol,e}$ (4.9) is given by:

$$\begin{aligned}
\frac{\partial \psi_{vol,e}}{\partial \theta} &= \frac{\partial}{\partial \theta}\left(\frac{1}{2} K\left(\theta\right)\left(\ln J_e\right)^2\right) \\
&= \frac{1}{2}\frac{\partial K}{\partial \theta} - K\left(\ln J_e\right)\frac{\partial}{\partial \theta}\left(3\alpha_{th}\left(\theta-\theta_0\right)\right) \\
&= \frac{1}{2}\frac{\partial K}{\partial \theta}\left(\ln J_e\right)^2 - K\left(\ln J_e\right)\left(3\frac{\partial \alpha_{th}}{\partial \theta}\left(\theta-\theta_0\right)+3\alpha_{th}\right)
\end{aligned} \tag{A.1}$$

Consequently, for the second derivative it holds:

$$\begin{aligned}
\frac{\partial^2 \psi_{vol,e}}{\partial \theta^2} &= \frac{\partial}{\partial \theta}\left\{\frac{1}{2}\frac{\partial K}{\partial \theta}\left(\ln J_e\right)^2 - K\left(\ln J_e\right)\left(3\frac{\partial \alpha_{th}}{\partial \theta}\left(\theta-\theta_0\right)+3\alpha_{th}\right)\right\} \\
&= \frac{1}{2}\frac{\partial^2 K}{\partial \theta^2}\left(\ln J_e\right)^2 - \frac{\partial K}{\partial \theta}\left(\ln J_e\right)\left(3\frac{\partial \alpha_{th}}{\partial \theta}\left(\theta-\theta_0\right)+3\alpha_{th}\right) \\
&\quad - \frac{\partial K}{\partial \theta}\left[\left(\ln J_e\right)\left(3\frac{\partial \alpha_{th}}{\partial \theta}\left(\theta-\theta_0\right)+3\alpha_{th}\right)\right] + K\left(3\frac{\partial \alpha_{th}}{\partial \theta}\left(\theta-\theta_0\right)+3\alpha_{th}\right)^2 \\
&\quad - K\left(\ln J_e\right)\left(3\frac{\partial^2 \alpha_{th}}{\partial \theta^2}\left(\theta-\theta_0\right)+6\alpha_{th}\right)
\end{aligned} \tag{A.2}$$

The exact thermal free energy can now be obtained by rearranging the definition of the heat capacity (4.10) and integrating twice over temperature:

$$T\left(\theta\right) = -\int_{\theta_0}^{\theta}\int_{\theta_0}^{\theta}\frac{\partial^2 \psi_{vol,e}}{\partial \theta^2}\,\mathrm{d}\theta^2 - \int_{\theta_0}^{\theta}\int_{\theta_0}^{\theta}\frac{\rho_0}{\theta}\left(c\left(\theta\right)+L_\theta\right)\,\mathrm{d}\theta^2 \tag{A.3}$$

The entropy (4.18) has been identified as the negative derivative of the free energy with respect to temperature. The temperature dependency of material parameters has again been neglected. For completeness, the exact derivation of the simplified potential (4.14) with respect to temperature is given by:

$$s = -\frac{\partial \psi}{\partial \theta} = \frac{3\alpha K}{\rho_0} \ln J + (c + L_\theta) \ln \frac{\theta}{\theta_0} - \frac{1}{2}\frac{\partial H_\alpha}{\partial \theta}\alpha^2 \underline{- \frac{1}{2}\frac{\partial K}{\partial \theta} (\ln J)^2}$$
$$- \frac{1}{2}\frac{\partial \mu}{\partial \theta} (I_{\bar{\mathbf{b}}_e} - 3) - 3 \left[\frac{\partial \alpha}{\partial \theta} K + \alpha \frac{\partial K}{\partial \theta}\right] (\ln J)\, \theta - \rho_0 \frac{\partial (c + L_\theta)}{\partial \theta} \left(\theta \ln \frac{\theta}{\theta_0} - (\theta - \theta_0)\right) \tag{A.4}$$

Appendix B

Linearization

The local return mapping algorithm (section 6.2.2) and the computation routine for the LME shape functions (section 6.4) have been generated with the software *AceGen* (section 6.5). In the global Newton-Raphson algorithm, the consistent linearization of internal forces and heat conduction matrix at the material point level has also been obtained with *AceGen*. The remaining terms were linearized manually. These linearizations are briefly summarized here. Details can be found in the work of MIEHE (1988).

Material parameter
The material parameters are expressed as a function of the temperature at the previous time step. Therefore, their linearization is neglected.

Mass and heat capacitance matrix $\mathbf{M}$ and $\mathbf{C}$
As discussed in section 6.2, the shape functions are computed as functions of the previous support domains. As a consequence, the linearization of the mass matrix $\mathbf{M}$ (6.14) is zero. Since the material parameters are taken as constant within a time step, also the linearization of the heat capacitance matrix $\mathbf{C}$ (6.4) vanishes.

Mechanical load vector $\mathbf{P}$
The linearization of gravitational forces is zero, since gravity acceleration $\hat{\mathbf{b}}$ and mass $m = \rho v$ are constant. The surface tension force is only computed once within each time step. Therefore, its linearization is neglected and $\Delta\mathbf{P}$ with $\mathbf{P}$ the load vector (6.16) is zero. Note that the smoothing (6.19) of the surface tension force $\mathbf{f}^{CSF}$ is an expensive operation and makes a consistent linearization cumbersome. Although it is understood that optimal convergence cannot be reached with this simplification, the algorithm converged within three to maximum five global iterations which is deemed acceptable.

Termal load vector $\mathbf{Q}$
For a volumetric heat source, the intensity function is updated within each iteration step, but it is not linearized. The linearization of the heat input vector $\mathbf{Q}$ (6.6) involves the linearization of the volume. It is given by

$$\Delta\,\mathrm{d}v = \Delta\left(J\,\mathrm{d}V\right) = \mathrm{div}\,\Delta\mathbf{u} \tag{B.1}$$

In combination with ray tracing, a linearization of $\mathbf{Q}$ is not necessary since each ray is assigned a discrete energy portion. Reflection is only computed once within a time step.

Acceleration $\mathbf{a}$ and temperature rate $\dot{\theta}$
The linearization of the acceleration $\mathbf{a}$ and the temperature rate $\dot{\theta}$ follow from the integration rules (6.20):

$$\Delta\dot{\theta}_{I\,n+1} = (\Delta t)^{-1}\,\Delta\theta_{I\,n+1} \qquad \Delta\mathbf{a}_{I\,n+1} = \alpha_1\Delta\mathbf{u}_{I\,n+1} \tag{B.2}$$

Rigid mechanical and thermal contact $\mathrm{R}^{con}_{\mathbf{u}}$ and $\mathrm{R}^{con}_{\theta}$
For the linearization of thermal contact (6.49), only the temperature must be linearized. Analogously, in the penalty force (6.47) of the mechanical contact formulation, only the current position is linearized as $\Delta\mathbf{x}_{I\,n+1} = \Delta\mathbf{u}_{I\,n+1}$.

Penalty regularization $\mathbf{E}$
The stabilizing penalty regularization $\mathbf{E}$ (6.35) is based on the discrepancy $\mathbf{e}_{I\,p\,n+1}$ (6.34). The latter is a function of the current nodal displacements $\mathbf{u}_{I\,n+1}$. Linearization yields:

$$\Delta\mathbf{E}^{k+1}_{I\,n+1} = \varepsilon\frac{N_{I\,p\,n}}{||\mathrm{d}\mathbf{x}_{I\,p\,n}||}\Delta\mathbf{e}_{I\,p\,n+1} = \varepsilon\frac{N_{I\,p\,n}}{||\mathrm{d}\mathbf{x}_{I\,p\,n}||}\left(\Delta\mathrm{d}\mathbf{x}^{k+1}_{I\,p\,n+1} - \Delta\left(\Delta\mathbf{F}^{k+1}_{p\,n+1}\right)\mathrm{d}\mathbf{x}_{I\,p\,n}\right) \tag{B.3}$$

From the update of material point coordinates $\mathbf{x}_p$ (6.23), the linearization of the distance vector $\mathrm{d}\mathbf{x}_{I\,p}$ (6.33) becomes:

$$\Delta\mathrm{d}\mathbf{x}^{k+1}_{I\,p\,n+1} = \Delta\mathbf{u}^{k+1}_{I\,n+1} - \sum_{J}^{N^{sup}_{p\,n}} N_J\left(\mathbf{x}_{p\,n}\right)\Delta\mathbf{u}^{k+1}_{J\,n+1} \tag{B.4}$$

The incremental deformation gradient has been introduced in (6.25). It maps the material point position from the previous to the current time step, whereby the previous time step is regarded as the reference configuration. The linearization of $\Delta\mathbf{F}$ yields:

$$\begin{aligned}\Delta\left(\Delta\mathbf{F}^{k+1}_{p\,n+1}\right) &= \Delta\left(\frac{\partial\mathbf{x}^{k+1}_{p\,n+1}}{\partial\mathbf{x}_{p\,n}}\right) = \mathrm{Grad}\left(\mathbf{x}^{k+1}_{p\,n+1}\right) = \mathrm{Grad}\left(\sum_{J}^{N^{sup}_{p\,n}} N_J\left(\mathbf{x}_{p\,n}\right)\Delta\mathbf{u}^{k+1}_{J\,n+1}\right)\\ &= \sum_{J}^{N^{sup}_{p\,n}}\mathrm{Grad}^T\left(N_J\right)\Delta\mathbf{u}^{k+1}_{J\,n+1}\end{aligned} \tag{B.5}$$

Appendix C

Heat Source Modeling

C.1 Gusarov Model

The first derivative of the dimensionless laser energy density q with respect to the dimensionless coordinate ξ in the intensity distribution (5.11) is given by

$$\begin{aligned} -\frac{\partial q}{\partial \xi} = \frac{\rho_h\, a}{\left(4\rho_h - 3\right) C} \Big\{ & \left(1 - \rho_h^2\right) e^{-\lambda} \left[\left(2a^2 - 2a\right) e^{-2a\xi} + \left(2a^2 + 2a\right) e^{2a\xi}\right] \\ & - \left(3 + \rho_h e^{-2\lambda}\right) \left[\left(-2a^2\rho_h - 2a^2 + 2a\rho_h - 2a\right) e^{2a(\lambda-\xi)} \right. \\ & \left. + \left(-2a^2\rho_h - 2a^2 - 2a\rho_h + 2a\right) e^{2a(\xi-\lambda)}\right] \Big\} - \frac{3}{4\rho_h - 3} \left(\rho_h - 1\right) e^{-2\lambda-\xi} \left(e^{2\lambda} + \rho_h e^{2\xi}\right) \end{aligned} \tag{C.1}$$

with

$$\begin{aligned} C &= (1-a)\left[1 - a - \rho\,(1+a)\right] e^{-2a\lambda} - (1+a)\left[1 + a - \rho\,(1-a)\right] e^{2a\lambda} \\ a &= \sqrt{1-\rho_h} \end{aligned} \tag{C.2}$$

Here, ρ_h is the hemispherical reflectivity and λ the optical thickness (5.11). For details on the theoretical background see GUSAROV ET AL. (2009).

C.2 Ray Tracing

The ray absorption is validated by comparison with an analytical solution. The power fraction ζ absorbed by a hemisphere is computed from the following surface integral:

$$\zeta = \int_0^R \int_0^{2\pi r} \left(1 - R_r\left(\theta^{in}\right)\right) I_{rad}\left(r\right)\, \mathrm{d}\phi\, \mathrm{d}r \tag{C.3}$$

With the radial intensity function from (5.5) and the substitutions $r = R \sin\left(\theta^{in}\right)$ and $\mathrm{dr} = \mathrm{R}\cos\left(\theta^{\mathrm{in}}\right)$ one obtains:

$$\zeta = \int_0^{\frac{\pi}{2}} \left(1 - R_r\left(\theta^{in}\right)\right) 4 \frac{\sin\left(\theta^{in}\right)\cos\left(\theta^{in}\right)}{1 - e^{-2}}\, \mathrm{d}\theta^{\mathrm{in}} \tag{C.4}$$

The definite integral has been evaluated with the software Mathematica using $R_r\left(\theta^{in}\right)$ from (7.12) with the parameters $\hat{\mu} = 1.0$ and $\hat{n} = 2.4$. The result $(\zeta = 81.3\%)$ is in very good agreement with the coupled ray tracing OTM algorithm $(\zeta = 82\%)$ from section 7.4.

Appendix D

Particle Fusion

D.1 Influence of Spatial and Temporal Discretization

Note that the gap indicator slightly depends on the spatial discretization. When fewer discretization points are used, the fusion gap does not approach zero as close as in figure 8.6. Gap indicator, consolidation time and maximum temperature as functions of laser power with heat transfer coefficient $\alpha_{powder} = 10^3$ W/(m^{2}K) on a coarse discretization (1127 nodes, 4728 material points) are compared to a finer discretization (1691 nodes, 7441 material points) in figure D.1. Gap indicator and consolidation time as functions of heat transfer coefficient are compared in figure D.2 for coarse and fine spatial discretizations. Consolidation time and maximum temperature are hardly affected by the investigated spatial discretizations. In order to make the gap indicator independent of spatial discretization it could be smoothed by weighting the material volume within a small neighborhood around the box in which the gap is computed rather than setting fixed boundaries.

The results are also insensitive to a refinement of the time step. In the parameter study, a time step size of $\Delta t = 10^{-6}$ s was used. The results obtained on a coarse spatial discretization consisting of 1127 nodes and 4728 material points with a laser power of 19 W have been compared to those obtained with a smaller time step of $\Delta t = 10^{-7}$ s. As summarized in table D.1, the difference in consolidation time and maximum temperature is 1.11% and 0.05%, respectively. This is deemed acceptable to justify the use of the larger time step.

	$\Delta t = 10^{-7}$ s	$\Delta t = 10^{-6}$ s	Deviation
gap indicator	0.825499	0.812675	1.55%
consolidation time	3.7396 μs	3.781 μs	1.11%
maximum temperature	3075.97 K	3077.63 K	0.05%

Table D.1. Evaluation of time step sensitivity on the numerical results. The laser power is $P_{laser} = 19$ W. The remaining simulation parameters are as specified in section 8.3.

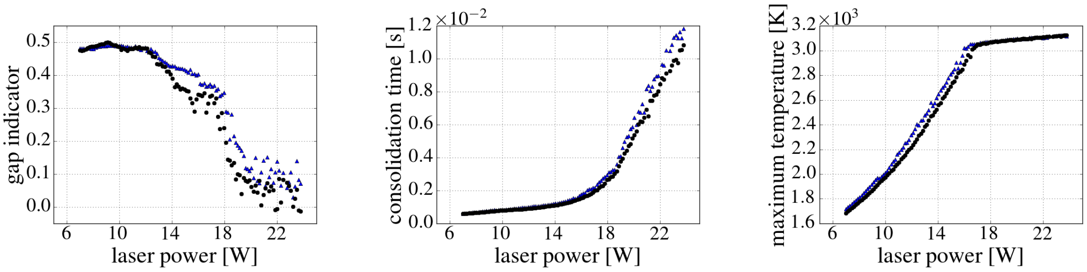

Figure D.1. Gap indicator, consolidation time and maximum temperature for $\alpha = 10^3$ W/(m^{2}K) as functions of laser power. Blue triangles refer to a coarse, black dots to a fine spatial discretization. The results of the fine discretization are identical to the ones presented in figure 8.6.

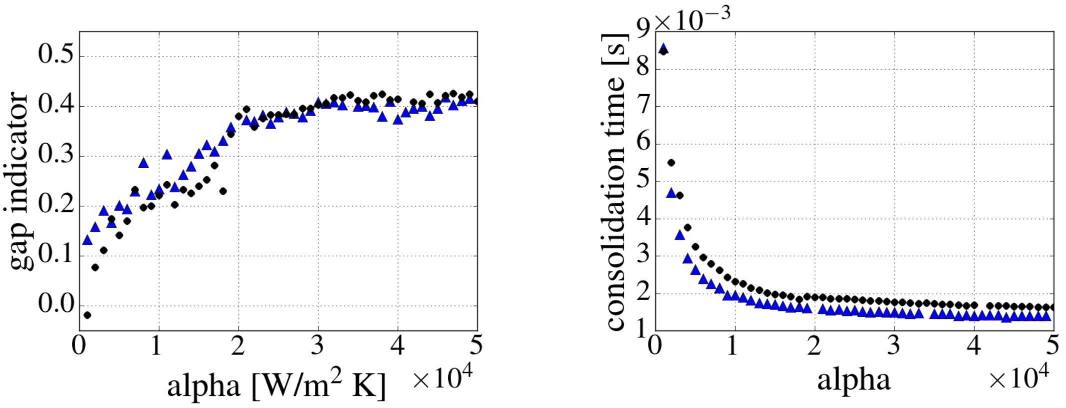

Figure D.2. Gap indicator and consolidation time as functions of heat transfer coefficient at a laser power of 22 W. Blue triangles refer to a coarse, black dots to a fine spatial discretization. The results of the fine discretization are identical to the ones presented in figure 8.4.

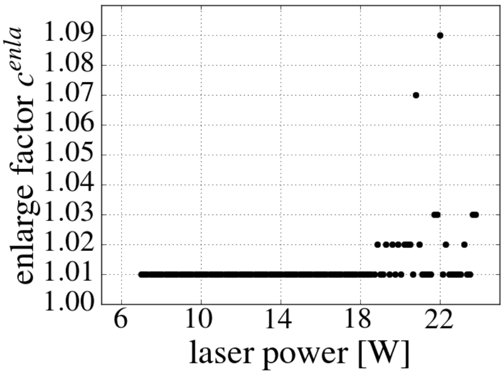

Figure D.3. Enlarge factor c^{enla} as a function of laser power. The plotted values are necessary for the computations with heat transfer coefficient α_{powder} on a fine spatial discretization shown in figures 8.6 and D.1. Initially, the enlarge factor c^{enla} is equal to 1.01. If a simulation fails, c^{enla} is increased about 0.01 and the simulation is restarted. This procedure is repeated until a stable result is obtained.

D.2 Stability of LME Shape Functions

As was discussed in section 8.3, OTM computations tend to fail due to convergence problems in the LME shape function routine. This becomes especially pronounced at higher laser powers, where large deformations in the liquid domain are expected. The stability of the LME Newton-Raphson algorithm is closely related to a numerical parameter, namely the enlarge factor c^{enla} which controls the search radius extension factor α^{ext} (6.36). This parameter determines the size of support domains and is part of the search algorithm. Search algorithm and LME shape functions were introduced in chapter 6. In this work, the instability is addressed by restarting a failed simulation with a slightly increased value of c^{enla}. The enlarge factor corresponding to the investigation of cooling conditions presented in figures 8.6 and D.1 is plotted in figure D.3. Up to nine attempts were necessary to obtain a stable computation for a given laser power. Limitations of the OTM are discussed in chapter 9.

Bibliography

AGARWALA M., BOURELL D., BEAMAN J., MARCUS H. ET AL. Direct selective laser sintering of metals. *Rapid Prototyping Journal*, 1 (1995) (1): 26–36.

AGELET DE SARACIBAR C., CERVERA M. & CHIUMENTI M. On the formulation of coupled thermoplastic problems with phase-change. *International Journal of Plasticity*, 15 (1999) (1): 1–34.

AMMER R., MARKL M., LJUNGBLAD U., KÖRNER C. ET AL. Simulating fast electron beam melting with a parallel thermal free surface lattice Boltzmann method. *Computers & Mathematics with Applications*, 67 (2014) (2): 318–330.

ANISIMOV S.I. & KHOKHLOV V.A. *Instabilities in laser-matter interaction*. CRC Press, Boca Raton, Florida, 1995.

ARROYO M. & ORTIZ M. Local maximum-entropy approximation schemes: A seamless bridge between finite elements and meshfree methods. *International Journal for Numerical Methods in Engineering*, 65 (2006) (13): 2167–2202.

BELYTSCHKO T., GUO Y., K. LIU W. & P. XIAO S. A unified stability analysis of meshless particle methods. *International Journal for Numerical Methods in Engineering*, 48 (2000) (9): 1359–1400.

BELYTSCHKO T., KRONGAUZ Y., DOLBOW J. & GERLACH C. On the completeness of meshfree particle methods. *International Journal for Numerical Methods in Engineering*, 43 (1998) (5): 785–819.

BELYTSCHKO T., LU Y.Y. & GU L. Element-free Galerkin methods. *International Journal for Numerical Methods in Engineering*, 37 (1994) (2): 229–256.

BESSA M.A., BOSTANABAD R., LIU Z., HU A. ET AL. A framework for data-driven analysis of materials under uncertainty: Countering the curse of dimensionality. *Computer Methods in Applied Mechanics and Engineering*, 320 (2017): 633–667.

BESSA M.A., FOSTER J.T., BELYTSCHKO T. & LIU W.K. A meshfree unification: Reproducing kernel peridynamics. *Computational Mechanics*, 53 (2014) (6): 1251–1264.

BOBARU F. *Handbook of peridynamic modeling*. CRC, Boca Raton, Florida, 2017.

BODE T. *Simulation of the Particle Distribution and Resulting Laser Processing of Selective Laser Melting Processes*. Master thesis, Leibniz University, Hannover (2017).

BONACINA C., COMINI G., FASANO A. & PRIMICERIO M. Numerical solution of phase-change problems. *International Journal of Heat and Mass Transfer*, 16 (1973) (10): 1825–1832.

BRACKBILL J.U., KOTHE D.B. & ZEMACH C. A continuum method for modeling surface tension. *Journal of Computational Physics*, 100 (1992): 335–354.

CAPRIO L., DEMIR A.G. & PREVITALI B. Comparative study between cw and pw emissions in selective laser melting. *Journal of Laser Applications*, 30 (2018) (3): 032 305.

CERVERA M., AGELET DE SARACIBAR C. & CHIUMENTI M. Thermo-mechanical analysis of industrial solidification processes. *International Journal for Numerical Methods in Engineering*, 46 (1999) (9): 1575–1591.

CHAWLA T.C., GRAFF D.L., BORG R.C., BORDNER G.L. ET AL. Thermophysical properties of mixed oxide fuel and stainless steel type 316 for use in transition phase analysis. *Nuclear Engineering and Design*, 67 (1981) (1): 57–74.

CHEN J.S., WU C.T., YOON S. & YOU Y. A stabilized conforming nodal integration for Galerkin mesh-free methods. *International Journal for Numerical Methods in Engineering*, 50 (2001) (2): 435–466.

CHEN L., LEE J.H. & CHEN C.F. On the modeling of surface tension and its applications by the generalized interpolation material point method. *Computer Modeling in Engineering and Sciences*, 86 (2012) (3): 199–223.

CHEN S.H. *Computational geomechanics and hydraulic structures*. Springer tracts in civil engineering. Springer, Singapore, 2019.

CHIUMENTI M. *Constitutive Modeling and Numerical Analysis of Thermo-Mechanical Phase Change Systems*. Dissertation, UPC, Barcelona (1998).

CIARLET P.G. & RAVIART P.A. Maximum principle and uniform convergence for the finite element method. *Computer Methods in Applied Mechanics and Engineering*, 2 (1973) (1): 17–31.

DE SOUZA NETO E.A., PERIĆ D. & OWEN D.R.J. *Computational methods for plasticity: Theory and applications*. Wiley, Chichester, West Sussex, UK, 2008.

DHATT G. & TOUZOT G. *The finite element method displayed*. A Wiley-Interscience publication. Wiley, Chichester [etc.], 1985, reprinted edition.

DIN 8580. Fertigungsverfahren - Begriffe, Einteilung (2003).

DIN EN ISO 52900. Additive Fertigung - Grundlagen - Terminologie (2017).

DYKA C.T. & INGEL R.P. Addressing tension instability in SPH methods. *Interim Report Naval Research Lab., Washington, D.C.*, (1994).

EAGAR T.W. & TSAI N.S. Temperature fields produced by traveling distributed heat sources. *Welding Journal*, 62 (1983) (12): 346–355.

EOS GMBH. Help is fast at hand thanks to additive manufacturing: Alphaform produces a hip replacement designed by instrumentaria. *https://www.eos.info/press/case_study/additive_manufactured_hip_implant*, (2015).

FERZIGER J.H. & PERIĆ M. *Computational methods for fluid dynamics*. Springer, Berlin and New York, 2002, 3rd, revised edition.

FRANCOIS M.M., SUN A., KING W.E., HENSON N.J. ET AL. Modeling of additive manufacturing processes for metals: Challenges and opportunities. *Current Opinion in Solid State and Materials Science*, 21 (2017) (4): 198–206.

FRIED I. & RHEINBOLDT W. *Numerical Solution of Differential Equations*. Computer science and applied mathematics. Elsevier Science, Burlington, 2014.

FÜRSTENAU J.P., WEISSENFELS C. & WRIGGERS P. Free surface tension in incompressible smoothed particle hydrodynamics (ISPH). *In revision by Computational Mechanics*, (2019a).

FÜRSTENAU J.P., WESSELS H., WEISSENFELS C. & WRIGGERS P. Generating virtual process maps of SLM using powder scale SPH simulations. *In revision by Computational Particle Mechanics*, (2019b).

GANERIWALA R. & ZOHDI T.I. A coupled discrete element-finite difference model of selective laser sintering. *Granular Matter*, 18 (2016) (2).

GANZENMÜLLER G.C. An hourglass control algorithm for Lagrangian smooth-particle hydrodynamics. *Computer Methods in Applied Mechanics and Engineering*, 286 (2015): 87–106.

GANZENMÜLLER G.C., HIERMAIER S. & MAY M. On the similarity of meshless discretizations of peridynamics and smooth-particle hydrodynamics. *Computers & Structures*, 150 (2015): 71–78.

GEBHARDT A. & HÖTTER J.S. *Additive manufacturing: 3D printing for prototyping and manufacturing*. Hanser, Munich, Cincinnati, 2016.

GIBSON I., ROSEN D.W. & STUCKER B. *Additive Manufacturing Technologies: Rapid Prototyping to Direct Digital Manufacturing*. Springer, New York, Heidelberg, Dordrecht, London, 2010.

GIESEKE M., ALBRECHT D., NÖLKE C., KAIERLE S. ET AL. Laserbasierte Technologien. In LACHMAYER R., LIPPERT R.B. & FAHLBUSCH T., eds., *3D-Druck beleuchtet: Additive Manufacturing auf dem Weg in die Anwendung*. Springer Vieweg, Berlin, Heidelberg, 2016.

GINGOLD R.A. & MONAGHAN J.J. Smoothed particle hydrodynamics: Theory and application to non-spherical stars. *Monthly Notices of the Royal Astronomical Society*, 181 (1977) (3): 375–389.

GOLDAK J., CHAKRAVARTI A. & BIBBY M. A new finite element model for welding heat sources. *Metallurgical Transactions B*, 15 (1984) (2): 299–305.

GOLDAK J.A. & AKHLAGHI M. *Computational welding mechanics*. Springer, New York, 2005.

GRIEBEL M., KNAPEK S. & ZUMBUSCH G. *Numerical simulation in molecular dynamics: Numerics, algorithms, parallelization, applications*, volume 5 of *Texts in computational science and engineering*. Springer, Berlin, Heidelberg, 2007.

GRIEWANK A. *Evaluating derivatives: principles and techniques of algorithmic differentation*. SIAM, Philadelphia, Pennsylvania, 2008, 2nd edition.

GROSS H. *Fundamentals of technical optics*, volume 1 of *Handbook of optical systems*. Wiley-VCH, Weinheim, 2005.

GU D. & CHEN H. Selective laser melting of high strength and toughness stainless steel parts: The roles of laser hatch style and part placement strategy. *Materials Science and Engineering: A*, 725 (2018): 419–427.

GU D.D., MEINERS W., WISSENBACH K. & POPRAWE R. Laser additive manufacturing of metallic components: Materials, processes and mechanisms. *International Materials Reviews*, 57 (2013) (3): 133–164.

GUSAROV A.V., YADROITSEV I., BERTRAND P. & SMUROV I. Model of radiation and heat transfer in laser-powder interaction zone at selective laser melting. *Journal of Heat Transfer*, 131 (2009) (7): 072 101–1 – 072 101–10.

HAUPT P. *Viskoelastizität und Plastizität: Thermomechanisch konsistente Materialgleichungen*. Ingenieurwissenschaftliche Bibliothek. Springer, Berlin, Heidelberg, 1977.

HE X., FUERSCHBACH P.W. & DEBROY T. Heat transfer and fluid flow during laser spot welding of 304 stainless steel. *Journal of Physics D: Applied Physics*, 36 (2003) (12): 1388–1398.

HECHT J. *Understanding Lasers: An Entry-Level Guide*, volume 21 of *IEEE Press Understanding Science & Technology Series*. Wiley [etc.], Hoboken, New Jersey, 2011, 3rd edition.

HIRT C., AMSDEN A. & COOK J. An arbitrary Lagrangian-Eulerian computing method for all flow speeds. *Journal of Computational Physics*, 14 (1974) (3): 227–253.

HODGE N.E., FERENCZ R.M. & SOLBERG J.M. Implementation of a thermomechanical model for the simulation of selective laser melting. *Computational Mechanics*, 54 (2014) (1): 33–51.

HODGE N.E., FERENCZ R.M. & VIGNES R.M. Experimental comparison of residual stresses for a thermomechanical model for the simulation of selective laser melting. *Additive Manufacturing*, 12 (2016): 159–168.

HOLZAPFEL G.A. *Nonlinear solid mechanics: A continuum approach for engineering*. Wiley, Chichester, 2010, reprinted edition.

HU H. & ARGYROPOULOS S.A. Mathematical modelling of solidification and melting: A review. *Modelling and Simulation in Materials Science and Engineering*, 4 (1996) (4): 371–396.

HU H. & EBERHARD P. Thermomechanically coupled conduction mode laser welding simulations using smoothed particle hydrodynamics. *Computational Particle Mechanics*, 68 (2016) (2): 849.

HU H., FETZER F., BERGER P. & EBERHARD P. Simulation of laser welding using advanced particle methods. *GAMM-Mitteilungen*, 39 (2016) (2): 149–169.

HU Z., ZHU H., ZHANG C., ZHANG H. ET AL. Contact angle evolution during selective laser melting. *Materials & Design*, 139 (2018): 304–313.

HUDOBIVNIK B., ALDAKHEEL F. & WRIGGERS P. A low order 3D virtual element formulation for finite elasto–plastic deformations. *Computational Mechanics*, 51 (2018) (2): 794.

HUGHES T.J.R. *The finite element method: Linear static and dynamic finite element analysis*. Dover, Mineola, New York, 2000, reprinted edition.

KAMATH C. Data mining and statistical inference in selective laser melting. *The International Journal of Advanced Manufacturing Technology*, 86 (2016) (5-8): 1659–1677.

KAMATH C. & FAN Y.J. Regression with small data sets: A case study using code surrogates in additive manufacturing. *Knowledge and Information Systems*, 57 (2018) (2): 475–493.

KARDITSAS P.J. & BAPTISTE M.J. *Thermal and structural properties of fusion related materials*. http://aries.ucsd.edu/LIB/PROPS/PANOS, 2018.

KERGASSNER A., MERGHEIM J. & STEINMANN P. Modeling of additively manufactured materials using gradient-enhanced crystal plasticity. *Computers & Mathematics with Applications*, (2018).

KHAIRALLAH S.A. & ANDERSON A.T. Mesoscopic simulation model of selective laser melting of stainless steel powder. *Journal of Materials Processing Technology*, 214 (2014) (11): 2627–2636.

KHAIRALLAH S.A., ANDERSON A.T., RUBENCHIK A. & KING W.E. Laser powder-bed fusion additive manufacturing: Physics of complex melt flow and formation mechanisms of pores, spatter, and denudation zones. *Acta Materialia*, 108 (2016): 36–45.

KI H., MAZUMDER J. & MOHANTY P.S. Modeling of laser keyhole welding: Part I: Mathematical modeling, numerical methodology, role of recoil pressure, multiple reflections, and free surface evolution. *Metallurgical and Materials Transactions A*, 33 (2002) (6): 1817–1830.

KIKUCHI F. Discrete maximum principle and artificial viscosity in finite element approximations to convective diffusion equations. *Institute of Space and Aeronautical Science, Report No. 550*, (1977).

KING W.E., ANDERSON A.T., FERENCZ R.M., HODGE N.E. ET AL. Laser powder bed fusion additive manufacturing of metals; physics, computational, and materials challenges. *Applied Physics Reviews*, 2 (2015) (4): 041 304.

KORELC J. Automatic generation of finite-element code by simultaneous optimization of expressions. *Theoretical Computer Science*, 187 (1997) (1-2): 231–248.

KORELC J. Automation of primal and sensitivity analysis of transient coupled problems. *Computational Mechanics*, 44 (2009) (5): 631–649.

KORELC J. & STUPKIEWICZ S. Closed-form matrix exponential and its application in finite-strain plasticity. *International Journal for Numerical Methods in Engineering*, 98 (2014) (13): 960–987.

KORELC J. & WRIGGERS P. *Automation of finite element methods.* Springer, Cham, Switzerland, 2016.

KRAKHMALEV P., FREDRIKSSON G., SVENSSON K., YADROITSEV I. ET AL. Microstructure, solidification texture, and thermal stability of 316L stainless steel manufactured by laser powder bed fusion. *Metals*, 8 (2018) (8): 643.

KRUTH J.P., MERCELIS P., VAN VAERENBERGH J., FROYEN L. ET AL. Binding mechanisms in selective laser sintering and selective laser melting. *Rapid Prototyping Journal*, 11 (2005) (1): 26–36.

KUMAR S. & KRUTH J.P. Wear performance of SLS/SLM materials. *Advanced Engineering Materials*, 10 (2008) (8): 750–753.

LANDAU L.D. & LIFŠIC E.M. *Fluid dynamics*, volume 6 of *Course of theoretical physics*. Pergamon, Oxford, 1987, 2nd edition.

LEHMANN T. *The Constitutive law in thermoplasticity*, volume 281 of *Courses and lectures*. Springer-Verlag, Wien and New York, 1984.

LI B., HABBAL F. & ORTIZ M. Optimal transportation meshfree approximation schemes for fluid and plastic flows. *International Journal for Numerical Methods in Engineering*, 83 (2010) (12): 1541–1579.

LI B., STALZER M. & ORTIZ M. A massively parallel implementation of the optimal transportation meshfree method for explicit solid dynamics. *International Journal for Numerical Methods in Engineering*, 100 (2014) (1): 40–61.

LI S. & LIU W.K. *Meshfree particle methods*. Springer, Berlin, Heidelberg, New York, 2007, corrected edition.

LIAN Y., LIN S., YAN W., LIU W.K. ET AL. A parallelized three-dimensional cellular automaton model for grain growth during additive manufacturing. *Computational Mechanics*, 61 (2018) (5): 543–558.

LINDGREN L.E. *Computational welding mechanics: Thermomechanical and microstructructural simulations*. CRC Press, Boca Raton, Florida, 2007.

LINDGREN L.E. & LUNDBÄCK A. Approaches in computational welding mechanics applied to additive manufacturing: Review and outlook. *Comptes Rendus Mécanique*, 346 (2018) (11): 1033–1042.

LIU J., JALALAHMADI B., GUO Y.B., SEALY M.P. ET AL. A review of computational modeling in powder-based additive manufacturing for metallic part qualification. *Rapid Prototyping Journal*, 27 (2018) (1): 182.

LIU W.K., LI S. & BELYTSCHKO T. Moving least-square reproducing kernel methods (I) methodology and convergence. *Computer Methods in Applied Mechanics and Engineering*, 143 (1997) (1-2): 113–154.

LU S.C.H. & PISTER K.S. Decomposition of deformation and representation of the free energy function for isotropic thermoelastic solids. *International Journal of Solids and Structures*, 11 (1975) (7-8): 927–934.

LUCY L.B. A numerical approach to the testing of the fission hypothesis. *The Astronomical Journal*, 82 (1977): 1013.

MATHEMATICA 11.1. Wolfram Research, Inc. *http://www.wolfram.com*, (2017).

MERCELIS P. & KRUTH J.P. Residual stresses in selective laser sintering and selective laser melting. *Rapid Prototyping Journal*, 12 (2006) (5): 254–265.

MIEHE C. *Zur numerischen Behandlung thermomechanischer Prozesse*. Dissertation, Leibniz Universität Hannover (1988).

MORRIS J.P. Simulating surface tension with smoothed particle hydrodynamics. *International Journal for Numerical Methods in Fluids*, 33 (2000) (3): 333–353.

MUHIEDDINE M., CANOT É. & MARCH R. Various approaches for solving problems in heat conduction with phase change. *International Journal on Finite Volumes*, 6 (2009) (1): 66–85.

MUMTAZ K.A. & HOPKINSON N. Selective laser melting of thin wall parts using pulse shaping. *Journal of Materials Processing Technology*, 210 (2010) (2): 279–287.

NAVROTSKY V. 3D printing at Siemens power service. *www.siemens.fi/pool/cc/events/elp14/esitykset/navrotsky.pdf*, (2014).

NAYROLES B., TOUZOT G. & VILLON P. Generalizing the finite element method: Diffuse approximation and diffuse elements. *Computational Mechanics*, 10 (1992) (5): 307–318.

NEUGEBAUER F., KELLER N., FEUERHAHN F. & KOEHLER H. Multi scale FEM simulation for distortion calculation in additive manufacturing of hardening stainless steel. *International Conference on Thermal Forming and Welding Distortion*, (2014).

OÑATE E., IDELSOHN S.R., DEL PIN F. & AUBRY R. The particle finite element method: An overview. *International Journal of Computational Methods*, 01 (2004) (02): 267–307.

PANWISAWAS C., PERUMAL B., WARD R.M., TURNER N. ET AL. Keyhole formation and thermal fluid flow-induced porosity during laser fusion welding in titanium alloys: Experimental and modelling. *Acta Materialia*, 126 (2017a): 251–263.

PANWISAWAS C., QIU C., ANDERSON M.J., SOVANI Y. ET AL. Mesoscale modelling of selective laser melting: Thermal fluid dynamics and microstructural evolution. *Computational Materials Science*, 126 (2017b): 479–490.

PITSCHENEDER W., DEBROY T., MUNDRA K. & EBNER R. Role of sulfur and processing variables on the temporal evolution of weld pool geometry during multikilowatt laser beam welding of steels. *Welding Journal*, (1996): 71–80.

POIRIER D. & SALCUDEAN M. On numerical methods used in mathematical modeling of phase change in liquid metals. *Journal of Heat Transfer*, 110 (1988) (3): 562.

PRICE D.J. Smoothed particle hydrodynamics and magnetohydrodynamics. *Journal of Computational Physics*, 231 (2012) (3): 759–794.

QIU C., PANWISAWAS C., WARD M., BASOALTO H.C. ET AL. On the role of melt flow into the surface structure and porosity development during selective laser melting. *Acta Materialia*, 96 (2015): 72–79.

RAI A., MARKL M. & KÖRNER C. A coupled cellular automaton–lattice Boltzmann model for grain structure simulation during additive manufacturing. *Computational Materials Science*, 124 (2016): 37–48.

REESE S. & GOVINDJEE S. A theory of finite viscoelasticity and numerical aspects. *International Journal of Solids and Structures*, 35 (1998) (26-27): 3455–3482.

RIEDLBAUER D., SCHAROWSKY T., SINGER R.F., STEINMANN P. ET AL. Macroscopic simulation and experimental measurement of melt pool characteristics in selective electron beam melting of Ti-6Al-4V. *The International Journal of Advanced Manufacturing Technology*, 88 (2017) (5-8): 1309–1317.

RIEDLBAUER D., STEINMANN P. & MERGHEIM J. Thermomechanical finite element simulations of selective electron beam melting processes: Performance considerations. *Computational Mechanics*, 54 (2014) (1): 109–122.

ROMBOUTS M., FROYEN L., GUSAROV A.V., BENTEFOUR E.H. ET AL. Photopyroelectric measurement of thermal conductivity of metallic powders. *Journal of Applied Physics*, 97 (2005) (2): 024 905.

ROSENTHAL D. The theory of moving sources of heat and its application to metal treatments. *Transactions of the American Society of Mechanical Engineers*, 43 (1946): 849–866.

ROSOLEN A., MILLÁN D. & ARROYO M. On the optimum support size in meshfree methods: A variational adaptivity approach with maximum-entropy approximants. *International Journal for Numerical Methods in Engineering*, 139 (2009) (1): 868–895.

RUSSELL M.A., SOUTO-IGLESIAS A. & ZOHDI T.I. Numerical simulation of laser fusion additive manufacturing processes using the SPH method. *Computer Methods in Applied Mechanics and Engineering*, 341 (2018): 163–187.

SALDI Z.S., KIDESS A., KENJEREŠ S., ZHAO C. ET AL. Effect of enhanced heat and mass transport and flow reversal during cool down on weld pool shapes in laser spot welding of steel. *International Journal of Heat and Mass Transfer*, 66 (2013): 879–888.

SCHOINOCHORITIS B., CHANTZIS D. & SALONITIS K. Simulation of metallic powder bed additive manufacturing processes with the finite element method: A critical review. *Proceedings of the Institution of Mechanical Engineers, Part B: Journal of Engineering Manufacture*, 231 (2016) (1): 96–117.

SERCOMBE T., JONES N., DAY R. & KOP A. Heat treatment of Ti–6Al–7Nb components produced by selective laser melting. *Rapid Prototyping Journal*, 14 (2008) (5): 300–304.

SILLING S.A. Reformulation of elasticity theory for discontinuities and long-range forces. *Journal of the Mechanics and Physics of Solids*, 48 (2000) (1): 175–209.

SIMO J.C. & HUGHES T.J.R. *Computational inelasticity*, volume 7 of *Interdisciplinary applied mathematics*. Springer, New York, 1998.

SIMO J.C. & MIEHE C. Associative coupled thermoplasticity at finite strains: Formulation, numerical analysis and implementation. *Computer Methods in Applied Mechanics and Engineering*, 98 (1992) (1): 41–104.

SMITH J., XIONG W., CAO J. & LIU W.K. Thermodynamically consistent microstructure prediction of additively manufactured materials. *Computational Mechanics*, 57 (2016) (3): 359–370.

SONG B., DONG S., LIU Q., LIAO H. ET AL. Vacuum heat treatment of iron parts produced by selective laser melting: Microstructure, residual stress and tensile behavior. *Materials & Design (1980-2015)*, 54 (2014): 727–733.

STRANTZA M., GANERIWALA R.K., CLAUSEN B., PHAN T.Q. ET AL. Coupled experimental and computational study of residual stresses in additively manufactured Ti-6Al-4V components. *Materials Letters*, 231 (2018): 221–224.

THE INTERNATIONAL NICKEL COMPANY, ed. *Mechanical and physical properties of the austenitic chromium-nickel stainless steels at elevated temperatures*. New York, 1978, reprinted edition.

TONG M. & BROWNE D.J. An incompressible multi-phase smoothed particle hydrodynamics (SPH) method for modelling thermocapillary flow. *International Journal of Heat and Mass Transfer*, 73 (2014): 284–292.

TRUESDELL C. & NOLL W. *The non-linear field theories of mechanics*. Springer, Berlin, 2004, 3rd edition.

VERHAEGHE F., CRAEGHS T., HEULENS J. & PANDELAERS L. A pragmatic model for selective laser melting with evaporation. *Acta Materialia*, 57 (2009) (20): 6006–6012.

VILLANI C. *Topics in optimal transportation*, volume 58 of *Graduate studies in mathematics*. American Mathematical Society, Providence, Rhode Island, 2003.

WEISSENFELS C. & WRIGGERS P. Stabilization algorithm for the optimal transportation meshfree approximation scheme. *Computer Methods in Applied Mechanics and Engineering*, 329 (2018): 421–443.

WESSELS H., BODE T., WEISSENFELS C., WRIGGERS P. ET AL. Investigation of heat source modeling for selective laser melting. *Computational Mechanics*, 63 (2019) (5): 949–970.

WESSELS H., WEISSENFELS C. & WRIGGERS P. Metal particle fusion analysis for additive manufacturing using the stabilized optimal transportation meshfree method. *Computer Methods in Applied Mechanics and Engineering*, 339 (2018): 91–114.

WITHERS P.J. & BHADESHIA H. Residual stress. Part 1 – measurement techniques. *Materials Science and Technology*, 17 (2001a) (4): 355–365.

WITHERS P.J. & BHADESHIA H. Residual stress. Part 2 – nature and origins. *Materials Science and Technology*, 17 (2001b) (4): 366–375.

WOHLERS T.T. *Wohlers Report: 3D printing and additive manufacturing state of the industry*. Wohlers Associates, Fort Collins, 2017.

WRIGGERS P. *Computational Contact Mechanics*. Springer, Berlin, Heidelberg, 2006.

WRIGGERS P. *Nonlinear finite element methods*. Springer, Berlin, Heidelberg, 2008.

WRIGGERS P., MIEHE C., KLEIBER M. & SIMO J.C. On the coupled thermomechanical treatment of necking problems via finite element methods. *International Journal for Numerical Methods in Engineering*, 33 (1992) (4): 869–883.

YADROITSEV I. *Selective laser melting: Direct manufacturing of 3D objects by selective laser melting of metal powders*. Dissertation, ENISE, Saint-Etienne (2008).

YAN W., GE W., QIAN Y., LIN S. ET AL. Multi-physics modeling of single/multiple-track defect mechanisms in electron beam selective melting. *Acta Materialia*, (2017).

YAN W., LIN S., KAFKA O.L., LIAN Y. ET AL. Data-driven multi-scale multi-physics models to derive process–structure–property relationships for additive manufacturing. *Computational Mechanics*, 61 (2018a) (5): 521–541.

YAN W., LIN S., KAFKA O.L., YU C. ET AL. Modeling process-structure-property relationships for additive manufacturing. *Frontiers of Mechanical Engineering*, 13 (2018b) (4): 482–492.

YAN W., QIAN Y., GE W., LIN S. ET AL. Meso-scale modeling of multiple-layer fabrication process in selective electron beam melting: Inter-layer/track voids formation. *Materials & Design*, 141 (2018c): 210–219.

YAN W., SMITH J., GE W., LIN F. ET AL. Multiscale modeling of electron beam and substrate interaction: A new heat source model. *Computational Mechanics*, 56 (2015) (2): 265–276.

ZIENKIEWICZ O.C., ZHU J.Z. & TAYLOR R.L. *The finite element method: Its basis and fundamentals*. Butterworth-Heinemann, Oxford, UK, 2013, 7th edition.

ZOHDI T.I. Computation of the coupled thermo-optical scattering properties of random particulate systems. *Computer Methods in Applied Mechanics and Engineering*, 195 (2006a) (41-43): 5813–5830.

ZOHDI T.I. On the optical thickness of disordered particulate media. *Mechanics of Materials*, 38 (2006b) (8-10): 969–981.

ZOHDI T.I. Simulation of coupled microscale multiphysical-fields in particulate-doped dielectrics with staggered adaptive fdtd. *Computer Methods in Applied Mechanics and Engineering*, 199 (2010) (49-52): 3250–3269.

ZOHDI T.I. Rapid simulation of laser processing of discrete particulate materials. *Archives of Computational Methods in Engineering*, 20 (2013) (4): 309–325.

ZOHDI T.I. Additive particle deposition and selective laser processing - a computational manufacturing framework. *Computational Mechanics*, 54 (2014) (1): 171–191.

ZOHDI T.I. Modeling of the scattering response of particulate obscurant clouds. *International Journal of Engineering Science*, 89 (2015a): 75–85.

ZOHDI T.I. On the thermal response of a surface deposited laser-irradiated powder particle. *CIRP Journal of Manufacturing Science and Technology*, 10 (2015b): 77–83.

ZOHDI T.I. Construction of a rapid simulation design tool for thermal responses to laser-induced feature patterns. *Computational Mechanics*, 295 (2017a) (7): 315.

ZOHDI T.I. On high-frequency radiation scattering sensitivity to surface roughness in particulate media. *Computational Particle Mechanics*, 4 (2017b) (1): 13–22.

ZOHDI T.I. *Modeling and Simulation of Functionalized Materials for Additive Manufacturing and 3D Printing: Continuous and Discrete Media: Continuum and Discrete Element Methods*, volume 60 of *Lecture notes in applied and computational mechanics*. Springer, Cham, Switzerland, 2018.

ZOHDI T.I. Ultra-fast laser-patterning computation for advanced manufacturing of powdered materials exploiting knowledge-based heat-kernels. *Computer Methods in Applied Mechanics and Engineering*, 343 (2019): 234–248.

ZOHDI T.I. & KUYPERS F.A. Modelling and rapid simulation of multiple red blood cell light scattering. *Journal of the Royal Society, Interface*, 3 (2006) (11): 823–831.

Curriculum vitae

Henning Wessels
born May 13, 1990 in Hildesheim, Germany

Professional Experience

since 04.2016	Research assistant at the Institute of Continuum Mechanics, Leibniz Universität Hannover
04.2017 - 09.2017	Visiting researcher at the Computational Manufacturing and Materials Research Lab, University of California, Berkeley

Education

10.2013 - 02.2016	Leibniz Universität Hannover Mechanical Engineering Degree: Master of Science (with distinction)
09.2014 - 02.2015	Aristotle University Thessaloniki Mechanical Engineering
10.2010 - 11.2013	Leibniz Universität Hannover Mechanical Engineering Degree: Bachelor of Science
08.1996 - 07.2000	Primary school at Grundschule Itzum, Hildesheim
08.2000 - 06.2002	Middle school at Orientierungsstufe Don Bosco, Hildesheim
08.2002 - 05.2009	Secondary school at Scharnhorstgymnasium Hildesheim
09.2006 - 01.2007	Secondary school at Lycée Thiers, Marseille

Civil Service

10.2009 - 04.2010	Nurse assistant at Herz-Jesu-Krankenhaus, Münster
08.2009 - 10.2009	Facility Management at DKV-Residenz am Tibusplatz, Münster

Scholarships

04.2017 - 09.2017	Fulbright Doctoral Program
11.2015	Scholarship ”Niedersachsenstipendium”
09.2014 - 02.2015	Erasmus+ Study Mobility Program
10.2014 - 09.2015	Scholarship ”Deutschlandstipendium”
02.2006 - 01.2007	Voltaire Program of the Franco-German Youth Office